ELASTIC EFFECTS IN FLEXIBLE DIMERIC AND ELASTOMER NEMATICS

A dissertation submitted

to Kent State University in partial

fulfillment of the requirements for the

degree of Doctor of Philosophy

by

Greta Babakhanova

May, 2019

Dissertation written by

Greta Babakhanova

B.S., San Jose State University, USA 2014

M.S., Kent State University, USA, 2016

Ph.D. Kent State Univerisity, USA, 2019

Approved by

Dr. Oleg D. Lavrentovich, Chair, Doctoral Dissertation Committee

Dr. Antal Jákli, Members, Doctoral Dissertation Committee

Dr. Samuel Sprunt

Dr. Min-Ho Kim

Dr. Elizabeth Mann

Accepted by

Dr. Antal Jákli, Chair, Department of Chemical Physics

Dr. James L. Blank, Dean, College of Arts and Sciences

TABLE OF CONTENTS

TABLE OF CONTENTS III

LIST OF FIGURES VII

LIST OF TABLES XVII

DEDICATION XVIII

ACKNOWLEDGEMENTS XIX

CHAPTER 1 INTRODUCTION 1

1.1 Flexible dimeric liquid crystals 1

1.2 Smart and biocompatible polymerized liquid crystal coatings 4

1.3 Scope and objectives of the dissertation 7

CHAPTER 2 FLEXIBLE DIMERS WITH POSITIVE DIELECTRIC ANISOTROPY 12

2.1 Introduction 12

2.2 Materials and Methods 16

2.2.1 Chemical structure, phase diagram, and alignment 16

2.2.2 Refractive indices and birefringence 18

2.2.3 Electro-optical measurements 20

2.2.4 Diamagnetic anisotropy 20

2.2.5 Dynamic light scattering 22

2.3 Results 28

2.3.1 Refractive indices and birefringence 28

2.3.2 Dielectric and diamagnetic properties 28
2.3.3 Elastic constants 30
2.4 Discussion 34
2.5 Conclusion 43
CHAPTER 3 COMPARATIVE ANALYSIS OF ANISOTROPIC MATERIAL PROPERTIES OF UNIAXIAL NEMATICS FORMED BY FLEXIBLE DIMERS AND ROD-LIKE MESOGENS WITH NEGATIVE DIELECTRIC ANISOTROPY 45
3.1 Introduction 45
3.2 Materials and methods 47
3.2.1 Chemical structure, phase diagram and alignment 47
3.2.2 Dielectric anisotropy 50
3.2.3 Birefringence 51
3.2.4 Elastic constants 51
3.3 Results 55
3.3.1 Dielectric anisotropy 55
3.3.2 Birefringence 56
3.3.3 Elastic constants 59
3.4 Discussion 62
3.5 Conclusion 67

CHAPTER 4 LIQUID CRYSTAL ELASTOMER COATINGS WITH PROGRAMMED RESPONSE OF SURFACE PROFILE 69

4.1 Introduction 69

4.2 Materials and methods 70

4.2.1 Photoalignment of substrates 70

4.2.2 Preparation of the liquid crystalline polymeric coatings 72

4.2.3 Surface topography measurements 73

4.3 Results 73

4.3.1 Pre-programming the LCE coatings 73

4.3.2 Surface depressions caused by radial defects 75

4.3.3 Surface elevations caused by circular defects 76

4.3.4 Coupled elevations-depressions caused by ±1/2 defects 77

4.3.5 Depressions/elevations caused by splay/bend stripe patterns 80

4.4 Discussion 81

4.5 Conclusion 89

CHAPTER 5 GUIDING MICROPARTICLES VIA LIGHT-ACTIVATED DEFORMATIONS OF LIQUID CRYSTAL ELASTOMERS 90

5.1 Introduction 90

5.2 Materials and methods 91

5.2.1 Preparation of the liquid crystal cells 91

5.2.2 Preparation of the light responsive LCE coatings 93

5.3 Results and discussion 93

5.4 Conclusion 101

CHAPTER 6 DIRECTING MOTILE SKIN CELLS VIA POLYMERIZED LIQUID CRYSTAL NANOSTRUCTURES 103

6.1 Introduction 103

6.2 Materials and Methods 104

6.2.1 Preparation of the nanogrooved surfaces 104

6.2.2 Surface characterization 106

6.2.3 Culturing Human Dermal Fibroblasts 106

6.2.4 Immunocytochemistry 107

6.3 Results 107

6.4 Discussion 111

6.5 Conclusion 113

CHAPTER 7 SUMMARY 115

REFERENCES 117

LIST OF FIGURES

Figure 1-1 a) Schematic representation of molecular organization of the N_{TB} phase, b) FFTEM image of plunge-frozen CB7CB dimer at $T = 95$ °C in the N_{TB} phase; the bulk replica shows the nanoscale modulation in N_{TB} phase. 1

Figure 1-2. Schematic representation of the polymer network conformation upon heating/cooling the material. 6

Figure 1-3. Schematic representation of *trans-cis* conformational change of azobenzene molecule..... 7

Figure 2-1. Molecular structure of CB7CB with electrostatic potential surface and phase diagram upon cooling (negative and positive electric charges excesses are shown as red and blue, respectively). 17

Figure 2-2. POM textures of CB7CB under cross polarizers showing uniformly aligned (a) N and (b) N_{TB} phases with focal conic domains. The direction of rubbing is shown by the axis $\hat{r}$ 17

Figure 2-3. Senarmont experimental set-up for birefringence measurements. 19

Figure 2-4. Optical set-up to determine $\Delta\chi$ 21

Figure 2-5. Light scattering geometries. "1": splay+twist scattering; "2": pure bend scattering ($\theta_l = \theta_m$) and predominantly twist scattering ($\theta_l = 2°$). $\vec{K}_i$ and $\vec{K}_s$ correspond to incident and scattering wave vectors respectively; θ_l is scattering angle measured in the laboratory frame; θ_m refers to the so-called "magic angle";

Π_i and Π_s indicate the light of incident polarization and scattering polarizations which are orthogonal to each other..... 23

Figure 2-6. (a) Refractive indices of CB7CB ($\lambda = 633$ nm); filled symbols represent the data acquired using a planar wedge cell; dotted and solid lines represent the fitted values of n_o and n_e respectively; (b) Δn measured at $\lambda = 633$ nm using Senarmont technique (circles), planar wedge cell (squares)..... 28

Figure 2-7. (a) Parallel and perpendicular components of temperature dependent dielectric constants and (b) $\Delta\varepsilon$ measured at $f = 5, 10, 20, 40$ and 60 kHz using a planar cell ($d = 18.9$ μm) of CB7CB..... 29

Figure 2-8. (a) Temperature dependence of $\Delta\chi$ fitted with Haller's rule and (b) orientational order parameter of CB7CB..... 30

Figure 2-9. (a) K_{11}, K_{22} and K_{33} data of CB7CB obtained using DLS and K_{11} data obtained using capacitance method at $f = 60$ kHz ; (b) temperature behavior of K_{33} (DLS method)..... 32

Figure 2-10. Ratios of elastic constants of CB7CB (a) K_{11} / K_{33} and K_{11} / K_{22}, (b) K_{33} / K_{22} from DLS data..... 33

Figure 2-11. Temperature dependence of orientational viscosities of CB7CB. 34

Figure 2-12. Temperature dependence of orientational diffusivities of CB7CB..... 34

Figure 3-1. Schematic representation of the bend Frederiks transition. In the field off state (left panel), the LC ($\Delta\varepsilon < 0$) is oriented homeotropically. After the threshold voltage

(right panel), the director experiences reorientation. Since the dielectric anisotropy is negative, the molecules in the bulk align perpendicular to the applied electric field.46

Figure 3-2. Chemical structures and phase diagrams of the liquid crystal monomer MCT5 (a) and dimer DTC5C9 (b) with negative dielectric anisotropy. The phase diagram was determined on cooling at the rate of 0.1°C/min from the isotropic phase..... 48

Figure 3-3. Polarizing optical microscope textures of DTC5C9 in the (a,b) homeotropic N cell ($d = 19.4\,\mu\text{m}$) and (c) planar N cell ($d = 21.5\,\mu\text{m}$); (d) planar N_{TB} cell with stripes and focal conic domains ($d = 21.5\,\mu\text{m}$). Part (b) shows the conoscopic pattern characteristic of a homeotropic uniaxial nematic. The director in part (c) is along the rubbing direction R; polarizer and analyzer are labelled as P and A..... 49

Figure 3-4. Polarizing optical microscope textures of MCT5 in the (a,b) homeotropic N cell (cell thickness $d = 19.5\,\mu\text{m}$); (c,d) planar N cell ($d = 19.5\,\mu\text{m}$). Part (b) shows the conoscopic pattern characteristic of a homeotropic uniaxial nematic. The director in part (c) and (d) is along the rubbing direction R. 50

Figure 3-5. Determination of V_{th3} for DTC5C9 material in a homeotropic cell with $d = 19.4\mu\text{m}$ at $T - T_{NI} = -24^{o}\text{C}$. The bold straight lines illustrate how the threshold is determined by double extrapolation..... 54

Figure 3-6. Temperature dependence of the dielectric anisotropy for liquid crystal monomer MCT5 (open symbols) and dimer DTC5C9 (filled symbols) measured at frequencies of 40 and 10 kHz respectively. The dashed vertical line represents N-N_{TB} transition temperature for DTC5C9. 56

Figure 3-7. Temperature dependence of Δn for (a) monomer MCT5 (open symbols) and (b) dimer DTC5C9 (filled symbols). The wavelength of the probing light was 546 nm. 58

Figure 3-8. Temperature dependence of S for the monomer MCT5 (open symbols) and dimer DTC5C9 (filled symbols). Dotted lines connecting the data points are guides for eyes. 59

Figure 3-9. Temperature dependent elastic constants of MCT5 (open symbols) and dimer DTC5C9 (filled symbols). 60

Figure 3-10. Temperature dependencies of the ratios (a) K_{11} / K_{22} (b) K_{22} / K_{33} and (c) K_{11} / K_{33} for MCT5 (open symbols) and DTC5C9 (filled symbols). 61

Figure 3-11. Temperature dependence of K_{33} for DTC5C9. Filled and empty circles represent the results obtained by the light intensity measurements with applied electric fields at 10 and 40 kHz respectively. The stars represent K_{33} extrapolated from the capacitance vs voltage curve. 62

Figure 4-1. Plasmonic metamasks. Scanning electron microscopy images of fragments of metamasks with (a) radial defect, $m = +1$ and $\varphi_0 = 0$. Scale bar, 1 μm. b, circular defect, $m = +1$ and $\varphi_0 = \pi / 2$. Scale bar, 1 μm. c, $m = +1/2$ defect. Scale bar, 1 μm. 71

Figure 4-2. Optical set-up for photopatterning. Experimental set-up for photopatterning the director field onto the empty cell consisting of two glass substrates coated with photosensitive layer. 72

Figure 4-3. Materials. The chemical composition of liquid crystal monomers and photoinitiator used to create the responsive LCEs. a, RM82 (25 wt%). b, RM23 (25 wt%). c, RM105 (49.2 wt%). d, Irgacure 819 (0.8 wt%). 73

Figure 4-4. Surface depressions developed by radial defects upon heating. a, PolScope image of a flat LCE coating at 23 ˚C which maps the optical retardance and the director orientation. Scale bar, 50 μm. b, 3D image of surface topography of LCE coating at 100 ˚C with developed depressions at radial defects, as observed using DHM. c, DHM image of the LCE surface at 100 ˚C used to extract the surface topography. Scale bar, 100 μm. d, Surface profiles along line *MM'* in (c) at 23 ˚C, 60 ˚C, 100 ˚C. e, Activation force density $\mathbf{f}$ map calculated for region outlined by a red box in (a,c). 75

Figure 4-5. Surface elevations developed at circular defects upon heating. a, PolScope image of a flat LCE coating at 30 ˚C which maps the optical retardance and the director orientation. Scale bar, 100 μm. b, 3D image of surface topography of LCE at 100 ˚C with elevations developed at circular defects, as observed using DHM. c, DHM image of the LCE surface at 100 ˚C used to extract the surface topography. Scale bar, 100 μm. d, Surface profiles along line *LL'* in (c) at 100 ˚C. e, Activation force density $\mathbf{f}$ map calculated for region outlined by a red box in (a,c). 76

Figure 4-6. Coupled elevations-depressions caused by ±1/2 defects upon heating. a, PolScope image of a flat LCE coating at 23 ˚C which maps the optical retardance and the director orientation; red boxes A and B show two different director configurations of the defect pairs. Scale bar, 50 μm. b, DHM image of the non-flat LCE surface at 100 ˚C used to extract the surface profile along line *TT'*. Scale bar, 50 μm. c, Surface profiles along line *TT'* in (b) at 23 ˚C, 60 ˚C and 100 ˚C. d, 3D image of surface topography of LCE at 100 ˚C observed using DHM. e, Grayscale PolScope images taken at 30 ˚C and 130 ˚C showing the displacement of the half-integer defects as a function of temperature and director configuration that separates the defects. f, Plot showing the distance separating ±1/2 defects as a function of temperature and director configurations A and B. The error bars represent the s.d.'s of 12 measurements. g, Director configuration for pair A. h, Activation force density $\mathbf{f}$ map calculated for the director pattern A. i, Director configuration for pair B. j, Activation force density $\mathbf{f}$ map calculated for director pattern B. 79

Figure 4-7. Depressions/elevations caused by splay/bend stripes upon heating. a, DHM image at 100 ˚C used to extract the surface profile along line *NN'*. Scale bar, 50 μm. b, PolScope image of a flat LCE coating at 23˚C which maps the optical retardance and the director orientation. Scale bar, 25 μm. c, Activation force density map calculated for region in (a,b) outlined by a red box. d, Surface profiles along line *NN'* in (a) at 24 ˚C, 60 ˚C and 100 ˚C. e, 3D image of surface topography of LCE at 100˚C observed using DHM. 81

Figure 4-8. Polymer network conformation and occurrence of the activation force. a, Prolate ellipsoid of polymer network conformations in the nematic phase; the long axis is along the director $\hat{\mathbf{n}}$; during heating, the ellipsoid shrinks along the long axis; in the isotropic phase, it becomes a sphere, as shown in part (b); the shrinking ellipsoid is modelled by a pair of forces $\mathbf{F}$. c, Activation force density $\mathbf{f}$ produced by contracting ellipsoids in the geometry of splay. d, Activation force density $\mathbf{f}$ produced by contracting ellipsoids in the geometry of bend. e, Map of activation forces in the pattern of a radial splay that push the material away from the center towards the periphery upon heating. f, Map of activation forces in the pattern of a circular bend that push the material from the periphery towards the center. 83

Figure 5-1 Chemical structures of liquid crystal monomers (a) RM82, (b) RM23, (c) RM105, (d) azo-dye, A3MA and (e) photoinitiator Irgacure 819. 92

Figure 5-2. Schematic representation of assembled cells consisting of a) an identical linear V-stripes at the top and bottom glass boundaries, b) linear photopatterned “V-stripes” and unidirectional planar substrates, c) circular “C-stripes” and unidirectional planar glass substrates. Scale bar $40\ \mu\mathrm{m}$ 92

Figure 5-3. LS system. a) 3D visualization of an actuated LCE with LS pattern showing alternating linear hills and valleys, b) light microscopy image showing the random distribution of microparticles at the initial deposition on an LCE surface, c) histogram showing the $80\ \mu\mathrm{m}$ periodicity of microparticle separation after UV light

illumination, d) light microscopy image showing linear chains of assembled microparticles at the disclination sites. Scale bar $100\ \mu\text{m}$ 96

Figure 5-4. CS system. a) 3D visualization of an actuated LCE showing circular surface topography, b) light microscopy image showing the microparticles assembling at the disclination sites after UV irradiation, c) histograms showing periodic $80\ \mu\text{m}$ microparticle separation upon UV light irradiation. The number of particles increases with distance, *R*, since the radius and length of each trough increase with the distance. Scale bar $50\ \mu\text{m}$ 97

Figure 5-5. NS system. a) 3D visualization of an actuated LCE showing linear, periodic hills and valleys, b) linear V-striped prepatterned LCE showing microparticles forming chain-like assemblies in the splay regions of the LCE coating where valleys are formed upon UV irradiation, c) histogram showing spatial distribution of the microparticles upon UV light irradiation exhibiting the $80\ \mu\text{m}$ periodicity. Scale bar $100\ \mu\text{m}$ 98

Figure 5-6. CS system. a) Initial deposition of microparticles dispersed in water onto a flat LCE surface showing random distribution, b) microparticles aggregated at the disclination sites where the valleys were formed upon UV illumination for 3 min, c) blue light illumination for 3 min yielded random distribution of microparticles, thus, showing the reversibility of the system. Scale bar $50\ \mu\text{m}$ 99

Figure 6-1. Chemical structures of (a) RM82, (b) Irgacure 651 and (c) 8OCB, (d) Schematic representation of the oily streak structure at the air/SmA LC interface. 105

Figure 6-2. a) Bright field observations of the polymerized oily streak structures oriented at 45 °; scalebar 20 μm. b) AFM image showing the grooved periodic surface profiles. 106

Figure 6-3. Human dermal fibroblast cells grown on flat glass substrate a) with fibronectin, b) without fibronectin and nanogrooved LC polymer surfaces c) with fibronectin, d) without fibronectin. Actin filaments are presented in green, while the nuclei correspond to the red oval regions. The arrows represent the direction of the nanogrooves. Scalebar 50 μm. 109

Figure 6-4. Orientational scalar order parameter (*S*) of human dermal fibroblast cells grown on flat glass with and without fibronectin as well as on nanogrooved surfaces with and without the fibronectin treatment. 109

Figure 6-5. Day 3 of human dermal fibroblast cells grown on a) fibronectin coated and b) fibronectin-free nanogrooved surfaces. The arrows represent the direction of the nanogrooves. Actin filaments are presented in red and the nuclei correspond to the light blue oval regions. 110

Figure 6-6. Distribution of actin filament orientations for flat and nanogrooved surfaces without fibronectin treatment. The arrow represents the direction of the nanogrooves. Scalebar 50 μm. 110

Figure 6-7. A collage of single human dermal fibroblast after day 1 of cells grown on a) fibronectin coated and b) fibronectin-free nanogrooved surfaces. Actin filaments are

presented in red and the nuclei correspond to the light blue oval regions. The average aspect ratios of the cells are a) 3.3 and b) 7.6. Scale bar 100 μm..... 111

LIST OF TABLES

Table 2-1. Elastic constants and their ratios of CB7CB dimer, 8OCB calamitic mesogen (I-N-SmA transitions), bent-core mesogens 12-F (I-N-SmA) and A131 (I-N-SmC) at $T_{norm} \approx 0.1$ and 0.2. The normalized temperature equals 1 at the I-N transition point and 0 at the transition point from N to the lower-temperature phase. 39

DEDICATION

"Straight ahead of him, nobody can go very far..."

Antoine de Saint-Exupéry

I dedicate my work to all who gave me a chance throughout my zigzag journey.

ACKNOWLEDGEMENTS

I am very grateful for my parents and grandparents, who instilled the value of education, discipline, persistence and self-reliability. Thanks to my lovely sisters: Annushka, Marisha and Sirushik who continuously help and encourage me. I am also deeply thankful for the companionship with Jagat Budhathoki, one of the most curious and competitive scientists I know. His humor, seriousness and genuine support helped me to make it through some of the gloomiest moments of graduate school.

I am thankful to my beloved teachers, mentors and professors for their understanding, mentorship and for their inspiration and support to pursue higher education: Levon Sergeyevich, Lilit Vazgenovna, Hasmik Zavenovna, Tara Sikorski, Marco Giordano, Bertha Aguayo, Olga Stepanovna, Dr. Karen Singmaster, Dr. Maureen Scharberg, Dr. Peter Beyersdorf, Dr. Larissa Chiriaeva, Dr. Romey Sabalius, Dr. Monika Kress, Dr. Carel Boekema, Dr. David Newton, Dr. Cynthia Phillips, Dr. Amy Mainzer, Dr. Nugent, Dr. Robin Selinger, Dr. Mina Katramatou, Dr. Torsten Hegmann, Dr. Oleg Lavrentovich and Dr. Jonathan Selinger.

Importantly, I am so lucky to have had the guidance and support of my advisor, Dr. Oleg D. Lavrentovich. He was instrumental throughout my Ph.D. journey. I will be forever thankful for his goal-oriented, fruitful & serious meetings, availability of resources and numerous travel opportunities that enriched my graduate school experience. I am grateful that Prof. Lavrentovich granted me independence and ability to pursue variety of projects, where I learned new skillsets and formed new collaborations. With each collaboration, I made life-long connections that are invaluable for me.

Working in his dynamic and multidisciplinary lab, I found new directions of scientific interests.

I want to thank Dr. Jákli, Dr. Frey, Dr. West and Dr. Lavrentovich for the opportunity to work together with Dr. Stannarius, Dr. Eremin, Dr. Sebastian and Dr. Nadasi at Otto-von-Guericke-Universität Magdeburg and experience German culture. I am thankful for Dr. Sprunt for giving me the means to learn about the remarkable light-scattering technique in his lab. The countless struggles in the dark light-scattering room gave me a chance to develop solid friendship with Zeinab Parsouzi. Another collaboration with Dr. Schenning, Dr. Liu, Dr. Hendrikx and Dr. Broer at Eindhoven University of Technology opened a big window of opportunity for me to learn about functional materials. That trip immediately changed my career path and I am very grateful that I had the opportunity to interact with Dr. Schenning, Dr. Broer and Dr. Lavrentovich directly over a cup of delicious hot chocolate! I am proud to say that my goal to conduct interdisciplinary research to solve biomedical questions came true at the end of my graduate school career through collaboration with Jess Krieger, Dr. Bing Yu and Dr. Kim. I enjoyed every single aspect of combining material science, imaging and biology. I am forever thankful to Dr. Min Gao and Dr. Lu Zou for introducing me to one of the most sophisticated imaging techniques which I fell in love with: atomic force microscopy, scanning and (freeze fracture/cryo) transmission electron microscopy.

It is a great pleasure to also acknowledge my colleagues and collaborators who have trained me, collaborated with me and gave valuable advice:

Dr. Y. Nastishin, Dr. Y-Ki Kim, Dr. Q-H. Wei, Dr. N. Sebastian, Dr. A. Eremin, Dr. S. Shiyanovkii, I. Chaganava, B. Li, Dr. S. Paladugu, Dr. F. Liu, Dr. Zhou, T. Turiv, H. Wang, Dr. V. Joshi, Dr. G. Mehl, H. Yu, Y. Golestani, Dr. S. Afghah, M. Rajabi, Dr. Y. Guo, M. Mrukiewicz, H. Baza, D. Li, R. Koizumi, O. Iadlovska, B. Wall, Dr. P. Shiller, D. Bryant, Dr. V. Borshch, Dr. J. Xiang, Dr. B. Tury, Dr. C. Peng, M. A. Kopcak, Dr. Shay Little and M. L. Bergstrom.

Thank you all for the great cooperation and enjoyable working atmosphere!

Best regards,

Greta Babakhanova

May 2019, Kent, Ohio

CHAPTER 1

Introduction

1.1 Flexible dimeric liquid crystals

Recently, a nanostructured twist-bend nematic (N_{TB}) formed by achiral flexible dimers connected by a flexible chain was determined as a new type of a liquid crystal (LC) phase on the basis of electron microscopy experiments (*1, 2*). The N_{TB} phase is characterized by a molecular orientation that follows an oblique helicoid exhibiting a pitch on the order of 10 nm (Figure 1-1) (*1-9*). The characteristic striped texture of the freeze fracture transmission electron microscopy (FFTEM) image demonstrates the nanoscale pitch of the N_{TB} phase of one of the well-studied dimers named 1,7-bis-4-(4′-cyanobiphenyl) heptane (CB7CB) , Figure 1-1b.

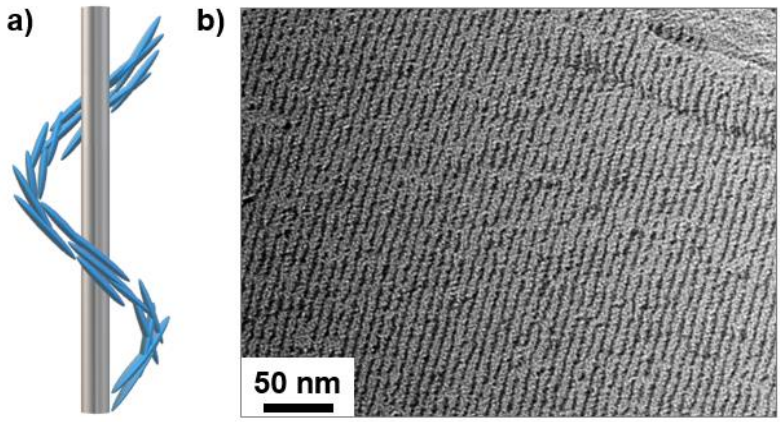

Figure 1-1 a) Schematic representation of molecular organization of the N_{TB} phase, b) FFTEM image of plunge-frozen CB7CB dimer at $T = 95$ °C in the N_{TB} phase; the bulk replica shows the nanoscale modulation in N_{TB} phase.

The N_{TB} phase occurs when the mesogenic molecules favor bend conformations; in the theory of Dozov, these spontaneous deformations can be assigned a negative value of the effective bend elastic constant K_{33} (*10*). Bend deformations, however, cannot fill the 3D space uniformly (*11*). For the nematic phase with bend deformations to be stable, bend must be accompanied either by splay or by twist (*11*). Thus two different variations of the nematic with spontaneous bend have been proposed by Meyer (*12*) and Dozov (*10*): a twist-bend nematic and a splay-bend nematic. The relative stability of the two is controlled by the ratio of the splay K_{11} to twist K_{22} constants. The bend-twist combination produces a stable N_{TB} phase provided the splay elastic constant K_{11} is noticeably larger than the twist elastic constant K_{22}, satisfying the condition $K_{11} / K_{22} > 2$, while in the splay-bend case, $K_{11} / K_{22} < 2$ (*10, 12, 13*).

The important connection between the type of molecular packings and elasticity has attracted a strong research interest to the measurements of elastic constants of flexible dimers in the uniaxial nematic (N) phase that exists at temperatures above the N_{TB} range (*14-20*). It was found that in many N_{TB}-forming dimeric materials, K_{33} in the N phase is indeed anomalously low, about 0.5 pN near the N-N_{TB} transition temperature T_{N-TB} (*14, 15, 17, 19-22*). Note here, that in the case of conventional rod-like LCs, the magnitudes of the elastic constants typically follow $K_{33} > K_{11} > K_{22}$ trend, where the bend elastic modulus has the highest value (*23*). An important feature of N_{TB}-forming LC dimers, which generally satisfy $K_{33} < K_{22}$ condition, is the ability to stabilize oblique helicoidal state of the director field by doping the LC mixture with a small amount of chiral dopant

and by applying an electric or magnetic field (*24-26*). We denote this state as CH_{OH}, where the subscript OH stands for 'oblique helicoid'. The CH_{OH} state was predicted by de Gennes (*27*) and Meyer (*11*) and experimentally demonstrated by Xiang and coworkers, who exploited this feature to achieve selective light reflection by tuning the pitch via an electric or magnetic field (*24-26*). In light of the importance of this material for understanding of N_{TB} and Ch_{OH} structures, it is critical to perform careful measurement of material parameters, as several prior experimental reports on the elastic constants of the nematic phase of CB7CB dimer are rather controversial.

The goal of our investigation of flexible dimers that form the N_{TB} phase is to understand the effect of the molecular shape on the macroscopic material properties in the high temperature N phase. At the beginning stages of this dissertation, only three publications reported measurements of all three bulk elastic constants of the nematic phase of dimers (*15, 16, 18*). Adlem et al (*15*) measured these for a mixture of dimers; although the data are valuable, presence of many (five) components makes it rather difficult to establish structure-property relationship. Yun et al (*16*) measured all three elastic constants for a single compound, CB7CB, but the measurements were at odds with the theoretical model (*10*) and the fact that CB7CB shows an N_{TB} phase as opposed to splay-bend phase. Namely, in Ref.(*16*), the ratio $K_{11} / K_{22} < 2$, while the stability of the N_{TB} phase requires $K_{11} / K_{22} > 2$. Finally, Sebastian et al (*18*) reported measurements for a dimeric material of negative dielectric anisotropy, in which the most important parameter, the bend elastic constant K_{33}, was obtained by an extrapolation technique

rather than through a direct measurement. Thus, there was a need to present accurate and direct measurements of the material parameters of the N_{TB}-forming dimers.

Here we present a comparative analysis of anisotropic material properties of N_{TB}-forming dimer and the associated rod-like 'monomer' that forms the dimer. We analyze how optical, dielectric, diamagnetic, elastic and viscous material properties in the high temperature nematic phase formed by liquid crystalline dimers deviate from the associated rod-like 'monomer' that forms the dimer. For instance, in some dimers, the temperature dependent birefringence, $\Delta n(T)$, and dielectric anisotropy, $\Delta\varepsilon(T)$, follow a nonmonotonous behavior when approaching T_{N-TB} (*2, 19, 20, 28*). In case of CB7CB dimer, we also investigate the pretransitional behavior of the elastic constants near the N-to-N_{TB} phase transition temperature to better our understanding of the formation of the N_{TB} phase.

1.2 Smart and biocompatible polymerized liquid crystal coatings

Reactive LC mesogens (such as mono- or diacrylates) allow the LC anisotropic properties to be permanently fixed via thermal or photo-polymerization processes (*29*). The resultant polymerized materials with orientational order are tentatively classified as liquid crystal networks (LCNs) and liquid crystal elastomers (LCEs) (*30*). The LCNs consist of moderate to densely crosslinked network architecture, while the LCEs are comprised of low cross-link density of side-chain and/or main-chain mesogenic units (*30*). Such polymerized materials yield wide range of anisotropic mesostructures with unique features (*29, 31, 32*). The ability to pre-program surface properties of LCNs/LCEs at the stage of their preparation makes them an excellent candidate for developing smart

surfaces (*30, 33-42*). When preparing LCE/LCN coatings, the blend of materials may consist solely of reactive mesogens (RMs) or nonreactive LCs doped with some amount of RMs. In the latter case, the nonreactive part is typically removed after polymerization using a solvent, leaving a polymerized scaffold with fixed molecular orientation. The coupling of orientational order to rubber-like elasticity allows one to use various external agents (temperature, light irradiation, static electric and magnetic fields) that modify the orientational order as a tool to trigger a mechanical response of LCNs/LCEs (*32*). One may also adjust the phase and glass transition temperatures by selecting suitable chemistry of LC moieties.

One of the intriguing issues in the problem of coupling between the orientational order and mechanical properties of the LCNs/LCEs is how the gradients of the director field can be used to achieve a predetermined change of shape. For example, Broer et al demonstrated that an LCE coating with one surface free and another attached to a rigid substrate and with the director that varies in the plane of the coating, can develop a strong variation in the thickness via an external excitation (*33-37, 39, 41-44*). The work demonstrated a huge potential for a design of "smart" coatings based on LCE with director distortions, but the general principles by which the director gradients transform into the thickness variation of the LCE coating were not clear, except for the case of a relatively simple geometry of coatings with the so-called fingerprint texture of the cholesteric LCE (*34, 35, 37, 42*). Very recently, free-standing LCE films with a preprogrammed director distortions were demonstrated to adopt a predesigned shape such as a mask of a human face when heated (*45*). In the latter case, the relationship between

the director gradients and curvature of the film can be established numerically, assuming a constant thickness of the film, but such an approach cannot be immediately extended to describe the behavior of coatings, in which the thickness change is of a prime importance.

The goal of this work was to find a relationship between the director gradients pre-inscribed in the LCE coating at the stage of preparation and the surface profile of an activated LCE coating. We present two types of activation, thermal and light-induced. Macroscopic material deformations of the crosslinked networks are triggered through the change of the tensorial order parameter of the orientational order (Figure 1-2). For example, upon heating, when the uniaxial orientational order is weakened, the material shrinks along the director and expands in the directions perpendicular to it (*30*).

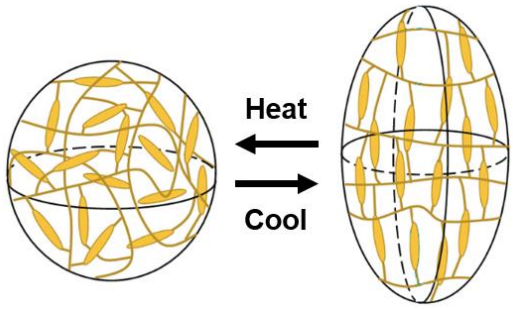

Figure 1-2. Schematic representation of the polymer network conformation upon heating/cooling the material.

The light-induced material deformations are achieved by integrating azobenze units into the blend of monomers. Azobenzene molecules have two conformations: *trans* and *cis* (Figure 1-3), where the *trans* rod-like isomer is thermodynamically more stable than its bent (*cis*) counterpart (*46*). When in the *trans* state, the azobenzine molecules align with the host LC-based matrix. Azobenzenes undergo reversible *trans-cis*

isomerization when irradiated in their absorption bands (*46, 47*). Subsequently, upon illumination with UV light, azobenzene units convert to their bent, or *cis*, state. The conformational changes of azo-moieties lead to the reduction of the liquid crystalline order (Figure 1-3) (*35*).

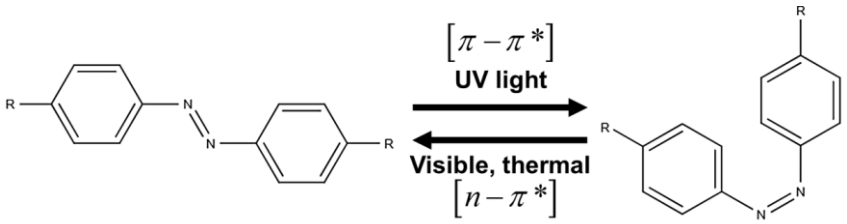

Figure 1-3. Schematic representation of *trans-cis* conformational change of azobenzene molecule.

1.3 Scope and objectives of the dissertation

The scope of this dissertation is two-fold. First, our aim is to perform a detailed analysis of temperature dependent material properties of flexible odd dimers with positive and negative anisotropies. In the case of the negative dimer, we conduct a comparative study between the dimer and the corresponding 'monomer' in the nematic phase. We find dramatic differences in the temperature dependencies of birefringence, dielectric anisotropy, and elastic constants. With an assortment of various electro- and magneto-optical techniques, we demonstrate that while the anisotropic properties of the monomer follow the classic behavior that are typical of the rod-like mesogens, the dimer that forms a twist-bend nematic phase, exhibits non-monotonous behavior of birefringence and elastic constants. We introduce a novel method of alignment of pure

liquid crystal dimers homeotropically, which allows the direct measurements of all three elastic constants for dimers with negative dielectric anisotropy.

Our second objective is to design ‘smart materials’ that change their shape, structure, and physical properties in a controlled manner when activated by external triggers. We demonstrate an approach to create an artificial preprogrammed coating that changes its surface topography when stimulated with temperature and light. The shape changes are preprogrammed by inscribing a pattern of molecular orientation at the stage of preparation of the coating, when it is totally flat. Once the coating is heated, it develops elevations, depressions and in-plane shifts of the material that are fully determined by the pre-inscribed pattern. Once cooled, the coating becomes flat again. The dynamic changes in the surface profiles are reversible. We establish a deterministic relationship between the in-plane patterns and 3D dynamic changes of the surface topography. To explain how the in-plane 2D patterns could produce a 3D dynamic shape changes when actuated by temperature, we introduce a theoretical model that connects the temperature-induced microscopic changes in the molecular structure to the macroscopic collective behavior of the material. We further employ these coatings with controlled surface topographies to 1) control placement of microparticles, and 2) guide the motility and consequently induce alignment of biological cells.

The dissertation is organized as follows.

Chapter 2 and 3 present a comprehensive set of measurements and comparative analysis of material parameters formed by a liquid crystalline dimers composed of two rigid rod-like units connected by a flexible aliphatic link. In Chapter 2 the studied dimer

is of positive dielectric anisotropy, while in Chapter 3 we focus on materials with negative dielectric anisotropy and draw a parallel to the rod-like LC that forms the dimer. In both chapters, we characterize the material parameters as functions of temperature in the N phase.

Chapter 4 demonstrates a dynamic thermal control of the surface topography of an elastomer prepared as a coating with a pattern of in-plane molecular orientation. The inscribed pattern determines whether the coating develops elevations, depressions, or in-plane deformations when the temperature changes. The deterministic dependence of the out-of-plane dynamic profile on the in-plane orientation is explained by activation forces.

Chapter 5 and 6 illustrate control of microparticle placement using LCE/LCN surfaces. In Chapter 5, we employ light-responsive, preprogrammed LCEs to guide inanimate microspheres into linear or circular chain-like aggregates. While, in Chapter 6, we guide motile human cells to follow the LCN nanotopography generated by polymerized liquid crystal defect structures.

The following publications cover the topics discussed in the dissertation:

[1]: Cukrov, G., Golestani, Y. M., Xiang, J., Nastishin, Y. A., Ahmed, Z., Welch, C., Mehl, G. H. & Lavrentovich, O. D. Comparative analysis of anisotropic material properties of uniaxial nematics formed by flexible dimers and rod-like monomers. Liquid Crystals 44, 219-231, (2017).

[2]: Babakhanova, G., Parsouzi, Z., Paladugu, S., Wang, H., Nastishin, Y. A., Shiyanovskii, S. V., Sprunt, S. & Lavrentovich, O. D. Elastic and viscous properties of the nematic dimer CB7CB. Phys Rev E 96, 062704, (2017).

[3]: Babakhanova, G., Turiv, T., Guo, Y., Hendrikx, M., Wei, Q.-H., Schenning, A. P. H. J., Broer, D. J. & Lavrentovich, O. D. Liquid crystal elastomer coatings with programmed response of surface profile. *Nat Commun* **9**, 456, (2018).

and five more publications that are currently being prepared for submission:

[4] Greta Babakhanova, Hao Yu, Irakli Chaganava, Qi-Huo Wei, Paul Shiller, Oleg D. Lavrentovich. “Controlled placement of microparticles at the water-liquid crystal elastomer interface”, *submitted to ACS Applied Materials & Interfaces.*

[5] Greta Babakhanova, Youssef Mosaddeghian Golestani, Hend Baza, Sajedeh Afghah, Hao Yu, Irakli Chaganava, Qi-Huo Wei, Paul Shiller, Jonathan V. Selinger, Robin Selinger, Oleg D. Lavrentovich. “Dynamically morphing microchannels in liquid crystal elastomer coatings containing disclinations”, *in preparation.*

[6]: Greta Babakhanova, Hao Wang, Mojtaba Rajabi, David Li, Quan Li, Oleg D. Lavrentovich. “Elastic and electro-optical properties of flexible fluorinated dimers”, *submitted to Liquid Crystals.*

[7] Greta Babakhanova, Jessie Krieger, Bing-Xiang Li, Min-Ho Kim, Oleg D. Lavrentovich. “Surface mediated cell alignment using polymerized liquid crystal nanostructures”, *in preparation.*

[8] Zeinab Parsouzi, Greta Babakhanova, Mojtaba Rajabi, Rony Saha, Prabesh Gyawali, Taras Turiv, Chris Welch, Georg H. Mehl, James Gleeson, Antal Jákli, Oleg D. Lavrentovich, and Samuel Sprunt. “Pretransitional behavior of orientational elasticities and viscosities at the uniaxial to twist-bend nematic phase transition in dimer, trimer, and tetramer homologues”, *submitted to Physical Chemistry Chemical Physics.*

CHAPTER 2

Flexible dimers with positive dielectric anisotropy

2.1 Introduction

Liquid crystals spectacularly illustrate how subtle variation in molecular structure leads to dramatic changes in the macroscopic properties of a material. Rigid rod-like molecules such as 4′-pentyl-4-cyanobiphenyl (5CB) are known to form the nematic (N) phase with a long range orientational order and no positional order; in the N phase, the rod-like molecules are on average aligned along a single direction, specified by a unit vector $\hat{\mathbf{n}}$ called the director; because of its non-polar nature, $\hat{\mathbf{n}}=-\hat{\mathbf{n}}$. However, when two cyanobiphenyl moieties are linked into a single molecule by a flexible aliphatic chain with an odd number of methyl groups, as in the case of 1,7-bis-4-(4′-cyanobiphenyl) heptane (CB7CB), (Figure 2-1), a new, lower temperature nematic phase, the so-called twist-bend nematic (N_{TB}), emerges (*1, 2, 14*). This phase exhibits a uniform mass density but a spatially modulated and locally chiral director field. The director precesses helically on a cone with an extremely small period (pitch), measured by transmission electron microscopy (TEM) (*1*, *2*) to be about 8 nm. The nanoscale heliconical geometry is evidenced by characteristic textures of asymmetric Bouligand arches in freeze-fracture TEM observations (*2*) and by resonant X-ray scattering (*9*).

The dimer material CB7CB, in addition to N_{TB}, also exhibits another twist-bend structure, the so-called oblique helicoidal cholesteric, Ch_{OH}, when doped with a small

amount of chiral additive and subjected to an externally applied electric (*24, 25*) or magnetic (*26*) field. Here again, the experimental observations followed earlier theoretical predictions by Meyer (*11*) and de Gennes (*27*). In an ordinary cholesteric, the molecules twist in a helical fashion with the director remaining perpendicular to the helical axis. In the Ch_{OH} structure, the director twists while making an angle $\theta < \pi / 2$ with the twist axis and the direction of the applied field. The tilt introduces bend in addition to twist. However, when the bend elastic constant is small, the elastic energy penalty for bend is compensated by the dielectric energy gain associated with the nonzero projection of the local director on the field direction. Geometrically, the director structure of the Ch_{OH} is similar to that of the N_{TB} phase, but the pitch P of the Ch_{OH} is typically much larger than the nano-scale pitch of the N_{TB}, since the molecules in the Ch_{OH} can rotate around their long axes (*48*), while the local structure of N_{TB} inhibits this rotation and is essentially biaxial. Both θ and P in Ch_{OH} are explicit functions of the applied field and the ratio K_{33} / K_{22} (*11, 25*). The sensitivity of the pitch to the electric field makes it possible to realize electrically controlled selective reflection of light (*24*) and lasing (*49*) within broad spectral ranges, which are potentially useful effects for practical applications of Ch_{OH}. The important parameter to optimize in these applications is the ratio K_{33} / K_{22}, which depends on temperature. Elastic constant measurements are crucial to explore the potential for this optimization.

The sensitivity of both N_{TB} and Ch_{OH} to the elastic constants of the corresponding material in its N state motivates the work reported in this chapter. In particular, we experimentally determine the temperature dependence of all three bulk elastic constants

in the entire range of the nematic phase of the dimer CB7CB. These three constants are deduced from the dynamic light scattering (DLS) data and also, in the case of splay constant, from the Frederiks transition threshold in the electric field. The elastic properties of CB7CB have been explored in the past (*16, 17, 22, 50, 51*), but the data obtained by different groups differ from each other rather substantially.

To date, the most complete study has been presented by Yun et al (*16*) who determined the temperature dependencies of all three bulk elastic constants by an electro-optical technique. Yun et al (*16*) used a Frederiks transition in a planar cell to determine the splay elastic constant K_{11} from the threshold of director deformations caused by an applied electric field. As the field increases, the initial pure splay mode of deformations is replaced by a mixed splay-bend distortion. By fitting the capacitance response of the cell with an analytical expression in which the elastic parameter is of the form $\kappa = (K_{33} - K_{11})/K_{11}$, one can extract the value of K_{33} since K_{11} is known. The method has been originally proposed for nematics formed by rod-like molecules (*52*), in which K_{33} is significantly larger than K_{11}, so that the fitting parameter κ is large and the fitting of extrapolated response is robust. In the case of dimers, however, it is expected that the largest elastic constant is K_{11} while K_{33} is the smallest (*14, 15, 18, 20*). Therefore, the low energy cost of bend distortions and small contribution of K_{33} to the fitting parameter κ makes the extrapolation approach less robust for the dimers. The ratio K_{11}/K_{22} was found to be around 1.4, i.e., smaller than 2, near the N- N_{TB} phase transition (*16*). The result is somewhat surprising, since the inequality $K_{11}/K_{22} > 2$ represents a criterion of

the formation of the N_{TB} phase as opposed to a splay-bend phase. The very fact of the twist-bend deformations in the low-temperature nematic phase has been established in the case of CB7CB by the freeze-fracture transmission microscopy studies (*1, 2*) and by the resonant carbon soft X-ray scattering (*9*). Sebastian et al and Lopez et al (*17, 22*) used the same extrapolation technique of splay Frederiks transition to determine K_{11} and K_{33}; it was found that as the temperature decreases towards the N-N_{TB} transition, K_{11} monotonously increases while K_{33} first increases and then decreases. The values of K_{11} determined in (*17, 22*) were somewhat higher (by $\approx$ 4-5%) than those in Ref. (*16*), while the values of K_{33} in (*17, 22*) were higher than those in Ref. (*16*) by approximately a factor of 2, depending on the temperature. Qualitatively different results were presented by Parthasarathi et al (*51*) who reported that as the temperature is lowered towards the N-N_{TB} transition in pure CB7CB, the bend constant K_{33} increases rather than decreases.

In this chapter, we use direct and complementary techniques to determine all three elastic constants of CB7CB as well as other material parameters. The electro-optic version of the Frederiks effect is used only to find the splay elastic constant K_{11} from the direct measurements of the threshold voltage needed to cause director distortions. To find the bend and twist constants and to independently determine the splay constant, we use dynamic light scattering (DLS). The two independently determined values of K_{11} served as a test of reliability.

In DLS, light is scattered at fluctuations of the director which is the local optic axis of the nematic. By designing a proper geometry of the experiment (polarizations,

incident and scattering angles), one can separate contributions of different modes of deformations and, in particular, probe the deformations of pure bend. As we demonstrate in this paper, this extraction of bend is especially well suited for the dimeric materials in which K_{33} is the smallest of all three bulk constants. Furthermore, besides the direct information about the elastic properties, the DLS data, with a proper calibration, also yield the values of orientational viscosities, corresponding to the relaxation dynamics of splay, bend, and the predominantly twist component of twist-bend deformations, as described by Majumdar et al (*53*) and Zhou et al (*54*); these viscosities are presented as functions of temperature. Finally, this work presents results on other material properties of CB7CB, including refractive indices, birefringence, dielectric permittivities and diamagnetic anisotropy.

2.2 Materials and Methods

2.2.1 Chemical structure, phase diagram, and alignment

The chemical structure and the phase diagram of CB7CB are shown in Figure 2-1. Phase characterization was performed upon cooling with the rate of $0.1\,^{\circ}/\mathrm{min}$ using polarizing optical microscopy (POM). The temperature was controlled with an Instec HCS402 hot stage and mK2000 temperature controller with a temperature stability of $0.01\,^{\circ}\mathrm{C}$. The CB7CB was synthesized by Hao Wang (Liquid Crystal Institute) following the procedures reported by Chen et al (*1*). Planar alignment was promoted by spin-coating PI2555 (HD Microsystems) polyimide layer on indium tin oxide (ITO)-coated glass substrates. The uniform alignment was achieved by rubbing the substrates with a

velvet cloth. The cells were assembled with anti-parallel arrangement of the rubbing direction. The cell gap d was controlled by Micropearl glass spacers (mixed with NOA 71 UV glue), and measured using a Perkin Elmer UV/VIS Spectrometer Lambda 18. All the experimental cells were filled by capillary action in the isotropic (I) phase. Figure 2-2 shows the POM textures of the N and N_{TB} phases in a planar cell ($d = 18.9\ \mu m$).

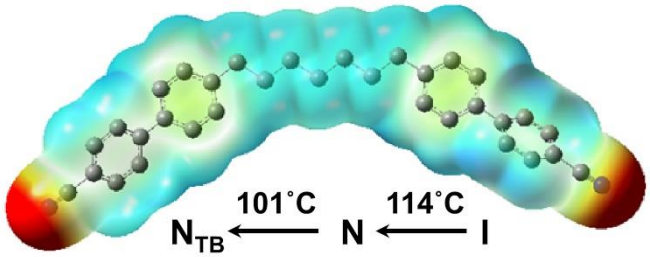

Figure 2-1. Molecular structure of CB7CB with electrostatic potential surface and phase diagram upon cooling (negative and positive electric charges excesses are shown as red and blue, respectively).

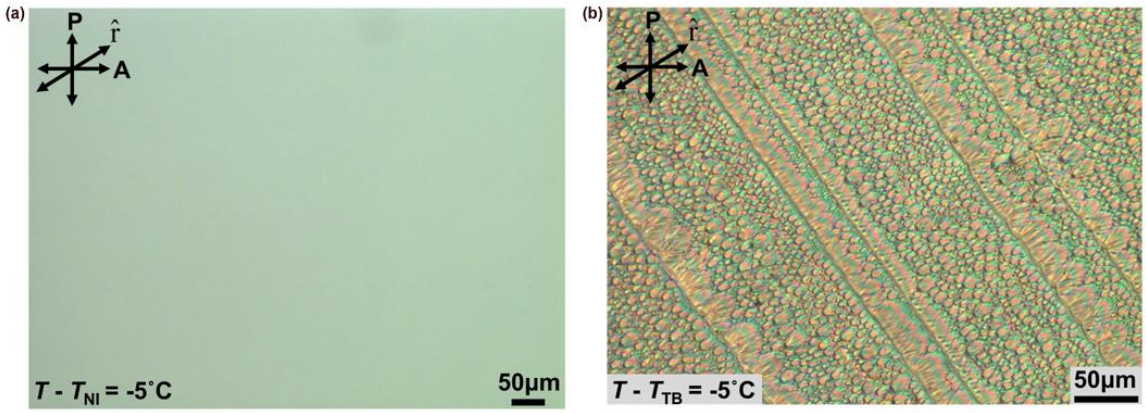

Figure 2-2. POM textures of CB7CB under cross polarizers showing uniformly aligned (a) N and (b) N_{TB} phases with focal conic domains. The direction of rubbing is shown by the axis $\hat{r}$.

2.2.2 Refractive indices and birefringence

We used the wedge-cell technique (*55*) to determine the ordinary n_o and extraordinary n_e refractive indices of CB7CB. The wedge cell was prepared using planar, rubbed ITO substrates assembled in antiparallel fashion such that the rubbing direction was perpendicular to the wedge thickness gradient. The pretilt angle in the planar substrates measured using crystal rotation method (*56*) is less than $1°$. The thickness of the thick part of the wedge was set by a stripe of NOA 71 glue with pre-mixed Micropearl glass spacers. Initially, the optical interference technique described in (*55*) was used to determine the angle of an empty wedge, by shining a Helium-Neon (He-Ne) laser beam ($\lambda = 633$ nm) onto the cell and recording an interference pattern under the POM. The temperature dependence of the wedge angle was determined over the same temperature range as the nematic range. The wedge cell was then filled with CB7CB by capillary action in the I phase. The analyzer (A) and polarizer (P) were aligned parallel to each other. Their orientations with respect to the nematic director were chosen to explore n_o and n_e independently. When polarization directions of both A and P are perpendicular or parallel to $\hat{\mathbf{n}}$, the multiple-beam interference in the wedge cell yielded n_o or n_e, respectively, according to the following equation

$$n_{o,e} = \frac{l\lambda}{2\alpha(s_{m+l}^{o,e} - s_m^{o,e})}, \tag{2-1}$$

where l is the interference order (i.e. the fringe number), λ is the wavelength of probing light, α is the wedge angle, and $(s_{m+l}^{o,e} - s_m^{o,e})$ is the distance between the interference maxima (*55*).

The birefringence, Δn, was measured by the Senarmont technique (*57*). The experimental optical set-up is displayed in Figure 2-3. First, a polarizer and analyzer (positioned on motorized rotational stage), were crossed for maximum extinction. A quarter-wave plate was placed such that the optical axis is parallel to the initial polarizer. The planar cell ($d = 10.1\ \mu\text{m}$) was introduced with the rubbing direction, $\hat{\mathbf{r}}$, making an angle $\varphi_o = 45°$ with the fist polarizer. The sample was probed with He-Ne laser light. For each temperature scan, the analyzer was rotated until the intensity of the linearly polarized light emerging from the quarter-wave plate reached a minimum (I_{min}) corresponding to an angle β. The maximum error of the angle measurements was $1°$. The total phase retardation was calculated as $\Delta\Phi = 2\beta + N2\pi$, where N is an integer number, and the resultant birefringence is determined as

$$\Delta n = \frac{\lambda}{2\pi d}\Delta\Phi \ . \tag{2-2}$$

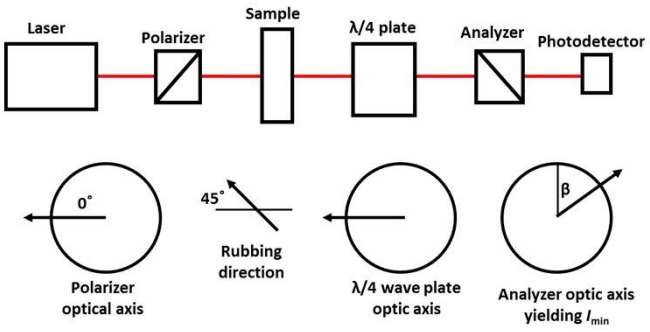

Figure 2-3. Senarmont experimental set-up for birefringence measurements.

To diminish the contribution from experimental errors, we fitted the measured Δn and $(n_e + n_o)$ data with a polynomial fit and obtained smoothed data for the temperature dependence for the refractive indices, according to the equation:

$$n_{e,o} = \frac{(n_e + n_o) \pm (n_e - n_o)}{2} \ . \qquad (2\text{-}3)$$

2.2.3 Electro-optical measurements

Dielectric characterization was performed using a precision LCR meter 4284A (Hewlett Packard). Temperature-dependent dielectric permittivities were calculated from the capacitance measurements on a planar cell ($d = 18.9\ \mu$m) of CB7CB. A voltage (V) up to 20 V_{rms} was applied across the active area of the patterned ITO electrodes. The square ITO patterned area was 25 mm^2. The measurements were performed at frequencies: $f = 5, 10, 20, 40$ and 60 kHz. No significant dissipation was observed in the range 5-200 kHz. The perpendicular component of dielectric permittivity $\varepsilon_\perp$ was calculated from capacitance measurements at low voltages, below the Frederiks threshold, whereas the parallel component $\varepsilon_\parallel$ was determined by extrapolation method at high voltages. The cell capacitance C was plotted as a function of V to find the splay Frederiks threshold voltage (V_{th}) by the double-line extrapolation method. The splay elastic constant K_{11} was then calculated according to (*58*)

$$K_{11} = \frac{\varepsilon_o \Delta\varepsilon V_{th}^2}{\pi^2}, \qquad (2\text{-}4)$$

where $\Delta\varepsilon = \varepsilon_\parallel - \varepsilon_\perp$ and ε_o is the vacuum permittivity.

2.2.4 Diamagnetic anisotropy

The diamagnetic anisotropy, $\Delta\chi = \chi_\parallel - \chi_\perp$, where $\chi_\parallel$ and $\chi_\perp$ are the diamagnetic susceptibilities parallel and perpendicular to the director, was determined utilizing a

planar cell ($d = 18.9\ \mu\text{m}$) placed in a uniform magnetic field applied perpendicular to the bounding plates (Figure 2-4). The sample was positioned between two crossed polarizers with the rubbing direction $\hat{\mathbf{r}}$ making an angle of $45°$ with the polarizer axes. The director reorientation caused by the splay Frederiks transition was monitored via transmitted light intensity data. Subsequently, the magnetic threshold (B_{th}) was extrapolated from measurements of the optical phase retardance vs. magnetic field curve using a double-line extrapolation approach. The values of $\Delta\chi$ were calculated by relating electric and magnetic splay Frederiks effects according to (*58*)

$$\Delta\chi = \varepsilon_{\text{o}}\mu_{\text{o}}\Delta\varepsilon\left(\frac{V_{\text{th}}}{dB_{\text{th}}}\right)^2, \tag{2-5}$$

where $\mu_{\text{o}} = 4\pi\times10^{-7}\ \text{H m}^{-1}$ is the vacuum permeability.

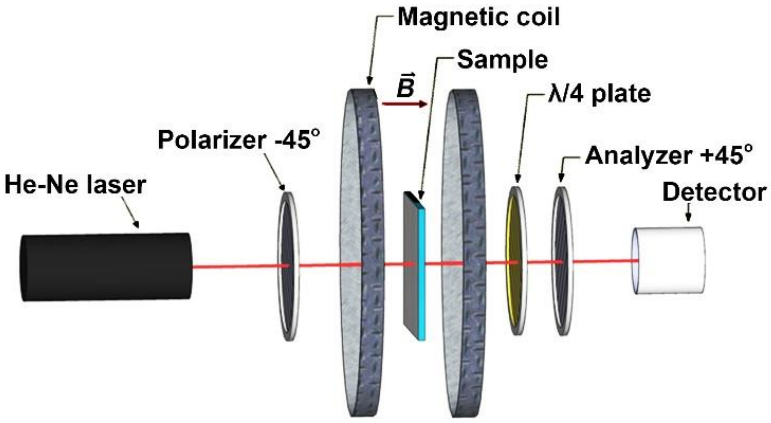

Figure 2-4. Optical set-up to determine $\Delta\chi$.

2.2.5 Dynamic light scattering

Dynamic light scattering (DLS) on planar cells ($d = 16.5\ \mu\text{m}$) of CB7CB was conducted as a function of temperature on cooling. In order to obtain the absolute values of K_{11}, K_{22} and K_{33}, we additionally recorded light scattering from a sample of the well-characterized calamitic nematic 4-*n*-octyloxy-4*'*-cyanobiphenyl (8OCB), for which the elastic constants and refractive indices are known with high precision (*59-61*). The 8OCB experiments were performed at selected temperatures and under the same experimental conditions as for CB7CB, using a planar cell ($d = 14.4\ \mu\text{m}$). Specifically, 8OCB and CB7CB cells were situated in the same plane and placed adjacent to each other in the scattering apparatus. They could then be translated into or out of the incident laser beam by turning a single micrometer, with no other effect on the state or parameters of the experiment. High quality of homogeneous $\hat{n}$ alignment was confirmed by POM, performed in situ on the DLS set-up. Phase transition temperatures of test samples were checked both before and after the experiment.

In the light scattering set-up, the output of a He-Ne laser (Spectra-Physics, model 127), with a wavelength $\lambda_o = 633\ \text{nm}$, incident power of 4 mW, and polarization oriented perpendicular to the scattering plane, is focused onto a spot on the sample with diameter ~50 μm. The hot stage containing the control and test samples was installed on a three-stage goniometer that allowed independent adjustment of the incident angle (set to normal incidence), the scattering angle, and the angle of the director $\hat{\mathbf{n}}$ with respect to the scattering plane. This flexibility enabled us to isolate scattering from three components of

the director fluctuations: pure bend (K_{33}), twist-bend mode dominated by twist (K_{22}), and pure splay (K_{11}) (Figure 2-5). In each case, depolarized scattered light was collected through a pinhole-lens-optical fiber detection layout. Scattered photons were converted to electronic pulses through a photomultiplier-amplifier-discriminator combination, allowing homodyne time correlation functions of the scattered intensity to be computed on a digital correlator.

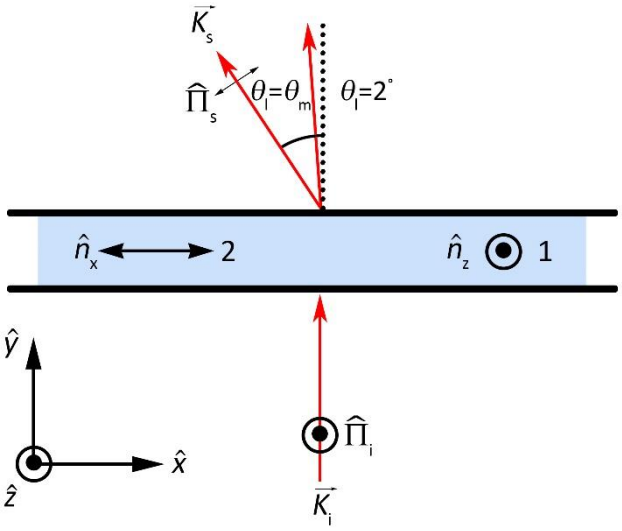

Figure 2-5. Light scattering geometries. "1": splay+twist scattering; "2": pure bend scattering ($\theta_l = \theta_m$) and predominantly twist scattering ($\theta_l = 2°$). $\vec{K}_i$ and $\vec{K}_s$ correspond to incident and scattering wave vectors respectively; θ_l is scattering angle measured in the laboratory frame; θ_m refers to the so-called "magic angle"; Π_i and Π_s indicate the light of incident polarization and scattering polarizations which are orthogonal to each other.

In splay+twist geometry "1" of Figure 2-5, the scattering vector $\vec{q}$ representing the difference between the incident and scattered wave-vectors, $\vec{q} = \vec{K}_s - \vec{K}_i$, is perpendicular to the director $\hat{n}$ ($\vec{q} = \vec{q}_\perp$). In this case, splay and twist fluctuations

contribute simultaneously to the scattering. The measured light intensity (divided by the incident light intensity I_o) for normal incidence is given by (*62*):

$$\frac{I_{ST}(\theta_l)}{I_o} = (\Delta\varepsilon')^2(\pi\lambda^{-2})^2\Omega d A k_B T\left[\frac{G_1(\theta_l)}{K_{11}q_\perp^2(\theta_l)} + \frac{G_2(\theta_l)}{K_{22}q_\perp^2(\theta_l)}\right], \quad (2\text{-}6)$$

where θ_l is scattering angle in the laboratory, $\Delta\varepsilon'$ is optical dielectric anisotropy defined as $\Delta\varepsilon' = n_e^2 - n_o^2$, λ is the wavelength of light, T is the absolute temperature, Ω is collection solid angle, A is the cross-sectional area of the illuminated sample volume, and d is the sample thickness. $G_1(\theta_l)$ and $G_2(\theta_l)$ are geometrical scattering factors dependent on n_o, n_e and θ_l. By choosing the scattering angle to be the so-called "magic angle", $\theta_m = \sin^{-1}\left(n_o\sqrt{1-\frac{n_o^2}{n_e^2}}\right)$, the contribution of twist fluctuation mode to the total intensity disappears, so that $I_S(\theta_m) \propto \frac{G_1(\theta_m)}{K_{11}q_\perp^2(\theta_m)}$. In this case, we can extract the elastic constant K_{11}. The fitted n_o and n_e values of CB7CB at the same wavelength as used for DLS were used to determine θ_m at each temperature. The calculated values of θ_m vary over $33° - 40°$ within the N range. For the 8OCB control sample, we used literature values of the refractive indices to obtain θ_m (*63*).

In geometry "2" ("twist-bend" geometry), where $\hat{n}$ lies in scattering plane, the scattering comes from a combination of the twist-bend normal mode of director fluctuations (*62*):

$$\frac{I_{\mathrm{TB}}(\theta_{\mathrm{l}})}{I_{\mathrm{o}}} = (\Delta\varepsilon')^2(\pi\lambda^{-2})^2\Omega dAk_{\mathrm{B}}T\left[\frac{G_3(\theta_{\mathrm{l}})}{K_{33}q_{\|}^2(\theta_{\mathrm{l}}) + K_{22}q_{\perp}^2(\theta_{\mathrm{l}})}\right]. \tag{2-7}$$

Here $G_3(\theta_{\mathrm{l}})$ is a geometrical factor appropriate to the twist-bend geometry. At a low experimental scattering angle of $\theta_{\mathrm{l}} = 2°$, the ratio $\frac{q_{\perp}^2(\theta_{\mathrm{l}})}{q_{\|}^2(\theta_{\mathrm{l}})} \approx 15$. Since we also know that $K_{22} \gg K_{33}$ for dimer molecules with odd-numbered spacers (*15, 18, 20*), we conclude that $K_{22}q_{\perp}^2(\theta_{\mathrm{l}}) \gg K_{33}q_{\|}^2(\theta_{\mathrm{l}})$ for $\theta_{\mathrm{l}} = 2°$, so that, to an excellent approximation, only twist fluctuations contribute in the above expression for the scattered intensity. On the other hand, when $\theta_{\mathrm{l}} = \theta_{\mathrm{m}}$, one finds that $q_{\perp}^2(\theta_{\mathrm{m}}) = 0$ (*62*), and in this case only bend fluctuations are probed. Thus, by switching from very small θ_{l} to $\theta_{\mathrm{l}} = \theta_{\mathrm{m}}$, we can selectively probe the elastic constants K_{22} and K_{33}.

As mentioned previously, in order to obtain the absolute values of the moduli, pure splay, bend, or twist scattering from CB7CB must be calibrated against the corresponding scattering from 8OCB. Literature values of optical parameters ($n_{e,8\mathrm{OCB}} = 1.65$, $n_{o,8\mathrm{OCB}} = 1.50$) (*61*) and elastic constants ($K_{11,8\mathrm{OCB}} = 5.5$ pN, $K_{22,8\mathrm{OCB}} = 2.9$ pN and $K_{33,8\mathrm{OCB}} = 6.05$ pN) (*59, 60*) at $T - T_{\mathrm{NI}} = -6$ °C were used in order to calculate intensity ratios between the 8OCB and CB7CB samples at fixed temperature ($T - T_{\mathrm{NI}} = -9$ °C). That enables a straightforward calculation of the elastic constants of CB7CB.

DLS also provides information on the orientational viscosities. At optical frequencies the director fluctuation modes are overdamped, and the standard expression for the homodyne intensity correlation function is (*64*),

$$\langle I(0,\theta_1)I(\tau,\theta_1)\rangle = I(\theta_1)^2\left[1+e^{-2\Gamma(\theta_1)\tau}\right], \tag{2-8}$$

where $\Gamma(\theta_1)$ is the relaxation rate of the fluctuations, and τ is the correlation delay time. Fits of the correlation data to this expression give the relaxation rates for the two director normal modes (*62*):

$$\Gamma_\alpha(\theta_1) = \frac{(K_{33}q_{||}^2 + K_\alpha q_\perp^2)}{\eta_\alpha(\vec{q})},\ \alpha = 1,2, \tag{2-9}$$

The viscosities $\eta_\alpha(\vec{q})$ are combinations of the Leslie and Miesowicz viscosities of the nematic. From the scattering geometries described above, values of the elastic moduli, and the fitted relaxation rates, we calculate the orientational viscosities for pure bend and splay scattering geometries as (*64*):

$$\eta_{\text{splay}} = \frac{K_{11}q_\perp^2}{\Gamma_1(\theta_{\text{m}})} = \eta_1(q_\perp) = \gamma_1 - \frac{\alpha_3^2}{\eta_b}, \tag{2-10}$$

$$\eta_{\text{bend}} = \frac{K_{33}q_{||}^2}{\Gamma_2(\theta_{\text{m}})} = \eta_2(q_{||}) = \gamma_1 - \frac{\alpha_2^2}{\eta_c}, \tag{2-11}$$

where $\gamma_1, \alpha_2, \alpha_3, \eta_b, \eta_c$ are fundamental viscosities of the nematic fluid discussed in standard texts (*62*).

The corresponding orientational diffusivities, D, are found using the following relationships (*62*):

$$D_{\text{splay}} = \frac{K_{11}}{\eta_{\text{splay}}}, \tag{2-12}$$

$$D_{\text{bend}} = \frac{K_{33}}{\eta_{\text{bend}}}, \tag{2-13}$$

In the case of the twist-bend mode (geometry "2") for small scattering angle $\theta_1 \approx 2°$ and $\frac{q_\perp^2}{q_\parallel^2} \approx 15$, the orientational viscosity becomes (*62*)

$$\eta_{\text{twist-bend}} = \frac{K_{22} q_\perp^2}{\Gamma_2(\theta_1 = 2°)} = \eta_2(q_\perp^2 \approx 15 q_\parallel^2) \approx \gamma_1 - \frac{\alpha_2^2}{\eta_a}\frac{q_\parallel^2}{q_\perp^2} \approx \gamma_1 - \frac{\alpha_2^2}{15\eta_a}. \tag{2-14}$$

In contrast to the situation with the elastic constants, the orientational viscosity $\eta_{\text{twist-bend}}$ cannot be reasonably approximated by the pure twist contribution ($\eta_{\text{twist}} = \gamma_1$), since the value of $\frac{\alpha_2^2}{\eta_a}$ in Equation 2-14 is typically rather large. For example, using reported values of $\alpha_2 \approx -0.083$ Pa s and $\eta_a \approx 0.040$ Pa s for the standard monomeric calamitic 5CB (*58, 65*), we have $\frac{\alpha_2^2}{\eta_a} = 0.17$ Pa s at a temperature 10°C below isotropic-nematic transition, which means that in CB7CB the last term in Eq. (2-14) is $\sim 14\%$ of the reported value of $\gamma_1 = 0.08$ Pa s. Thus, in the following section we report the orientational viscosity in Eq. (2-14) and the corresponding diffusivity

$$D_{\text{twist-bend}} = \frac{K_{22}}{\eta_{\text{twist-bend}}}. \tag{2-15}$$

2.3 Results

2.3.1 Refractive indices and birefringence

The values of measurements of the principal refractive indices and the birefringence at $\lambda = 633$ nm are presented in Figure 2-6.

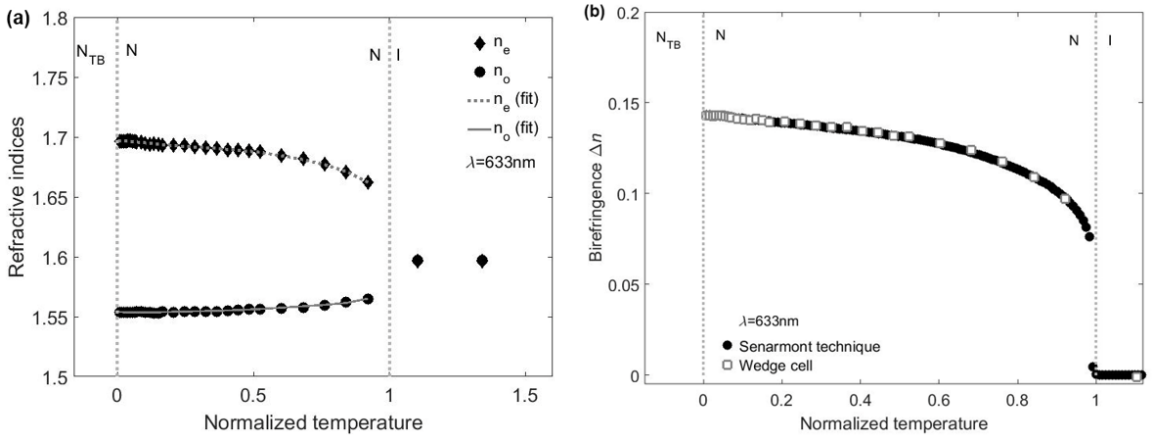

Figure 2-6. (a) Refractive indices of CB7CB ($\lambda = 633$ nm); filled symbols represent the data acquired using a planar wedge cell; dotted and solid lines represent the fitted values of n_o and n_e respectively; (b) Δn measured at $\lambda = 633$ nm using Senarmont technique (circles), planar wedge cell (squares).

The birefringence is positive and increases monotonically with decreasing temperature through the nematic phase down to the N-N_{TB} transition.

2.3.2 Dielectric and diamagnetic properties

Both components of dielectric permittivity ($\varepsilon_{\parallel}$ and $\varepsilon_{\perp}$) are presented in Figure 2-7a as functions of temperature. Figure 2-7b shows that, upon cooling from the I phase, $\Delta\varepsilon$ first significantly increases and then monotonously decreases. Changing the

frequency in the range $f = 5 - 60$ kHz did not significantly affect the temperature dependent behavior of the dielectric constants.

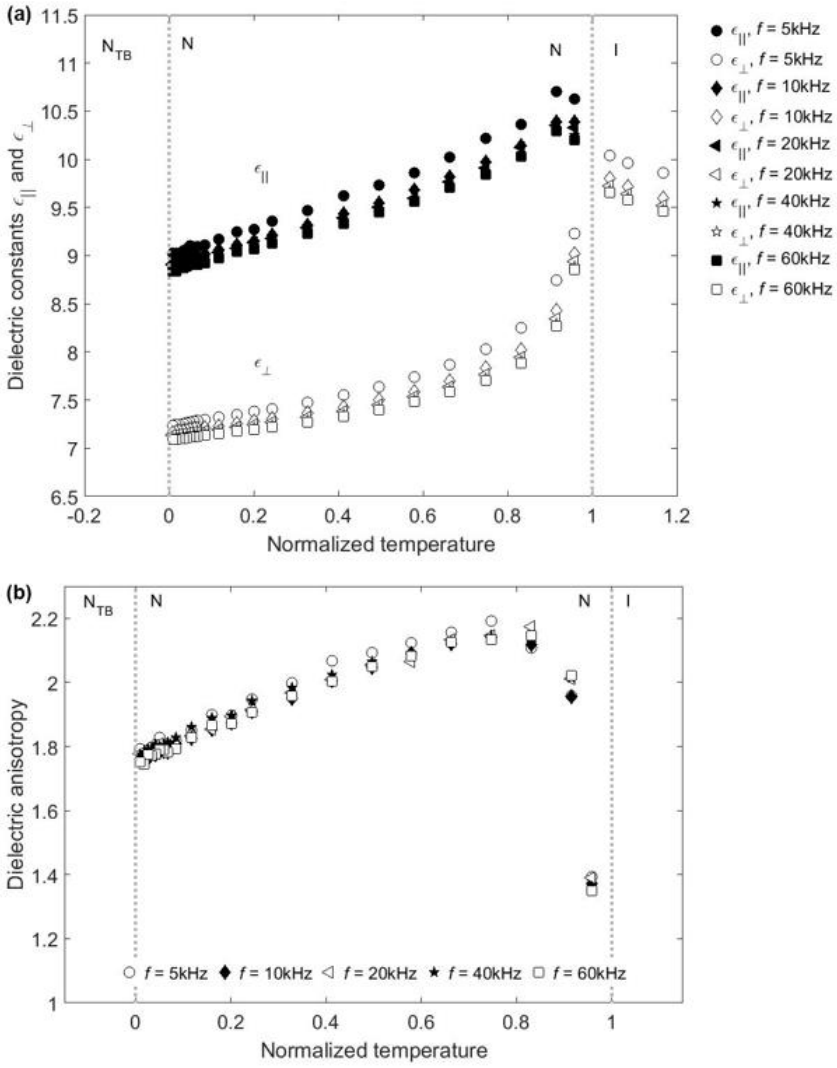

Figure 2-7. (a) Parallel and perpendicular components of temperature dependent dielectric constants and (b) $\Delta\varepsilon$ measured at $f = 5, 10, 20, 40$ and 60 kHz using a planar cell ($d = 18.9$ μm) of CB7CB.

The diamagnetic anisotropy presented in Figure 2-8a has a sharp increase near the I-N transition. It grows with decreasing temperature and saturates towards the N-N_{TB} transition. The data were fitted with a Haller's rule (*66*) of the form

$$\Delta\chi = \chi_o\left(1-\frac{T}{T*}\right)^{\nu} \tag{2-16}$$

where $\chi_o = 2.1493\times10^{-6}$, $T* = 384.75$ and $\nu = 0.10953$ are the fitting parameters. The scalar nematic order parameter S was calculated using the relationship $S = \frac{\Delta\chi(T)}{\chi_o}$, and is presented in Figure 2-8b.

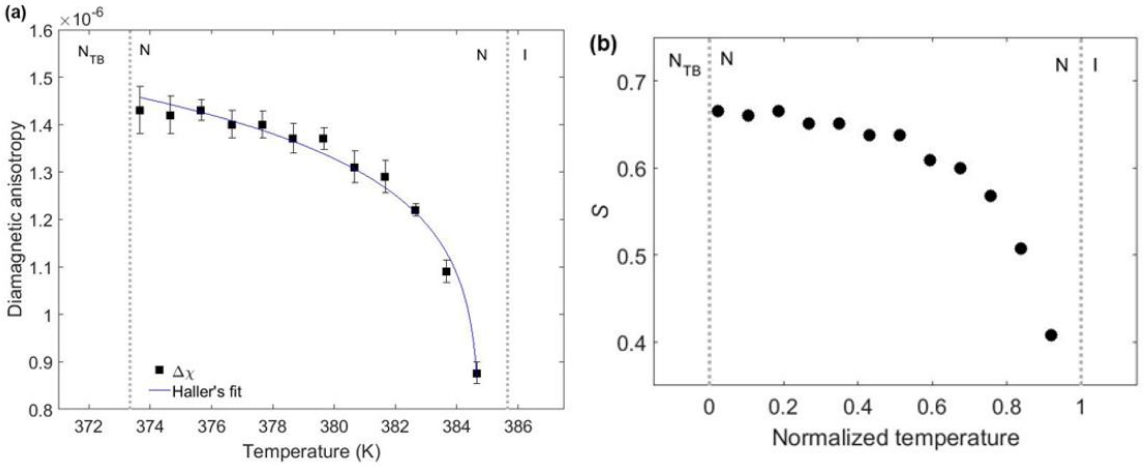

Figure 2-8. (a) Temperature dependence of $\Delta\chi$ fitted with Haller's rule and (b) orientational order parameter of CB7CB.

2.3.3 Elastic constants

We performed direct measurements of all three elastic constants of CB7CB by the methods described above. The geometries described in section 2.2.5 for DLS

measurements allowed us to isolate the fluctuations related to splay, twist and bend. The independently calculated values of K_{11}, K_{22} and K_{33} from the intensity measurements are presented in Figure 2-9a. The Frederiks transition method was also employed to further assure the validity of DLS results. The results of capacitance measurements at $f = 60$ kHz yielding K_{11} are presented in Figure 2-9a. On cooling, K_{11} weakly increases in the entire N range. There is also a slight increase in K_{22}, which is more prominent near the N-N_{TB} transition. The most striking behavior, however, is seen in the development of K_{33} as the temperature approaches the N_{TB} phase, Figure 2-9b. On cooling through higher temperatures in the N phase K_{33} increases slightly; however, on further cooling the value dramatically decreases approaching about 0.4 pN, after which there is a sharp growth near the N-N_{TB} transition. The temperature-dependent elastic constant ratios, K_{11}/K_{22}, K_{33}/K_{22} and K_{11}/K_{33}, are presented in Figure 2-10.

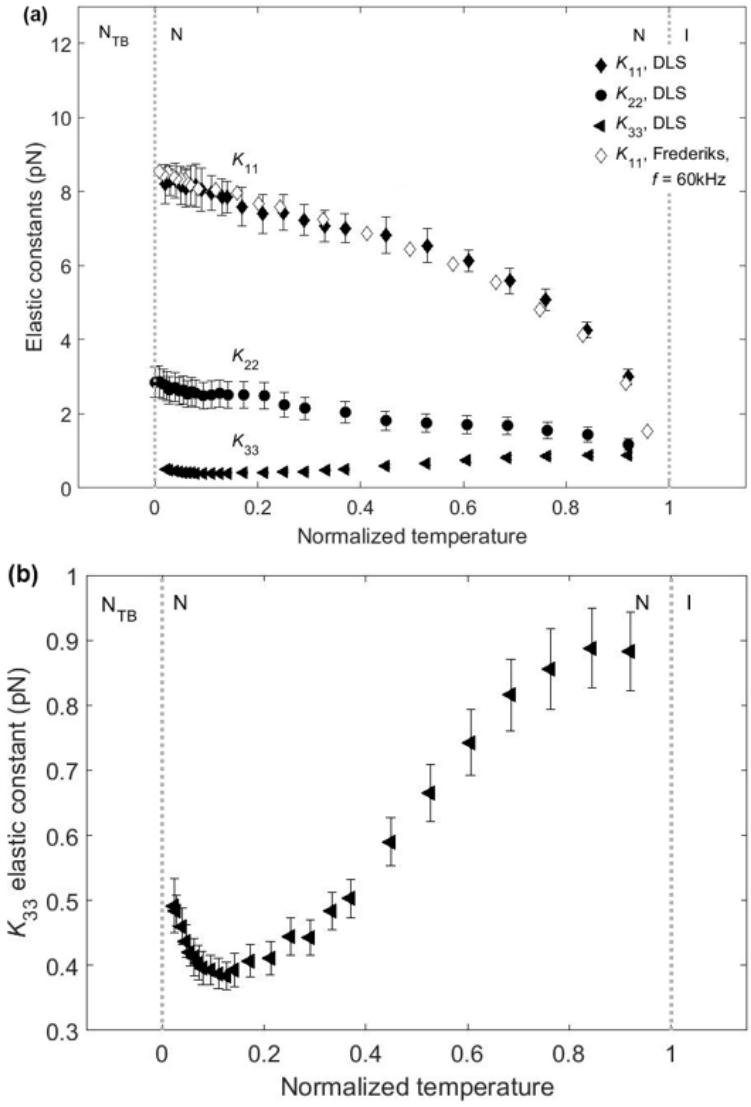

Figure 2-9. (a) K_{11}, K_{22} and K_{33} data of CB7CB obtained using DLS and K_{11} data obtained using capacitance method at $f = 60$ kHz; (b) temperature behavior of K_{33} (DLS method).

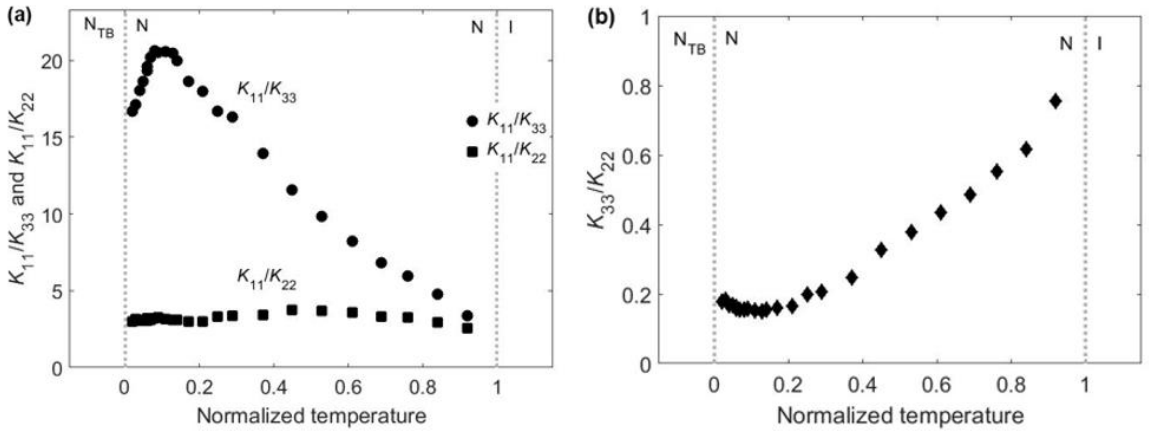

Figure 2-10. Ratios of elastic constants of CB7CB (a) K_{11}/K_{33} and K_{11}/K_{22}, (b) K_{33}/K_{22} from DLS data.

The temperature dependence of the three orientational viscosities, η_{splay}, η_{bend}, and $\eta_{\text{twist-bend}}$ are displayed in Figure 2-11; they tend to increase upon cooling, especially on approaching the N_{TB} phase. The corresponding diffusivities defined in Eqs. (2-12,2-13,2-15) are presented in Figure 2-12. As temperature is lowered from the I phase, $D_{\text{twist-bend}}$ remains practically constant, D_{splay} gradually decreases, and D_{bend} sharply decreases and levels off near the N-N_{TB} transition.

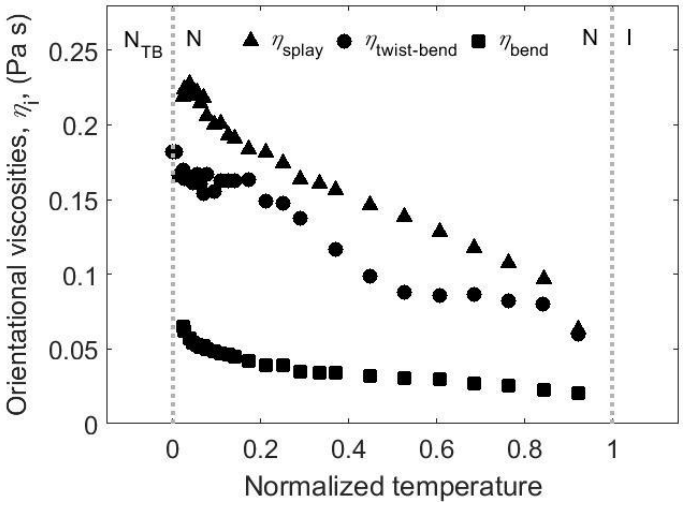

Figure 2-11. Temperature dependence of orientational viscosities of CB7CB.

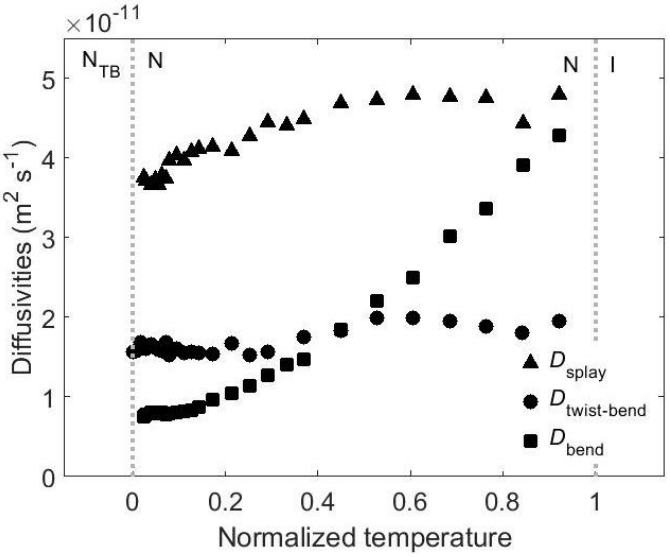

Figure 2-12. Temperature dependence of orientational diffusivities of CB7CB.

2.4 Discussion

The temperature dependence of the refractive indices and birefringence of CB7CB in the N phase is similar to that of ordinary calamatic liquid crystals such as 5CB

as well as bent-core liquid crystals (*63, 65, 67-73*). On cooling, the extraordinary refractive index increases and the ordinary index decreases. The birefringence Δn (Figure 2-6b) is positive and grows with increasing orientational order. The temperature dependence of Δn measured by us at 633 nm is in good agreement with the data by Meyer et al at $\lambda = 546$ nm (*74*) and Tuchband et al at $\lambda = 656.3$ nm (*75*).

The measured temperature dependency of dielectric anisotropy $\Delta\varepsilon$ differs from that of Δn. Upon cooling, Δn increases monotonously (Figure 2-6b), while $\Delta\varepsilon$ first slightly increases near the clearing point, then it decreases (Figure 2-7b). The difference between $\Delta\varepsilon(T)$ and $\Delta n(T)$ should not come as a surprise, as at optical frequencies, the electrical polarizability of nematics (and thus Δn) reflects electronic and atomic polarizabilities (*58, 76*), while the value of $\Delta\varepsilon$ at lower frequencies is also influenced by the orientational polarizability. The difference in contributing mechanisms to $\Delta\varepsilon$ and Δn is well known in the studies of rod-like mesogens, see, for example, Refs. (*76, 77*).

The tendency of the perpendicular component of permittivity to decrease on cooling is similar to that for monomeric liquid crystals with $\Delta\varepsilon > 0$ (*14*). However, the parallel component of the dielectric permittivity does not behave as in a typical calamitic nematic with $\Delta\varepsilon > 0$, where $\varepsilon_{\parallel}$ is expected to increase on cooling. In CB7CB, $\varepsilon_{\parallel}$ increases slightly just below the I-N transition, but upon further cooling it rolls over and begins to decrease. As seen in Figure 2-7, the decrease in $\varepsilon_{\parallel}$ leads to a decline in $\Delta\varepsilon$. Our experimental results are in good agreement with other dielectric studies of CB7CB

and its longer homologues (*14, 16, 18, 21, 22, 51, 78-80*) and can be qualitatively explained as follows.

In CB7CB, the molecular net dipole moment is determined mostly by the orientation of two cyanobiphenyl groups (*14, 21, 22*). The flexible dimers respond to changes in temperature by modifying their conformations (*14, 81-84*). Theoretical models of flexible dimers suggest that there are two main populations of conformers, extended and hairpin-like, that vary in the angle between the two terminal cyanobiphenyl units (*14*). This angle is about $120°$ for the extended conformers and $30°$ for the hairpin conformers. While the hairpin conformers might contribute substantially to the overall dielectric permittivity near the clearing point, their population should diminish as the temperature is lowered and the packing density increases. At the same time, the population of extended conformers should be growing as the order parameter increases upon cooling (*14*). The extended conformers with the angle between two terminal groups above $90°$ should have a vanishing longitudinal dipole moment (*21, 22*). The effect of increased number of the extended conformers might contribute to the observed decrease of $\varepsilon_{\parallel}$ upon cooling in Figure 2-7a. Besides the orientation of the dipole groups, their relative position might also contribute to the unusual temperature dependence of permittivity. A non-monotonous temperature dependence of $\Delta\varepsilon$ is known for the nematics formed by rod-like and bent-core molecules near the transition of the N phase to the smectic-A (SmA) phase (*68, 76, 77*). In SmA, the molecules are arranged in layers, with their long axes being perpendicular to these layers. The spacing between the molecules within SmA layers is shorter than the distance between different planes. This

packing feature enhances antiparallel dipole correlations within the layers, decreasing the effective longitudinal dipole moment and thus decreasing $\varepsilon_{\parallel}$ and $\Delta\varepsilon$ (*76*, *77*). Although the nematic phases of CB7CB do not show smectic modulations of density, enhancement of antiparallel correlations of the dipole moments located at the neighboring molecules might also contribute to the observed decrease of $\varepsilon_{\parallel}$ and $\Delta\varepsilon$.

The diamagnetic anisotropy of CB7CB is positive, and, as expected, the temperature dependence is similar to that of the birefringence. The values of $\Delta\chi$ saturate near the N-N_{TB} transition. The extrapolated values of the orientational order parameter using Haller's fit show that the scalar order parameter S varies between 0.41 and 0.67, which is consistent with the reported values (*74*, *85*).

Figure 2-11 shows the temperature dependent orientational viscosities that obey a relationship $\eta_{\text{twist-bend}} \approx \eta_{\text{splay}} > \eta_{\text{bend}}$ in the entire nematic range. As already discussed, see Eq. (2-14), the value of $\eta_{\text{twist-bend}}$ cannot be approximated by the pure rotational viscosity γ_1, since one expects $\eta_{\text{twist-bend}} > \gamma_1$. The value of η_{splay} is about 2 times larger than that in 5CB, while η_{bend} is 10-20% smaller than in 5CB (*65*). The increase of η_{splay} in CB7CB as compared to 5CB can be associated with the increase of the molecular length (*65*). One expects $\eta_{\text{splay}} > \eta_{\text{bend}}$ for conventional rod-like mesogens (*86*). For rigid bent-core molecules, Majumdar et al reported $\eta_{\text{bend}} \approx \eta_{splay}$, with bend viscosity being slightly, by about 10% higher than the splay viscosity (*53*). The relative smallness of η_{bend} observed in our studies of CB7CB is apparently caused by the tendency of odd-numbered dimers to adopt bent conformations.

The main focus of this dissertation was to determine the elastic constants in the most accurate and complete fashion. In order to achieve this goal, we used direct measurements by two independent techniques, DLS and Frederiks transition. The elastic moduli obtained in our work and the results of similar studies by other groups for CB7CB are presented in Table I and discussed below. Since the literature values of the nematic range of CB7CB vary, we normalized the temperature (T_{norm}) of the N phase, where T_{norm}=0 and T_{norm}=1 represent N-N_{TB} and I-N transitions respectively. Table I presents the data for two normalized temperature points $T_{norm} \approx 0.1$ and ≈ 0.2. In our set-up for CB7CB, these temperatures corresponds to ∼102.3 ˚C and ∼103.6 ˚C respectively. The literature values of K_{11}, K_{22}, K_{33} for CB7CB were taken from the supplementary material in Ref. (*16*) as well as from the figures in Refs. (*17, 22, 51*). Experimental errors presented in Table I were calculated by error propagation method for DLS data and by measuring the symbol size in plots presented in Refs. (*16, 17, 22, 51*).

Table 2-1. Elastic constants and their ratios of CB7CB dimer, 8OCB calamitic mesogen (I-N-SmA transitions), bent-core mesogens 12-F (I-N-SmA) and A131 (I-N-SmC) at $T_{\text{norm}} \approx 0.1$ and 0.2. The normalized temperature equals 1 at the I-N transition point and 0 at the transition point from N to the lower-temperature phase.

Material	T_{norm}	K_{11} (pN)	K_{22} (pN)	K_{33} (pN)	$\frac{K_{11}}{K_{22}}$	$\frac{K_{11}}{K_{33}}$	Reference
CB7CB	0.1	8.0 ± 0.5	2.5 ± 0.4	0.39 ±0.02	3.2	21	DLS (this work)
CB7CB	0.1	7.2 ± 0.3	5.2 ± 0.5	0.3 ± 0.1	1.4	24	Ref. (*16*)
CB7CB	0.1	7.6 ± 0.2	-	0.6 ± 0.2	-	13	Ref. (*22*)
CB7CB	0.1	7.0 ± 0.2	-	3.8 ± 0.3	-	1.8	Ref. (*51*)
CB7CB	0.1	7.6 ± 0.3	-	0.5 ± 0.3	-	15	Ref. (*17*)
CB7CB	0.2	7.4 ± 0.5	2.4 ± 0.4	0.41 ± 0.03	3.1	18	DLS (this work)
CB7CB	0.2	6.9 ± 0.3	4.9 ± 0.3	0.3 ± 0.1	1.4	23	Ref. (*16*)
CB7CB	0.2	7.2 ± 0.2	-	0.6 ± 0.2	-	12	Ref. (*22*)
CB7CB	0.2	6.8 ± 0.2	-	3.7 ± 0.3	-	1.8	Ref. (*51*)
CB7CB	0.2	7.1 ±0.3	-	0.6 ± 0.3	-	12	Ref. (*17*)
8OCB	0.1	7.3 ± 0.1	4.0 ± 0.1	13.1 ±0.1	1.8	0.56	Ref. (*60*)
8OCB	0.2	6.8 ± 0.1	3.5 ± 0.1	9.5 ± 0.1	1.9	0.72	Ref. (*60*)
12-F	0.1	6.7 ± 0.5	-	9.4 ± 0.4	-	0.71	Ref.(*68*)
12-F	0.2	6.2 ± 0.5	-	5.9 ± 0.3	-	1.1	Ref.(*68*)
A131	0.1	15.4 ± 0.3	-	11.6 ± 0.3	-	1.3	Ref. (*87*)
A131	0.2	13.9 ± 0.3	-	6.7 ± 0.3	-	2.1	Ref. (*87*)

Splay. The splay modulus data measured by our two methods agree with each other within the error bars, Figure 2-9a. Upon cooling, K_{11} grows monotonously, and obeys the relationship $K_{11} > K_{22}, K_{33}$ throughout the entire N range. The K_{11} values are in a reasonable agreement with the literature data obtained by measuring capacitance of cells experiencing the splay Frederiks transition (*16, 17, 22, 51*), Table I. The major source of the error in the DLS measurements is the variation of the measured light intensity values. We minimized that error by measuring the light intensity of each data point by two independent channels for ten minutes.

Twist. The dependence $K_{22}(T)$ measured by DLS shows a typical increase as the temperature is lowered. The rate of this increase becomes higher near the N-N_{TB} phase transition, within about 1.2˚C of the transition point. The absolute values, however, are lower than the values reported for K_{22} in Ref. (*16*), by a factor of ~ 2 near the N-N_{TB} transition. The authors in Ref. (*16*) used the electric Frederiks transition in a twisted nematic (TN) cell and in a planar cell with in-plane switching (IPS). According to Ref. (*16*), the obtained values of K_{22} are not accurate because of difficulties in determining the threshold voltage V_{th} in the TN cells and because of field inhomogeneity in the IPS cells. The ratio K_{11}/K_{22} measured in our work is consistently higher than 2.5 in the entire N range of CB7CB, while Ref. (*16*) reports that on average $K_{11}/K_{22} \approx 1.4$. Note here that the twist-bend phase has been predicted to be stable only when $K_{11}/K_{22} > 2$, as opposed to the splay-bend case in which one expects $K_{11}/K_{22} < 2$ (*10, 13*).

Bend. The most striking temperature dependence is observed for K_{33}. Our DLS data show an overall decrease of K_{33} upon cooling, down to ≈ 0.4 pN near the N-N_{TB} transition, after which K_{33} grows within 1.5˚C interval just before the transition. A similar pretransitional slight increase of K_{33} was already observed for CB7CB and other dimeric liquid crystals (*15, 17, 18, 20-22*), with the exception of Ref. (*51*) which reported K_{33} monotonously increasing as the temperature is lowered. In Refs. (*16, 17, 22, 51*) K_{33} was determined by using the splay Frederiks transition and measuring the cell's response well above the threshold voltage at which pure splay gives rise to mixed splay-

bend; extrapolation to infinite fields yields K_{33}. When $K_{33} \ll K_{11}$, this extrapolation might be less accurate than in the conventional case of $K_{33} > K_{11}$. Furthermore, as the electric field increases above threshold, director deformations give rise to flexoelectric polarization that renormalizes the extrapolated value of the elastic constants. In particular, Brown and Mottram (*88*) demonstrated that in the conventional nematic E7, the extrapolated values of K_{33} obtained from the splay Frederiks effect in a planar cell are significantly influenced by this flexoeffect. In the case of CB7CB, the flexoelectric effect can be significant, see, for example, (*89, 90*). Thus the extrapolation technique should be supplemented by an independent analysis of how the flexoelectric effect can influence the extrapolated K_{33}.Thus far, only our DLS experiments provide a direct measurement of K_{33}. The data show that the splay-bend anisotropy of the elastic constants in CB7CB is huge, $K_{11} / K_{33} \sim 21$, which implies that the one-constant approximation ($K_{11} = K_{22} = K_{33}$) often used in theory will not be accurate for CB7CB.

Table I also compares the elastic moduli of CB7CB to those of other nematics, formed by conventional rod-like and rigid bent-core molecules with underlying smectic phases. Again, we use normalized temperature to make the comparison, where T_{norm}=0 represents N-SmA/SmC transition. 8OCB is a calamitic liquid crystal which exhibits N-SmA transition (*60*). Bent-core compound (4*'*-fluoro phenyl azo) phenyl-4-yl 3-[*N*-(4*'*-*n*-dodecyloxy 2-hydroxybenzylidene)amino]-2-methyl benzoate abbreviated as 12-F, exhibits SmA phase (*68*), while the second bent-core material, 4-[(4-

dodecylphenyl)diazenyl] phenyl 2-methyl-3-[4-(4-octylbenzoyloxy) benzyledeneamino] benzoate, abbreviated as A131, exhibits SmC phase (*87*).

Nematic phases of 8OCB, F-12 and A131, listed in Table 2-1, all exhibit a substantial pretransitional increase of K_{33} when temperature is cooled down from T_{norm} = 0.2 to T_{norm} = 0.1. The effect is usually explained by the proximity of the smectic phase in which the condition of layers equidistance is incompatible with the director bends and twists; above the transition, in the N phase, formation of cybotactic clusters with periodic layer spacing makes twist and bend elastic constants relatively large (*60, 63, 68, 87*). Even though the N_{TB} phase of CB7CB does not exhibit periodic mass density modulation, the periodic director structure limits twist and bend (*20*). Thus, the mechanism responsible for the observed pretransitional increase of K_{22} and K_{33} near N-N_{TB} phase transition in CB7CB, Figure 2-9, may be analogous to that of other materials near the N-SmA/SmC phase transitions, where K_{22} and K_{33} diverge.

The results presented in this work and in Refs. (*15, 18, 20*) demonstrate that the typical elastic constants relationship for the N phase of dimers exhibiting the N_{TB} phase is of the type $K_{33} < K_{22} < K_{11}$. For rod-like calamitic nematics such as 8OCB, Table 2-1, the relationship is $K_{22} < K_{11} < K_{33}$ (*20, 23, 60, 91*). In the case of bent-core nematics, however, the elastic constant relationship is not universal, and it is largely dependent on the bend angle (*73, 92*). Few reports show that $K_{33} > K_{11}$ (*68, 73, 93*). There are also observations of an anomalous temperature behavior, similar to dimers, with $K_{33} < K_{11}$ (*53, 68, 72, 87, 94*). The bent shape of the rigid bent-core molecules might explain the

anomalously small K_{33} (*87*). The reduction of the bend elastic constant by the molecular curvature has already been predicted by Gruler and Helfrich (*95, 96*).

2.5 Conclusion

We experimentally determined the temperature-dependent optical, dielectric, diamagnetic and elastic and viscous material properties of the most studied odd methylene-linked dimer, CB7CB, in its nematic phase. We determined that on cooling, the refractive indices behave much like the regular calamatic liquid crystals such as 5CB. The dielectric measurements reveal that the parallel component of dielectric permittivity decreases on approach to the N-N_{TB} transition after an initial increase below the isotropic phase, while the perpendicular component decreases monotonically. The resultant dielectric anisotropy has a sharp increase below the clearing temperature, but then rolls over and gradually decreases on approaching the N-N_{TB} transition. These results are consistent with the dimers adopting a more bent (less extended) average conformation as the N-N_{TB} transition is approached.

We also reported the first independent temperature dependent measurements of all three elastic constants for CB7CB. In our study we employed direct measurements of all three elastic constants with very small temperature steps near N-N_{TB} phase transition. We show that the relationship $K_{11} > K_{22} > K_{33}$ holds true in the entire nematic range, with $K_{11} / K_{22} > 2$ as predicted by the theory for a system that exhibits the N_{TB} phase (*10, 13*). K_{11} increases monotonously; K_{22} also increases gradually but has a more prominent pretransitional increase close to the N-N_{TB} phase transition. The temperature dependence

of K_{33} is the most dramatic – on cooling from the I-N transition it decreases to an unusually low value ≈ 0.38 pN and then experiences pretransitional increase near the N-N_{TB} transition. The pretransitional increase of both K_{22} and K_{33} might be explained by formation of clusters with periodic twist-bend modulation of the director close to N_{TB} phase transition. These clusters lead to an increase of K_{22} and K_{33} since the equidistance of pseudolayers hinders twist and bend deformations of the director. A similar pretransitional increase of K_{22} and K_{33} is well documented near the nematic-to-smectic A phase transition (*60, 97, 98*). The ratio K_{33} / K_{22} that controls the field-tunable range of the heliconical structure (*99*) is less than 1 in the entire N range, thus making CB7CB a good candidate for preparation of heliconical cholesterics with a tunable pitch.

Finally, the measured values of all three orientational viscosities increase on cooling, showing steeper slopes near the N-N_{TB} phase transition. The bend orientational diffusivity sharply decreases on cooling from T_{NI} and saturates near T_{NTB}. The splay diffusivity decreases smoothly, whereas, on average, the twist diffusivity remains constant throughout the nematic range.

CHAPTER 3

Comparative analysis of anisotropic material properties of uniaxial nematics formed by flexible dimers and rod-like mesogens with negative dielectric anisotropy

3.1 Introduction

Research data presented in chapter 2 indicate that the dimeric materials feature elastic properties very different from those of rod-like nematogens. The goal of the work presented in this chapter is to determine the temperature dependencies of basic material properties, such as dielectric anisotropy $\Delta\varepsilon$, birefringence Δn, and elastic constants of splay K_{11}, twist K_{22} and bend K_{33} of the N phase formed by the dimeric molecules of 1,5-Bis(2′,3′-difluoro-4′′pentyl-[1,1′:4′1′′-terphenyl]-4-yl)nonane (DTC5C9) and to compare them to the corresponding values in the N phase formed by its 'monomer' 2′,3′-difluoro-4,4′′-dipentyl-*p*-terphenyl (MCT5). For materials with a positive dielectric anisotropy, the standard approach to measure K_{11} is to use a single uniformly aligned planar cell and apply the electric field across it; K_{33} is than extrapolated from the fitted K_{11} data. A suitable direct method for measuring K_{33} of LCs with negative dielectric anisotropy is a bend Frederiks transition (Figure 3-1) caused by an external electric field in a homeotropic cell, in which the director is perpendicular to the bounding plates and parallel to the applied field. Since the dielectric anisotropy is negative, the director reorients perpendicular to the applied electric field direction.

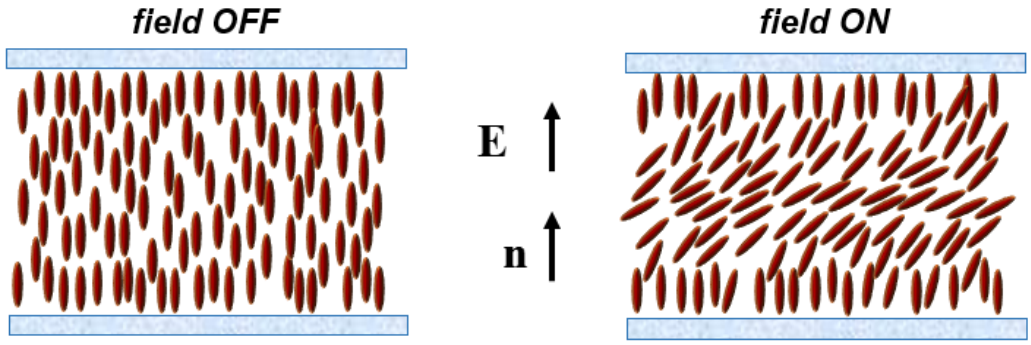

Figure 3-1. Schematic representation of the bend Frederiks transition. In the field off state (left panel), the LC ($\Delta\varepsilon < 0$) is oriented homeotropically. After the threshold voltage (right panel), the director experiences reorientation. Since the dielectric anisotropy is negative, the molecules in the bulk align perpendicular to the applied electric field.

To date, however, homeotropic alignment of pure dimeric nematics has not been achieved. Borshch et al (*2*) used homeotropic cells of a 7:3 mixture of DTC5C9 and MTC5, to measure K_{33} directly (0.8 pN near T_{Ntb}). Here we present a novel dual-alignment layer which yields homeotropic alignment for fluorinated dimers. Thus, all elastic constants are determined directly, by detecting the threshold of the Fredericks transitions for splay and twist in planar cells and for bend in homeotropic cells.

Our results demonstrate that the monomer behavior is in line with the models based on rod-like building units, in which the ratios of the elastic constants such as K_{11}/K_{33} and K_{22}/K_{33} are practically temperature-independent, while all the constants grow as the temperature is lowered. In contrast, DTC5C9 dimer shows a strong temperature dependence of K_{11}/K_{33} and K_{22}/K_{33}. The ratio K_{11}/K_{22} remains larger than 2 as expected for the material capable of forming the N_{TB} phase as opposed to the

splay-bend phase. Both K_{11} and K_{22} increase strongly when the temperature is lowered; K_{33} exhibits a non-monotonous temperature dependence, first growing and then decreasing as the material is cooled down from T_{NI}. Near T_{NTB}, K_{33} reaches very small values, about 0.4 pN, that is more than one order of magnitude smaller than the corresponding value for MCT5.

3.2 Materials and methods

3.2.1 Chemical structure, phase diagram and alignment

Figure 3-2 shows the chemical structures and the phase diagrams of the two studied materials, the monomer MCT5 (Figure 3-2a) and the dimer DTC5C9 (Figure 3-2b). MCT5 was acquired from Kingston Chemicals Limited, while DTC5C9 was synthesized by G.M. and co-workers. MCT5 shows N phase, while DTC5C9 exhibits N phase at high temperatures and N_{TB} phase at lower temperatures. The presence of the N_{TB} phase in DTC5C9 was established on the basis of the polarizing-microscopy textures showing the characteristic stripes and focal conic domains (Figure 2-2d), similar to those observed in other studies of the N_{TB} phase (*2, 14, 100-102*). DTC5C9 behavior mirrors broadly that of analogues with shorter and longer internal spacers and mesogens with negative dielectric anisotropy (*103-107*). The clearing temperature of DTC5C9 increases in strong magnetic fields, with a rate ~0.6 ^{o}C/T (*108*); in all our experiments, we used magnetic field less than 1 T. Note that the formation of the N_{TB} phase has been demonstrated by transmission electron microscopy for the 7:3 mixture of DTC5C9 and MCT5 (*2*).

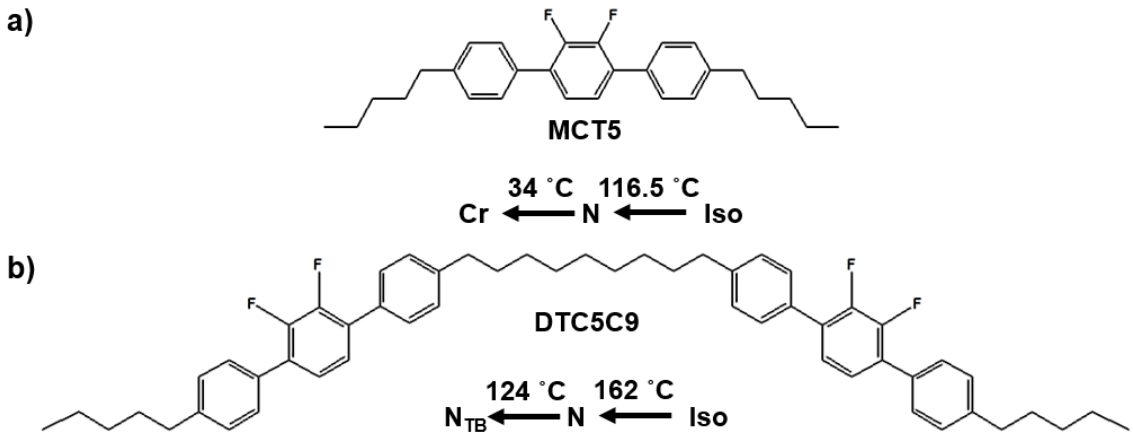

Figure 3-2. Chemical structures and phase diagrams of the liquid crystal monomer MCT5 (a) and dimer DTC5C9 (b) with negative dielectric anisotropy. The phase diagram was determined on cooling at the rate of 0.1°C/min from the isotropic phase.

To realize stable homeotropic alignment for fluorinated dimers and MCT5, we developed the following procedure. First, the ITO glass was cleaned in the ultrasonic bath at 60 °C for 30 minutes, rinsed in deionized (DI) water for three minutes and rinsed with an Isopropyl Alcohol (IPA). To evaporate the solvent, the substrates were placed in an oven preheated to $T = 90$ °C. After drying, the ITO glass was treated with UV ozone for 15 minutes. Subsequently, the substrates were immersed and agitated in 1 wt% aqueous solution of Dimethyloctadecyl[3-(trimethoxysilyl)propyl]ammonium chloride (DMOAP) (Sigma-Aldrich) for 25 minutes. The substrates were than rinsed with DI water for three minutes, dried with Nitrogen gas and cured in an oven at $T = 110$ °C. Lastly, the second alignment layer, SE5661 mixed with a thinner, Solvent 79, with 1:1 ratio (Nissan Chemical Industries), was spin-coated at 500 rpm (3 sec), 3000 rpm (30 sec), 50 rpm (1 sec) on ITO substrates. After the spin-coating procedure, the substrates were soft-baked

at $T = 80$ °C for 10 minutes, and, finally, baked at $T = 180$ °C for 55 minutes. The homeotropic alignment was stable in the entire N range, Figure 3-3a,b and Figure 3-4a,b.

Planar alignment was achieved by using rubbed polyimide PI2555 layers (HD Microsystems), Figure 3-3c,d and Figure 3-4c,d. On cooling the homeotropic and planar cells, the N - N_{TB} transition is clearly evidenced by a propagating front that quenches fluctuations of the director in the N phase. All textural observations were performed using a polarizing optical microscope (POM) [Nikon, Optiphot-2 Pol] equipped with a home-made hot stage with the temperature control accuracy 0.1 °C. The cells thickness d was set by silicon microspheres of a calibrated diameter dispersed in a UV-curable glue; d was measured with a light interference technique using a spectrometer.

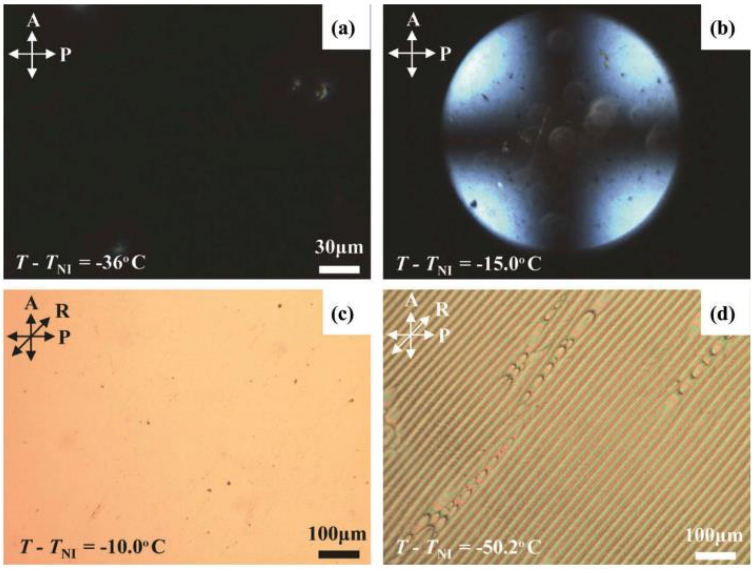

Figure 3-3. Polarizing optical microscope textures of DTC5C9 in the (a,b) homeotropic N cell ($d = 19.4\,\mu m$) and (c) planar N cell ($d = 21.5\,\mu m$); (d) planar N_{TB} cell with stripes and focal conic domains ($d = 21.5\,\mu m$). Part (b) shows the conoscopic pattern

characteristic of a homeotropic uniaxial nematic. The director in part (c) is along the rubbing direction R; polarizer and analyzer are labelled as P and A.

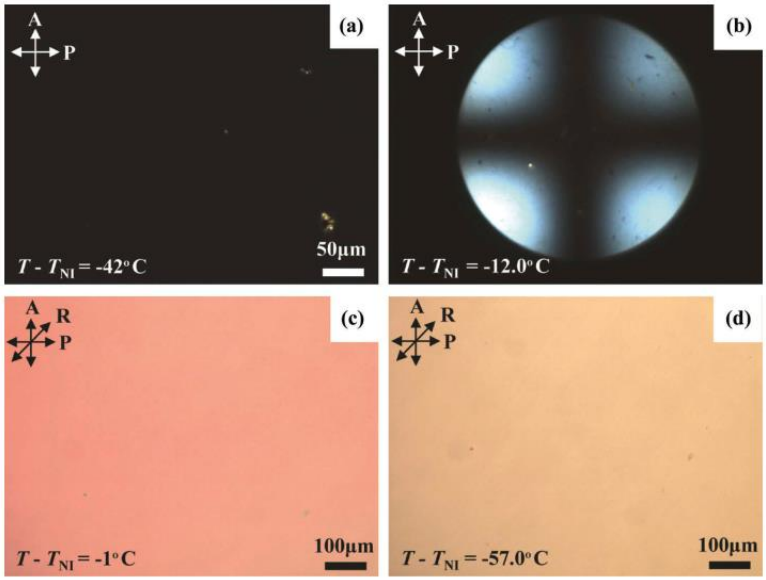

Figure 3-4. Polarizing optical microscope textures of MCT5 in the (a,b) homeotropic N cell (cell thickness $d = 19.5\,\mu m$); (c,d) planar N cell ($d = 19.5\,\mu m$). Part (b) shows the conoscopic pattern characteristic of a homeotropic uniaxial nematic. The director in part (c) and (d) is along the rubbing direction R.

3.2.2 Dielectric anisotropy

For dielectric characterization, we used LCR meter (HP4284A) to measure the capacitance of the cells. The dielectric measurements of MCT5 were performed using a planar cell with $d = 19.3 \pm 0.1\,\mu m$; and a homeotropic cell with $d = 19.5 \pm 0.2\,\mu m$. For the measurements of DTC5C9, we used a planar cells with $d = 21.5 \pm 0.2\,\mu m$; and a homeotropic cell with $d = 37.6 \pm 0.2\,\mu m$. Dielectric permittivities were measured using an AC electric field at frequencies $f = 40$ kHz for MCT5 and $f = 10$ kHz for DTC5C9.

The relatively high frequency of the field assured that the flexoelectric and surface polarization contributions (*109*) to the electro-optical response of the cell are minimized. The dielectric permittivity $\varepsilon_{\parallel}$ was determined from the capacitance of the homeotropic cells, while $\varepsilon_{\perp}$ was measured using the planar cells; $\Delta\varepsilon = \varepsilon_{\parallel} - \varepsilon_{\perp}$ is negative in the entire N range for both materials, Figure 3-6.

3.2.3 Birefringence

The temperature dependence of the birefringence Δn for MCT5 and DTC5C9 was determined by measuring the optical retardance, $\Gamma = \Delta n d$, on cooling at a rate of 2.0°C/min using LC PolScope (Abrio Imaging System) (*110*, *111*), Figure 3-7. The sample was probed with a monochromatic light of wavelength $\lambda = 546$ nm. The accuracy of the retardance measurements is not worse than 1 nm. The measurements of Δn were performed using planar cells of thicknesses $d = 3.56 \pm 0.05$ μm for MCT5 and $d = 5.09 \pm 0.05$ μm for DTC5C9.

3.2.4 Elastic constants

The elastic constant of splay K_{11} was obtained by determining the magnetic threshold, B_{th1}, of the splay Frederiks transition in a planar sample caused by the magnetic field applied perpendicularly to the bounding plates. The director reorientation was probed by measuring the transmitted light intensity passing normally through the LC cell between crossed polarizers. K_{11} was determined from the relationship (*58*)

$$K_{11} = \left(\frac{dB_{th1}}{\pi} \right)^2 \frac{\Delta\chi}{\mu_o}, \qquad (3\text{-}1)$$

where B_{th1} is the magnetic threshold, $\Delta\chi$ is the diamagnetic anisotropy, and $\mu_o = 4\pi \times 10^{-7}\ \mathrm{H \cdot m^{-1}}$.

There are several approaches to measure K_{22}, such as the Frederiks transition in a twisted nematic (TN) cell (*112*), in-plane realignment in a planar cell (*113*), a dynamic light scattering method (*114*), etc. The measured value of K_{22} in these methods is usually less accurate than those of K_{11} and K_{33}, since the twist deformations are accompanied by bend and splay. For example, in the TN method, K_{22} depends on K_{11} and K_{33}, so that the errors in K_{11} and K_{33} are accumulated into the value of K_{22}. In the in-plane switching cell method, K_{22} is independent of K_{11} and K_{33}, but the electric field within the cell is not uniform, resulting in an additional source of errors (*115*). To avoid these complications, we use the twist Frederiks transition caused by the magnetic field acting on a planar cell in such a way that the field is perpendicular to the director but lies in the plane of the cell. At a certain threshold, B_{th2}, the uniform cell experiences pure twist deformation, which allows us to determine the twist elastic constant as (*58*)

$$K_{22} = \left(\frac{dB_{th2}}{\pi} \right)^2 \frac{\Delta\chi}{\mu_o}. \qquad (3\text{-}2)$$

We used a planar sample placed between two crossed polarizers and tested transmittance of a He-Ne laser beam ($\lambda = 632.8\ \mathrm{nm}$). At normal incidence because of the polarization-

guiding regime, called the Mauguin regime, the probing light polarization follows the liquid crystal director and consequently is insensitive to the twist deformation inside the LC cell (*85, 116*). No Frederiks threshold can be registered in this case. To avoid the Mauguin regime, we use an experimentally verified approach (*85, 116, 117*), in which the laser beam is directed at an oblique incidence varying between 7-14˚. The output light intensity is measured as a function of the magnetic field to determine B_{th2} and thus K_{22}. The experimental evidence of overcoming of the Mauguin regime with the oblique light incidence is brought about by the successful registration of the magnetic threshold B_{th2}.

In order to obtain K_{33}, we applied an AC electric field using LCR meter and measured the voltage dependence of the transmitted light passing through a homeotropic cell. We applied 40 kHz for MCT5; 10 and 40 kHz for DTC5C9 measurements. The bend Frederiks threshold, V_{th3}, was determined from the optical phase retardation vs voltage curve using the so-called double extrapolation approach (*57, 118*), from which the value of K_{33} was extracted, (*58*)

$$K_{33} = \frac{\varepsilon_o \Delta\varepsilon V_{th3}^2}{\pi^2}. \qquad (3\text{-}3)$$

Figure 3-5 illustrates the typical field dependence of optical phase retardation used to find V_{th3} by double extrapolation. We also employed the capacitance method (*119*) for determining the bend elastic constant using the capacitance vs voltage dependency measured for a homeotropic cell.

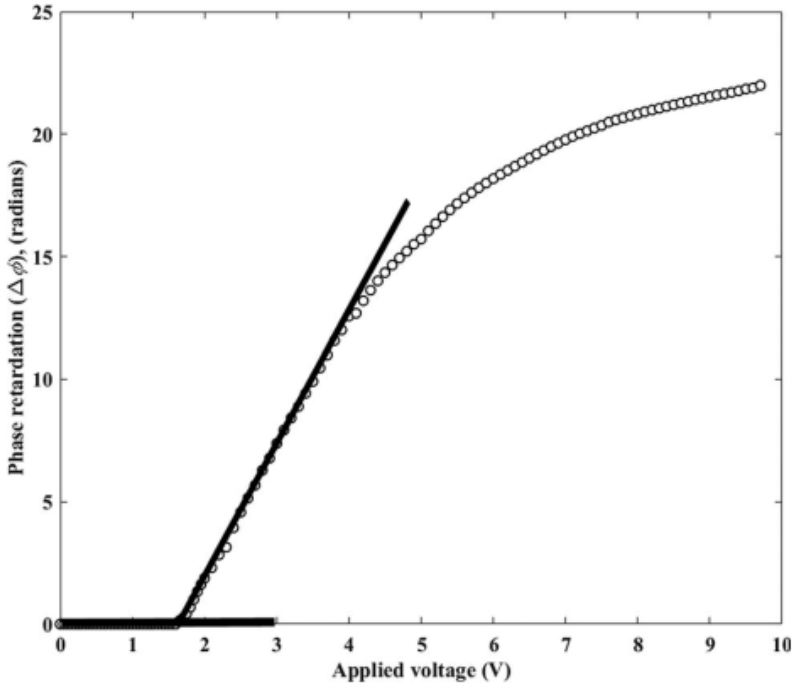

Figure 3-5. Determination of V_{th3} for DTC5C9 material in a homeotropic cell with $d = 19.4\mu\text{m}$ at $T - T_{\text{NI}} = -24^{\text{o}}\text{C}$. The bold straight lines illustrate how the threshold is determined by double extrapolation.

The bend Frederiks transition in a homeotropic cell can also be triggered by the magnetic field directed perpendicularly to the director, as $\Delta\chi$ of MCT5 and DTC5C9 is positive, $\Delta\chi = \chi_{\parallel} - \chi_{\perp} > 0$. The magnetic threshold B_{th3} was determined by measuring the transmitted light intensity passing through the homeotropic LC cell. Using the expression (*58*)

$$K_{33} = \left(\frac{dB_{th3}}{\pi}\right)^2 \frac{\Delta\chi}{\mu_{\text{o}}} \qquad (3\text{-}4)$$

and comparing the bend constant to the value obtained in the electric Frederiks effect, we determined the diamagnetic anisotropy, $\Delta\chi = \varepsilon_o \mu_o \Delta\varepsilon \left(\frac{V_{th3}}{dB_{th3}} \right)^2$. For example, $\Delta\chi = (1.1 \pm 0.1) \times 10^{-6}$ at $T - T_{NI}$ = -22 °C for MCT5, and $\Delta\chi = (1.4 \pm 0.1) \times 10^{-6}$ at $T - T_{NI}$ = -25 °C for DTC5C9. The measured values of $\Delta\chi$ are used in measuring the splay and twist elastic constants in planar cells.

We used two cells of different thicknesses (19.4 μm and 37.6 μm) with the same homeotropic alignment layer and found the same value of $B_{\text{th}} d$ for both cells. The latter justifies that the polar anchoring of the homeotropic alignment is strong enough and that the threshold field and the K_{33} data are not affected by the finite surface anchoring. The threshold field values in other geometries were determined in a similar fashion.

3.3 Results

3.3.1 Dielectric anisotropy

Both MCT5 and DTC5C9 liquid crystals show a negative dielectric anisotropy, Figure 3-6. MCT5 exhibits a monotonous temperature behavior that agrees with data collected by Urban et al for the same compound (referred to as KS3) (*120*). Behavior of DTC5C9 is dramatically different near the N- N_{TB} transition: the absolute value of the dielectric anisotropy starts to decrease in the pretransitional region, similarly to the data by Borshch et al obtained for the 7:3 mixture of DTC5C9 and MCT5 (*2*) .

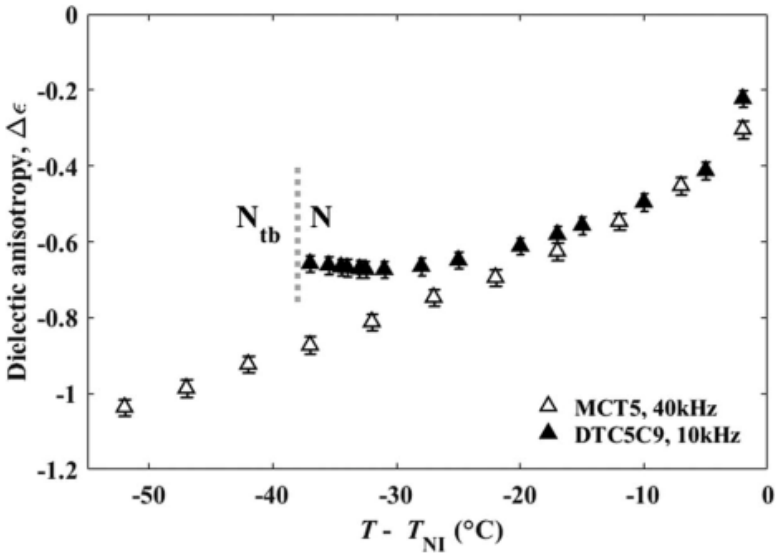

Figure 3-6. Temperature dependence of the dielectric anisotropy for liquid crystal monomer MCT5 (open symbols) and dimer DTC5C9 (filled symbols) measured at frequencies of 40 and 10 kHz respectively. The dashed vertical line represents N- N_{TB} transition temperature for DTC5C9.

3.3.2 Birefringence

Birefringence of MCT5 increases monotonically as the temperature is reduced, in a fashion typical for rod like molecules (*121*), following the Haller's rule (*66*) in the entire nematic range, Figure 3-7a. Haller's rule is of the form

$$\Delta n = \delta n \left(1 - \frac{T}{T^*}\right)^{\beta}, \qquad (3\text{-}4)$$

where δn, T^*, and β are the fitting parameters. For MCT5 we find $\delta n = 0.309 \pm 0.003$, $T^* = 390.3 \pm 0.2$ K and $\beta = 0.178 \pm 0.004$. As suggested by Geppi

et al (*122*), validity of the fit in Equation 3-4 allows one to approximate the temperature dependence of the order parameter as $S(T) = \frac{\Delta n(T)}{\delta n}$. Using this approximation, we find the value of S increasing from 0.4 to 0.7 within the entire N phase, Figure 3-8, in agreement with the data presented by Geppi et al (*122*) for the compounds very similar to MCT5, such as KS7, in which one of the aliphatic tails is shorter than that of the aliphatic tails of MCT5 by one methyl group.

In contrast to the monotonous behavior of Δn in MCT5, the birefringence of DTC5C9 cooled down from the isotropic phase first increases and then decreases on approaching T_{NTB}, Figure 3-7b. The decrease of Δn near the N_{TB} phase is consistent with other studies of dimers (*2, 18, 74*). The behavior of Δn does not obey Haller's rule, clearly deviating near the N-N_{TB} transition. The temperature range of this deviation is broad, about 10 K. For this reason we use the Haller fit only for the data above T = T_{NTB} + 10 K. The result is shown in Figure 3-7b, yielding $\delta n = 0.219 \pm 0.006$, $T^* = 434.6 \pm 0.4$ K and $\beta = 0.140 \pm 0.009$. Non-monotonous $\Delta n(T)$ behavior suggests that the order parameter $S(T)$ might also be non-monotonous. As a rough approximation, we assume that the two functions are connected in a linear fashion, $S(T) = \frac{\Delta n(T)}{\delta n}$, where $\delta n = 0.219$ is the value obtained from the fit above. More accurate measurement of $S(T)$ would require independent measurements of ordinary and extraordinary refractive indices. The dependence $S(T)$ calculated from the entire range of data on $\Delta n(T)$, is non-monotonous, with a maximum $S_{\max} = 0.68$ achieved at about 10

K above T_{NTB}, Figure 3-7b. Interestingly, the non-monotonous $S(T)$ with the maximum at T_{NTB} +10 K has been already reported by Emsley et al (*123*) who measured the order parameter from chemical shift anisotropies in NMR experiments and prior to that by Adlem et al (*15*) in their NMR studies of quadrupolar splitting of a dimeric mixture. A similar conclusion about pretransitional changes of $S(T)$ that start at T_{NTB} +10 K were made by Burnell et al (*124*) for the mixture of flexible dimer CB9CB with 5CB.

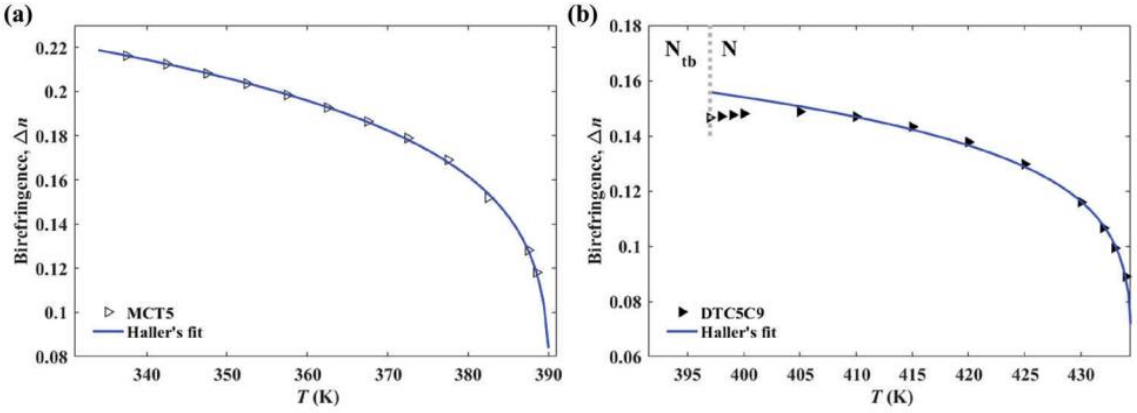

Figure 3-7. Temperature dependence of Δn for (a) monomer MCT5 (open symbols) and (b) dimer DTC5C9 (filled symbols). The wavelength of the probing light was 546 nm.

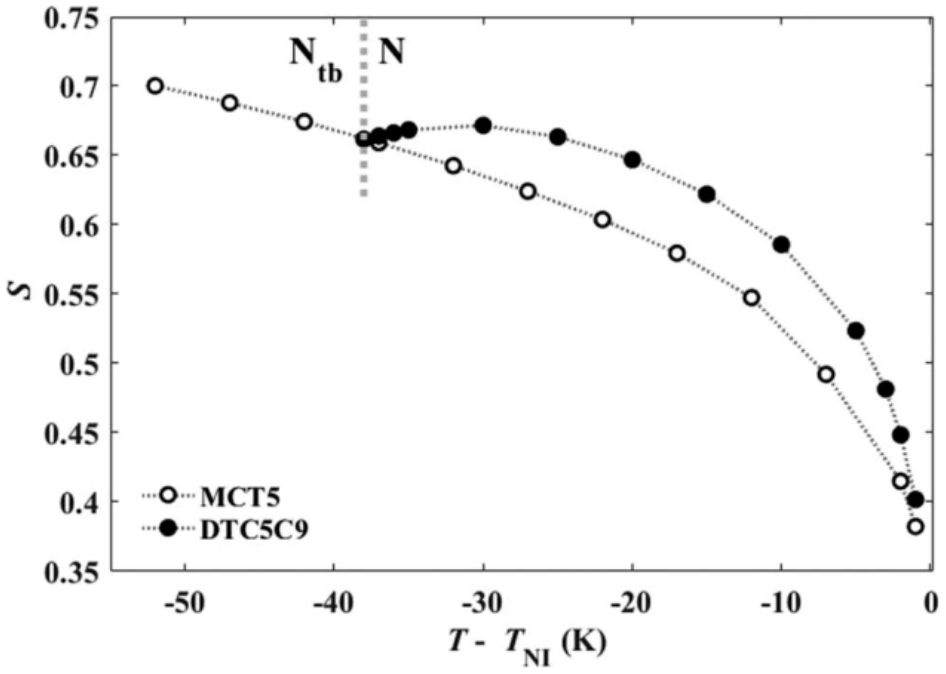

Figure 3-8. Temperature dependence of S for the monomer MCT5 (open symbols) and dimer DTC5C9 (filled symbols). Dotted lines connecting the data points are guides for eyes.

3.3.3 Elastic constants

The elastic constants of MCT5 (Figure 3-9) follow general behavior of calamitic LCs, as $K_{33} > K_{11} > K_{22}$ (*91, 125*). The temperature behavior of the elastic constants of DTC5C9 is dramatically different in comparison to MCT5. The ratio $K_{11} / K_{22} > 2$ (Figure 3-10a), as expected by Dozov for materials exhibiting the N_{TB} phase (*10*). On departure from T_{NI}, K_{33} first increases and then dramatically decreases on approaching T_{Ntb} (Figure 3-11).

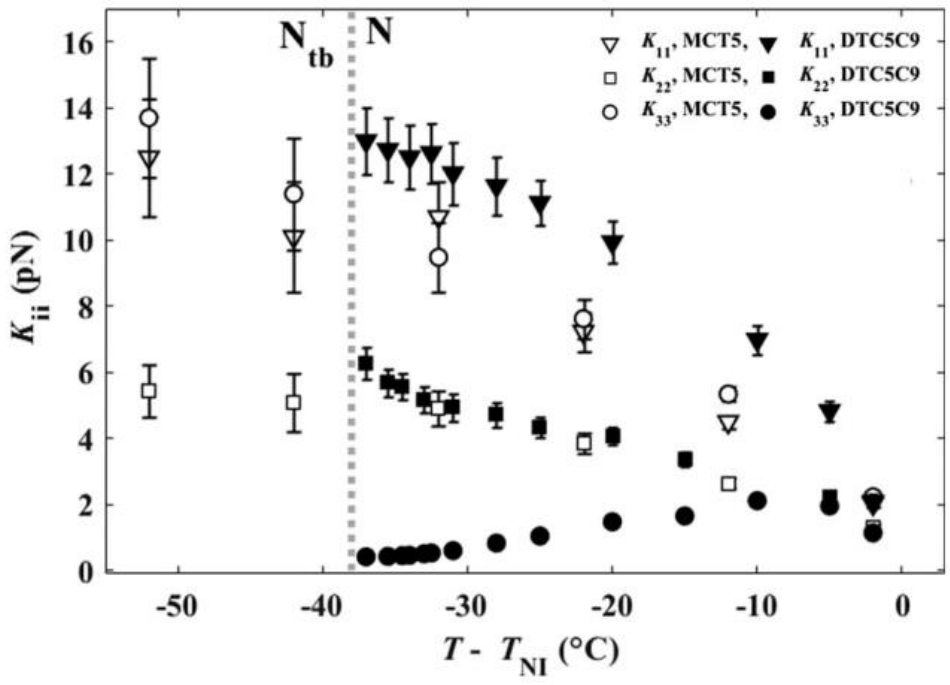

Figure 3-9. Temperature dependent elastic constants of MCT5 (open symbols) and dimer DTC5C9 (filled symbols).

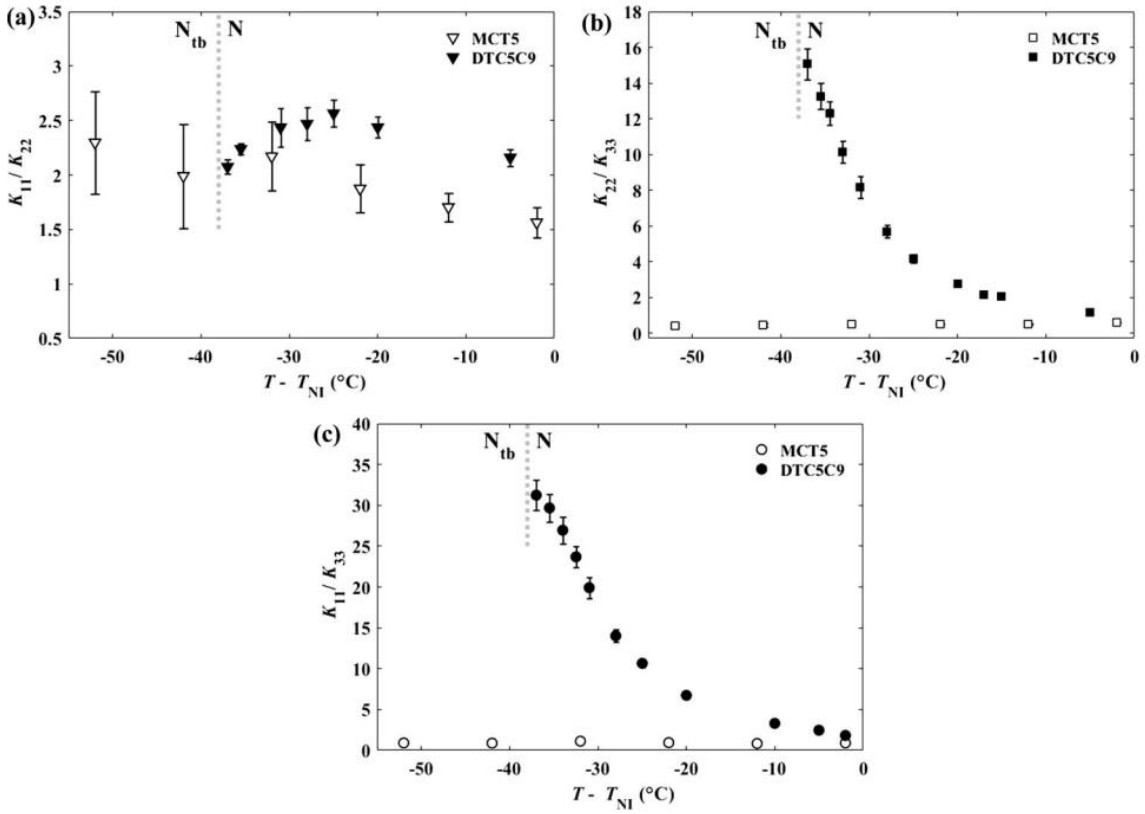

Figure 3-10. Temperature dependencies of the ratios (a) K_{11} / K_{22} (b) K_{22} / K_{33} and (c) K_{11} / K_{33} for MCT5 (open symbols) and DTC5C9 (filled symbols).

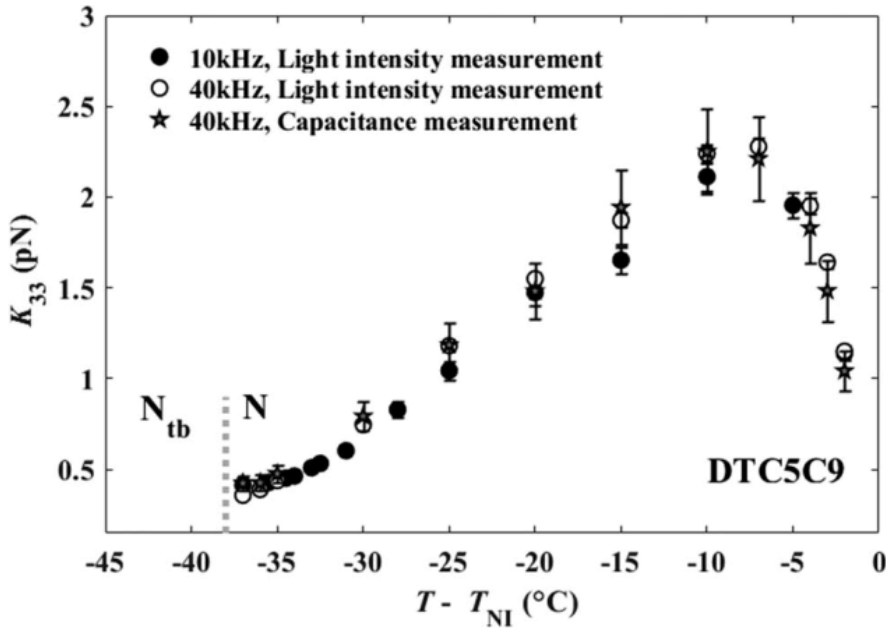

Figure 3-11. Temperature dependence of K_{33} for DTC5C9. Filled and empty circles represent the results obtained by the light intensity measurements with applied electric fields at 10 and 40 kHz respectively. The stars represent K_{33} extrapolated from the capacitance vs voltage curve.

3.4 Discussion

In conventional rod-like nematic liquid crystals (such as MCT5), far from the phase transitions into lower-symmetry phases, the anisotropic properties such as birefringence and dielectric anisotropy change linearly with the scalar order parameter. The birefringence obeys the Haller type behavior, Figure 3-7, implying that the scalar order parameter of MCT5 monotonously increases as the temperature is lowered from T_{NI}. In the simplest mean-field models, the elastic constants are expected to follow the relationship $K_{ii} \propto S^2$, while showing the inequalities $K_{33} > K_{11} > K_{22}$ (*23*, *91*). The

temperature behavior of the elastic constants for MCT5 follows these expectations rather well. Indeed, Figure 3-9 demonstrates that $K_{33} > K_{11} > K_{22}$. The ratio of any two elastic constants is roughly independent of temperature, as shown for MCT5 by open symbols in Figure 3-10.

DTC5C9 shows a dramatically different behavior. First of all, Δn exhibits a non-monotonous temperature dependence, decreasing near N- N_{TB} transition, within a rather broad temperature range. The maximum Δn is achieved at the temperature ~10 K above T_{Ntb}, suggesting that S follows a similar non-monotonous behavior with a maximum at a similar temperature. NMR measurements by Emsley et al (*123*) for DCT5C9 show that $S(T)$ is indeed reaching a maximum at 10 K above T_{Ntb}. The non-monotonous temperature dependencies of Δn and S could be associated with the growth of the population of molecular conformers with a bent shape at lower temperatures and higher densities. It is very likely that these bent molecules form pretransitional clusters with the structure closely resembling the structure of the N_{TB} phase. We remind here that according to the theory, the driving force of the N_{TB} phase formation is the tendency of molecules to bent; this bend is uniform in 3D space only when accompanied by twist (*10, 12*). The twist-bend distortions set up a one-dimensional periodic modulation of the local director. In the pretransitional region, one would expect a similar interplay of spontaneous bend and twist so that the pretransitional clusters could develop some pseudo-layered structure.

We turn now to the discussion of the elastic properties of DTC5C9. The splay elastic constant is noticeably larger than that in MCT5, Figure 3-9. For example, at the

temperature $T - T_{NI} = -10\ ^{o}\mathrm{C}$, MTC5 and DTC5C9 show K_{11} = 4 and 7 pN, respectively, while at $T - T_{NI} = -20\ ^{o}\mathrm{C}$, the values are K_{11} = 7 and 10 pN. This result correlates with the model proposed by Meyer, in which K_{11} is expected to increase linearly with the length L of the molecules (*126*), $K_{11} = \frac{k_B T}{4d}\frac{L}{d}$, where k_B is the Boltzmann constant, T is the absolute temperature, d is the diameter of the rod-like molecule. Splay deformations require creation of gaps between the molecules. To keep the density constant, these gaps must be filled with the ends of adjacent molecules. The formula above follows from the consideration of the entropy loss associated with rearrangements of the molecular ends assumed to behave as non-interacting particles of an ideal gas (*126*). Such an assumption is well justified for long molecules, but might be less accurate for relatively short ones. It is worth noticing that other monomer-dimer comparative studies do not show such a large differences in the values of K_{11} (*127*) and sometimes even show that K_{11} of dimers is smaller than K_{11} of a monomer. Dilisi et al (*128*) measured K_{11} for a monomer 4,4'-dialkoxyphenylbenzoate [$C_5H_{11}OC_6H_4COOC_6H_4OC_5H_{11}$], its related "even" dimer with a spacer of ten methylene groups (*127*) and an "odd" dimer with nine methylene groups in the flexible bridge (*128*). It turned out that the odd dimer, presumably of a bent shape similar to that one of DTC5C9, produced the lowest K_{11} among the three studied molecules (*127, 128*), contrary to our case. For example, at $T - T_{NI} = -10\ ^{o}\mathrm{C}$, the values of K_{11} for the monomer, even dimer, and odd dimer, are 7.5, 8.5, and 5 pN, respectively (*127, 128*).

One might argue that a reduced scalar order parameter of the odd dimer (which is indeed evidenced by the lower diamagnetic anisotropy (*128*)) might lead to a smaller K_{11}. However, this mechanism is apparently not the main one governing K_{11} in DTC5C9 and MCT5, and the increase of the molecular length appears to be dominating.

The twist elastic constants of DTC5C9 and MCT5 show similar values in the upper temperature range but behave differently at lower temperatures. Namely, K_{22} of DTC5C9 increases noticeably near the transition into the N_{TB} phase. An increase of K_{22} is typical near the nematic – smectic A phase transition phase and is explained by the formation of cybotactic clusters with periodic structure of equidistant layers that hinder deformations of twist and bend of the normal to the layers. A similar mechanism should be expected in the vicinity of T_{Ntb}, even if the smectic order, in the sense of periodic mass density modulation, does not develop. The N_{TB} structure is one-dimensionally periodic because of twist-bend director modulation and thus also prohibits deformations of twist and bend of the heliconical axis. The increase of K_{22} can thus be treated as a pretransitional effect potentially caused by the formation of pretransitional clusters with a pseudo-layered structure. Such an effect correlates well with the pretransitional decrease of birefringence and scalar order parameter in DCT5C9 discussed above. The measured values of K_{11} and K_{22} show that $K_{11}/K_{22} > 2$; the result agrees with the Dozov model of the N_{TB} phase (*10*).

The most spectacular deviation of DTC5C9 from the classic picture of nematic elasticity is demonstrated by K_{33}, Figure 3-11. As the temperature decreases from T_{NI},

K_{33} first increases, but after reaching a maximum, K_{33} decreases to a very low value of 0.4 pN. The rate of the decrease is slowed down near the N- N_{TB} transition; there seems to be a small plateau or even an increase right before the transition. Such a behavior has been already observed in other studies and is associated with the bent conformations of the dimeric molecules (*15*, *18*). Importantly, the temperature dependence of K_{33} in DTC5C9 does not correlate with the expected behavior of the scalar order parameter, as clearly evidenced by a strong temperature dependencies of the ratios K_{22}/K_{33} and K_{11}/K_{33}, Figure 3-10b,c.

The idea that bent shape of molecules can lead to a small bend constant K_{33} dates back at least four decades to the theoretical works by Gruler (*95*) and Helfrich (*96*). The underlying mechanism is that in presence of bend deformations, the distribution of molecular orientations is no longer axially symmetric; the molecules can realign cooperatively, mimicking the director bend by adjusting their bend shapes and thus relieving the elastic strain. Reduction of K_{33} through bent conformations has also been predicted by Terentjev and Petshchek (*129*) and by Osipov and Pajak (*130*). Experimentally, a reduction in K_{33} was indeed confirmed for mixtures (*131*) and pure compounds with rigid bent core molecules (*68, 87, 94*).

The considerations by Gruler and Helfrich have been recently reinforced in the density functional theory by De Gregorio et al (*132*). Namely, mesogens of bent shape are shown to exhibit a non-monotonous dependence of K_{33} on the number density of the molecules. As a function of an increasing S, K_{33} is predicted (*132*) to first increase

(near T_{NI}), then reach a maximum and decrease to 0, presumably when the material undergoes a transition into the N_{TB} phase. Importantly, the effect of a reduced K_{33} is observed only if the bent-core molecules are collectively adjusting to the imposed bend. If the orientational distribution of the bent region remains locally uniaxial, the model (*132*) predicts a strong increase of K_{33} with the enhancement of S, a classic result for the rod-like mesogens.

It is important to stress that the experimental values of K_{33}, unlike some of their theoretical counterparts, never reach zero at T_{NTB} and might even slightly increase near the transition (*15*). The most likely reason is formation of pretransitional clusters with local bend and twists which establish a pseudo-layered structure, similarly to the discussed case of an increased K_{22}.

Finally, $K_{33} < K_{22}$ found for DTC5C9 opens a possibility for realization of the Ch_{OH} cholesteric under an applied electric field as predicted by Meyer (*133*) making the cholesteric pitch and thereby the selective reflection band tuneable (*24, 25*).

3.5 Conclusion

We determined the material parameters of the uniaxial nematic phase formed by a monomer MCT5 and the flexible odd dimer DTC5C9. The monomer shows a classic temperature dependence of the material properties expected for rigid rod-like mesogens. The dimer DTC5C9 exhibits a dramatic departure from this behavior. First, the birefringence of DTC5C9 does not follow the Haller's rule in a broad temperature range of width ~10 K near T_{NTB}. This behavior correlates well with the idea that the scalar order

parameter in the pretransitional region decreases, because of the growth of population of molecules with bent conformations and formation of pretransitional clusters with local bends and twists. The twist elastic constant increases near the N-N_{TB} transition, while the bend constant decreases to about 0.4 pN. The ratios of the elastic constants such as K_{11} / K_{33} and K_{22} / K_{33} show a strong temperature dependence, emphasizing that K_{33} does not correlate with the scalar order parameter. It is very likely that the bend deformations used to directly determine K_{33} in the bend Frederiks transition are relieved by formation of polar biaxial structures with the bent molecules packed in a similar fashion, thus modifying the orientational distribution function. Finite values of K_{33} and an increase of K_{22} near the transition into the N_{TB} phase can be associated with the pretransitional formation of pseudo-layered clusters.

CHAPTER 4

Liquid crystal elastomer coatings with programmed response of surface profile

4.1 Introduction

A liquid crystal elastomer (LCE) is an anisotropic rubber, as it is formed by cross-linked polymeric chains with rigid rod-like mesogenic segments in the main chain and attached as side branches; these mesogenic units are similar to the molecules forming low-molecular weight liquid crystals (*30, 134*). The mesogenic moieties in the nematic state of an LCE are oriented along the director. Cross-linked polymeric chains are structurally anisotropic. Upon heating the orientational order weakens and the cross-linked polymer network becomes more isotropic, thus, a uniformly aligned LCE strip contracts along the director and expands in the perpendicular directions (*134*). Such a uniform LCE strip behaves as an artificial muscle (*135*).

Recent research unraveled even more exciting effects when the director changes in space, $\hat{\mathbf{n}}(\mathbf{r}) \neq \text{const}$. Thin LCE films with in-plane director patterns develop 3D shape changes with non-trivial mean and Gaussian curvatures when exposed to thermal or light activation (*30, 136-144*), while director deformations across the film trigger wave-like shape changes and locomotion when activated by light illumination (*145*). In a parallel vein, there is a tremendous progress in exploiting LCE coatings in which one surface is attached to the substrate and the other is free (*35, 146*). When illuminated with light,

photoresponsive coatings with a misaligned director develop random spike-like topographies (*39*), while periodic elevations and groves can be produced by using cholesteric "fingerprint" textures (*33*), or periodic stripe arrays (*147*). The challenge is in finding an approach by which the change of the topography of the coating or its stretching/contraction can be deterministically pre-programmed.

In this work, we demonstrate such programmed displacements and dynamics of surface profile in an artificial skin, made of an LCE. The program is written as a pattern of molecular orientation in the plane of the LCE coating that is initially flat. When activated by temperature, the coating changes its surface profile as prescribed by the in-plane pattern, by moving the material within and out-of-plane. The displacements are deterministically related to the molecular orientation pattern. For example, circular bend of molecular orientation causes elevations, while radial splay causes depressions of the coating.

4.2 Materials and methods

4.2.1 Photoalignment of substrates

Glass substrates were first cleaned and treated with UV ozone. Subsequently, the photosensitive material, LIA-S, (0.5%) (DIC Corporation) in Dimethylformamide was spin-coated on them and successively baked at 90˚C for 30 min. The cell was assembled using two indium tin oxide coated glass substrates treated with LIA-S, and the spacing was controlled with 5 μm silica spacers (Bangs Laboratories, Inc.) which were pre-mixed with NOA UV71 glue. In order to pre-pattern liquid crystal molecular director onto the

treated glass substrates, we used plasmonic metamask (PMM) (Figure 4-1) made of rectangular nanoaperture arrays (100nm x 220nm) in Al film (*148*). Illuminating PMM with EXFO X-Cite series 120 unpolarized light source creates a pattern of linearly polarized light. The resultant polarized light photoaligns the azobenzene chromophores of the photosensitive layer perpendicularly to the polarization direction of the incident light (Figure 4-2) (*148*). The polymerized films were probed at 546 nm wavelength using PolScope in order to map the director configuration of an LCE in the *xy*-plane using the optical phase retardance measurements. Note that the typical period of the patterned director in our work is ≈ 100-200 μm, which is much smaller than the period of structures of free films studied by Ware et al (*139*). The smallest pixel in Ref. (*139*) is about 100 x 100 μm, while in our approach is it about 4.5 μm x 4.5 μm or better (*148*).

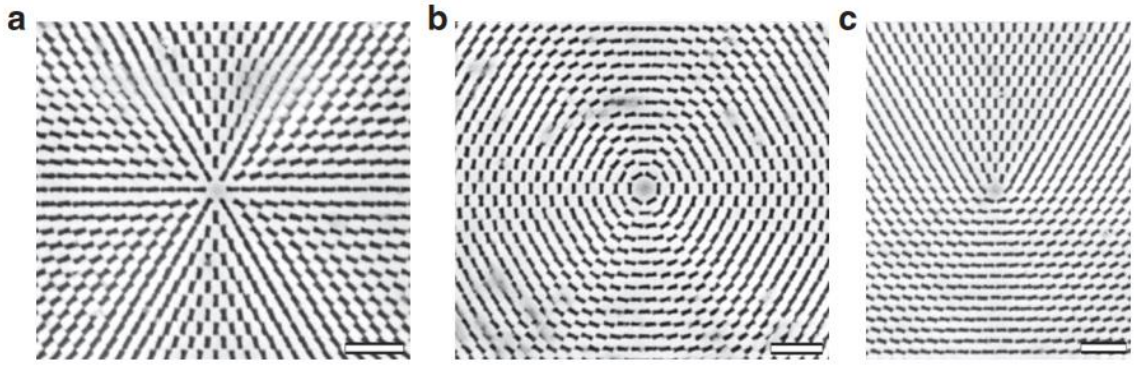

Figure 4-1. Plasmonic metamasks. Scanning electron microscopy images of fragments of metamasks with (a) radial defect, $m = +1$ and $\varphi_0 = 0$. Scale bar, 1 μm. b, circular defect, $m = +1$ and $\varphi_0 = \pi / 2$. Scale bar, 1 μm. c, $m = +1/2$ defect. Scale bar, 1 μm.

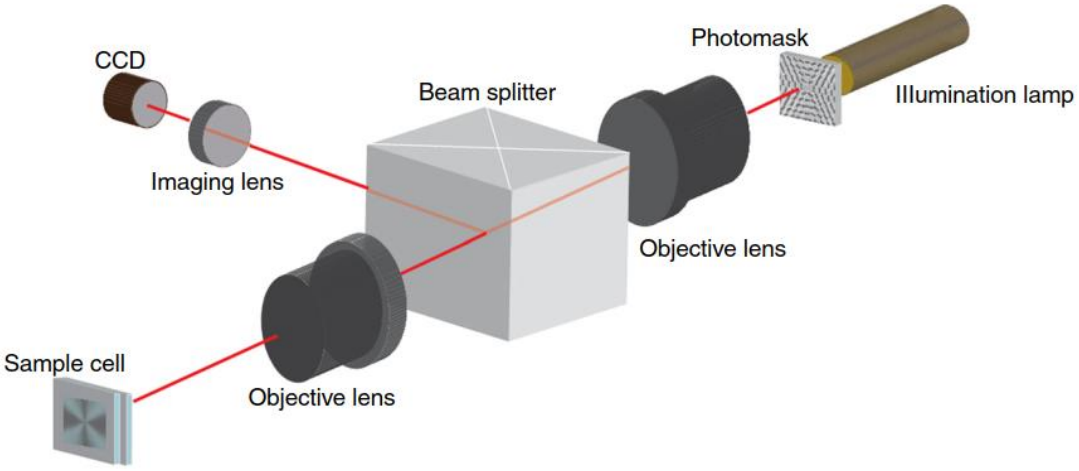

Figure 4-2. Optical set-up for photopatterning. Experimental set-up for photopatterning the director field onto the empty cell consisting of two glass substrates coated with photosensitive layer.

4.2.2 Preparation of the liquid crystalline polymeric coatings

The chemical structures of the reactive monomers RM82 (25wt%), RM23 (25wt%), RM105 (49.2wt%) (Merck) and photoinitiator Irgacure 819 (0.8wt%) is shown in Figure 4-3 The monomers were homogeneously mixed with the photoinitiator in Dichloromethane overnight at 40˚C. The monomeric mixture was injected into the photoaligned cells in an isotropic phase at 80˚C by capillary action. The samples were than cooled down to the nematic phase and kept at 50˚C during the photo-polymerization which was performed using 365 nm LED lamp (Thorlabs M365LP1) for 10 min with intensity of 8.8-18.3 mW/cm^2. The intensity was controlled by LED controller (Thorlabs DC4104) and a collimator (Thorlabs SM2F32-A). After the polymerization, the top and bottom substrates were separated in order to observe the topography of the film attached to a glass substrate.

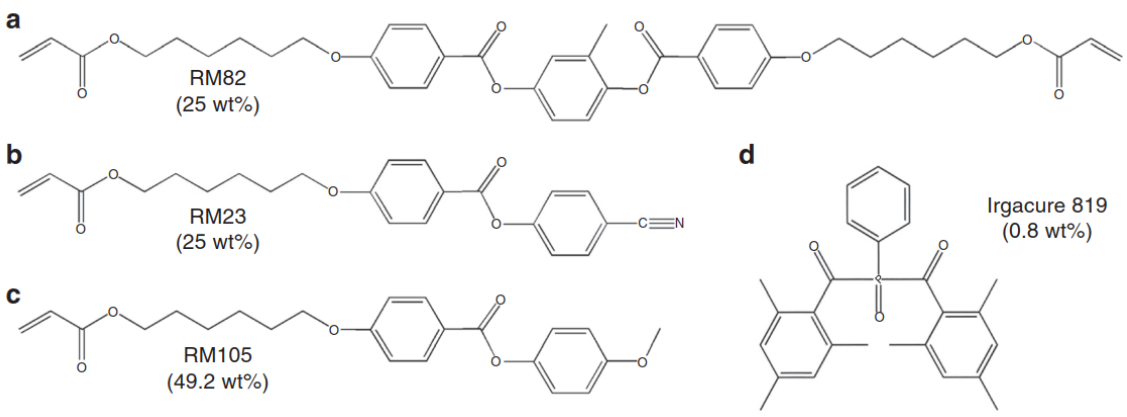

Figure 4-3. Materials. The chemical composition of liquid crystal monomers and photoinitiator used to create the responsive LCEs. a, RM82 (25 wt%). b, RM23 (25 wt%). c, RM105 (49.2 wt%). d, Irgacure 819 (0.8 wt%).

4.2.3 Surface topography measurements

Dynamic optical topography measurements of the partially reflecting surfaces of liquid crystalline polymeric coatings attached to a glass substrate were recorded using Reflection DHM (Lyncée Tec) as a function of temperature. Digital holograms were created using 666 nm monochromatic reference beam which interfered with the object beam received from the polymeric coating. The acquired phase images in real time provided us with the quantitative data for 3D reconstruction of the surface profiles, with the vertical resolution of ≈ 0.3 nm.

4.3 Results

4.3.1 Pre-programming the LCE coatings

The director patterns with pre-designed splay and bend of the director are imposed onto the LCE by the plasmonic photoalignment technique (*148*) (see Sec. 4.2.). Two parallel glass plates separated by a distance of 5 μm coated with photosensitive

azodye molecules are irradiated by a light beam that passes through a plasmonic photomask with a patterned array of elongated nanoapertures. The photomask imparts spatially-varied linear polarization onto the transmitted light beam (*148*). Under irradiation, the azodye molecules reorient their long axes perpendicularly to the local light polarization (*148*). When the liquid crystal in its monomeric state fills the gap between the two glass plates, the patterned surface orientation of the azodye molecules establishes the director pattern in the bulk. The mixture is then photopolymerized to obtain the LCE with the desired pattern of the director. The director is modulated in the (x, y) plane of the film and remains parallel to the bounding plates; there is no change of the director through the thickness of the cell, as the top and bottom plate are photopatterned in the same way. One of the plates is removed to obtain the LCE coating. At this stage, the coating is flat.

Figure 4-4a, Figure 4-5a, Figure 4-6a show the director patterns imprinted into the LCE coatings with arrays of topological defects of integer and semi-integer strength. The director field is of the form

$$\hat{\mathbf{n}} = \left(n_x, n_y, 0\right) = (\cos\alpha, \sin\alpha, 0), \tag{4-1}$$

where $\alpha(x, y) = \sum_i m_i \arctan\left(\frac{y - y_{0i}}{x - x_{0i}}\right) + \varphi_0$, $m_i = \pm 1/2, \pm 1$ indicates the strength of the defect, x_{0i} and y_{0i} are the coordinates of the core of the defect and φ_0 is the constant phase specifying the prevailing type of deformations and orientation of the defect structures. The +1 defects are either of a radial type, carrying splay, when $\varphi_0 = 0$ (Figure

4-4a), or of a circular geometry, carrying bend, when $\varphi_0 = \pi/2$ (Figure 4-5a). The -1 defects in both Figure 4-4a, Figure 4-5a exhibit four alternating regions of splay and bend.

4.3.2 Surface depressions caused by radial defects

The LCE coating with the pre-inscribed director pattern is practically flat at the room temperature. The surface profile is established by Digital Holographic Microscopy (DHM). When the coating is heated above the glass transition temperature (~50 ˚C), its surface topography shows a remarkably robust and reproducible change determined by the specific form of director distortions. Namely, splay regions associated with radial ($m = +1$ and $\varphi_0 = 0$) defects in Figure 4-4a, produce depressions (Figure 4-4b,c,d). The material moves away from the center of the defect along the radial directions.

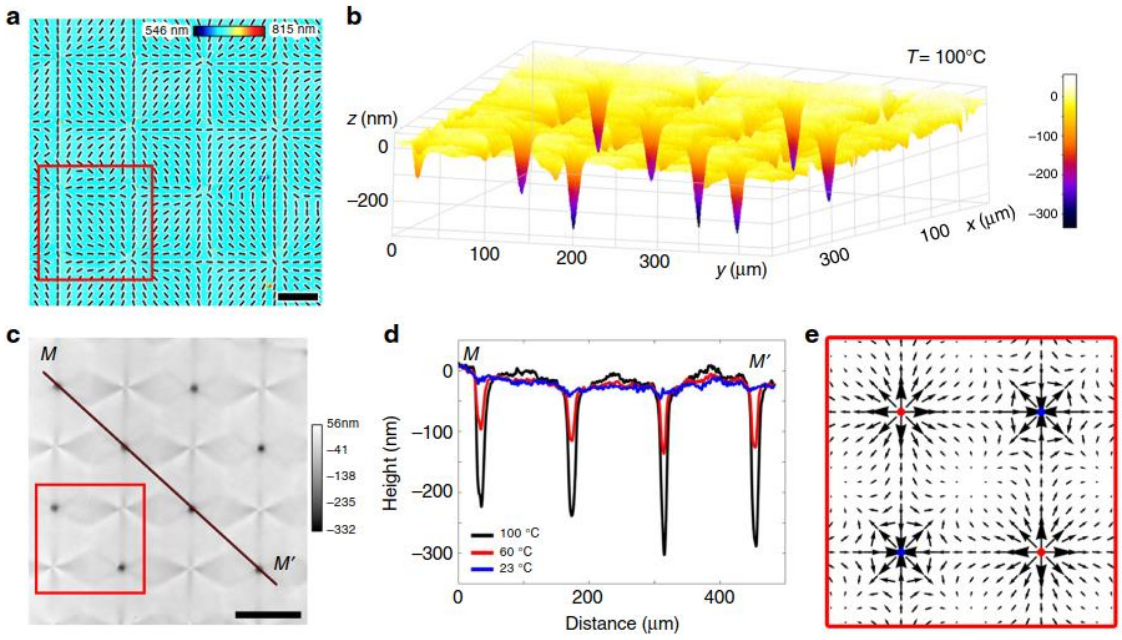

Figure 4-4. Surface depressions developed by radial defects upon heating. a, PolScope image of a flat LCE coating at 23 ˚C which maps the optical retardance and the director

orientation. Scale bar, 50 μm. b, 3D image of surface topography of LCE coating at 100 ˚C with developed depressions at radial defects, as observed using DHM. c, DHM image of the LCE surface at 100 ˚C used to extract the surface topography. Scale bar, 100 μm. d, Surface profiles along line *MM'* in (c) at 23 ˚C, 60 ˚C, 100 ˚C. e, Activation force density **f** map calculated for region outlined by a red box in (a,c).

4.3.3 Surface elevations caused by circular defects

In contrast, bend regions associated with circular ($m = +1$ and $\varphi_0 = \pi / 2$) defects in Figure 4-5a, produce pronounced hills (Figure 4-5b,c,d). The amplitude of thickness variation is about 300-400 nm, representing a substantial fraction of the total thickness ($5\ \mu m$). The typical aspect ratio for depressions in Figure 4-4b,d and elevations in Figure 4-5b,d, determined at 100 ˚C as the depth per height of the deformation divided by its full width at half-depth per height, was about 200 nm per $10\ \mu m$, or 0.02.

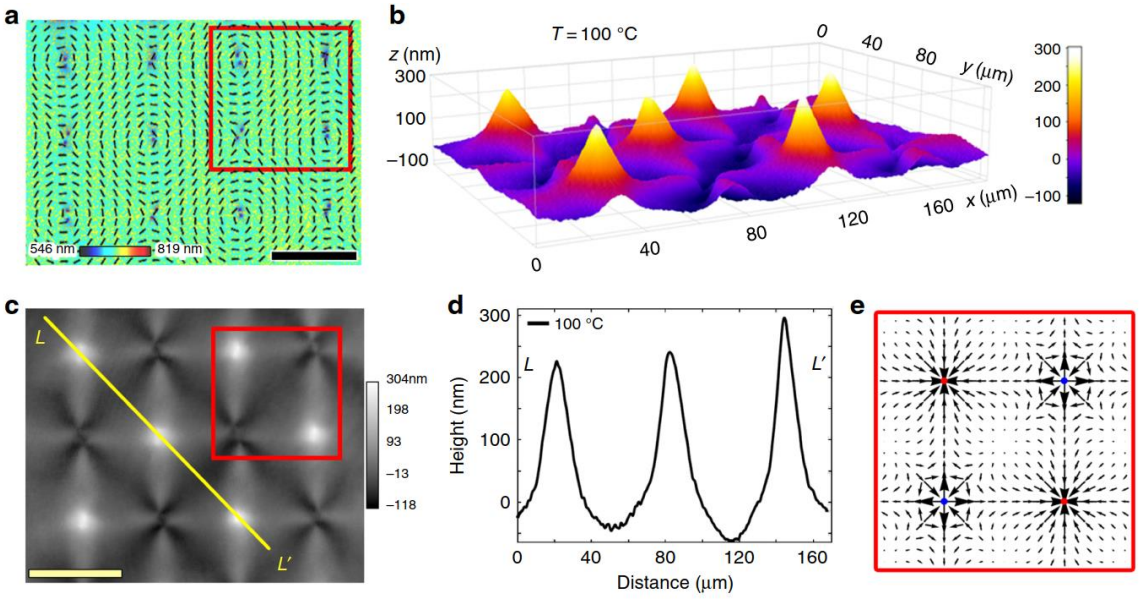

Figure 4-5. Surface elevations developed at circular defects upon heating. a, PolScope image of a flat LCE coating at 30 ˚C which maps the optical retardance and the director orientation. Scale bar, 100 μm. b, 3D image of surface topography of LCE at 100 ˚C with

elevations developed at circular defects, as observed using DHM. c, DHM image of the LCE surface at 100 ˚C used to extract the surface topography. Scale bar, 100 μm. d, Surface profiles along line *LL'* in (c) at 100 ˚C. e, Activation force density **f** map calculated for region outlined by a red box in (a,c).

The heating-induced non-flat profile around $m=-1$ defects is more complicated, exhibiting four ridges and four valleys, which correlates with four regions of splay and four regions of bend (Figure 4-4b,c and Figure 4-5b,c). The dynamics of surface topography is completely reversible when the temperature is cycled between the room temperature and the maximum temperature of around 150 ˚C. The most pronounced profile deformations, such as depressions in Figure 4-4b,d and elevations in Figure 4-5b,d can lose their complete reversibility if the material is heated to temperatures above ~150 ˚C, presumably because of the developed irreversible strains, similarly to the case reported by Ware et al for thermally addressed LCE films with two free surfaces (*139*).

4.3.4 Coupled elevations-depressions caused by ±1/2 defects

Similar relationships between the director patterns and surface topography are observed in patterns with $m=+1/2$ and $m=-1/2$ defects (Figure 4-6). The defects $m=+1/2$ in Figure 4-6 are of a polar symmetry with one bend regions and one splay region; the $m=-1/2$ defects exhibit three regions of bend and three regions of splay each (Figure 4-6a). The corresponding surface profile is comprised of a single elevation/depression pair in $m=+1/2$ case (Figure 4-6b) and three elevations/depressions around the $m=-1/2$ defects, as expected from the symmetry of the defects. There is a new unique feature of the $m=+1/2$ defects, not observed neither for $m=-1/2$ nor for

$m = \pm 1$ defects. Namely, upon heating, both the core and the elevation/depression pair associated with the $m = +1/2$ defect shift along the vector directed from the bend region towards the splay region (Figure 4-6c,e,f). Figure 4-6e,f show the temperature effect on the distance between $m = \pm 1/2$ defect pairs A and B, where the origin (0,0) is their initial separation distance at 30 ˚C. The shift of $m = +1/2$ defect core is fully reversible in the heating-cooling cycles, provided the maximum temperature does not exceed ~150 ˚C.

The displacement of the elevation/depression pair is observed using DHM (Figure 4-6c), by tracing the temperature dependent topography along *TT'* line which crosses three defect cores: -1/2, +1/2 and -1/2 (Figure 4-6b). The inset in Figure 4-6c demonstrates that on heating the LCE by 40 ˚C, the shift Δy of elevation is about $5\,\mu m$. The displacement of the depression is about $3\,\mu m$. The associated shift of the $m = +1/2$ defect core is about $3\,\mu m$ as observed under PolScope (Figure 4-6e,f). The core is the central region of the defect at which the orientational order is strongly diminished. Its position is thus readily visualized by PolScope that maps the local optical retardance since the optical retardance at the core is much lower than in the rest of the sample (Figure 4-6a,e) (*149*).

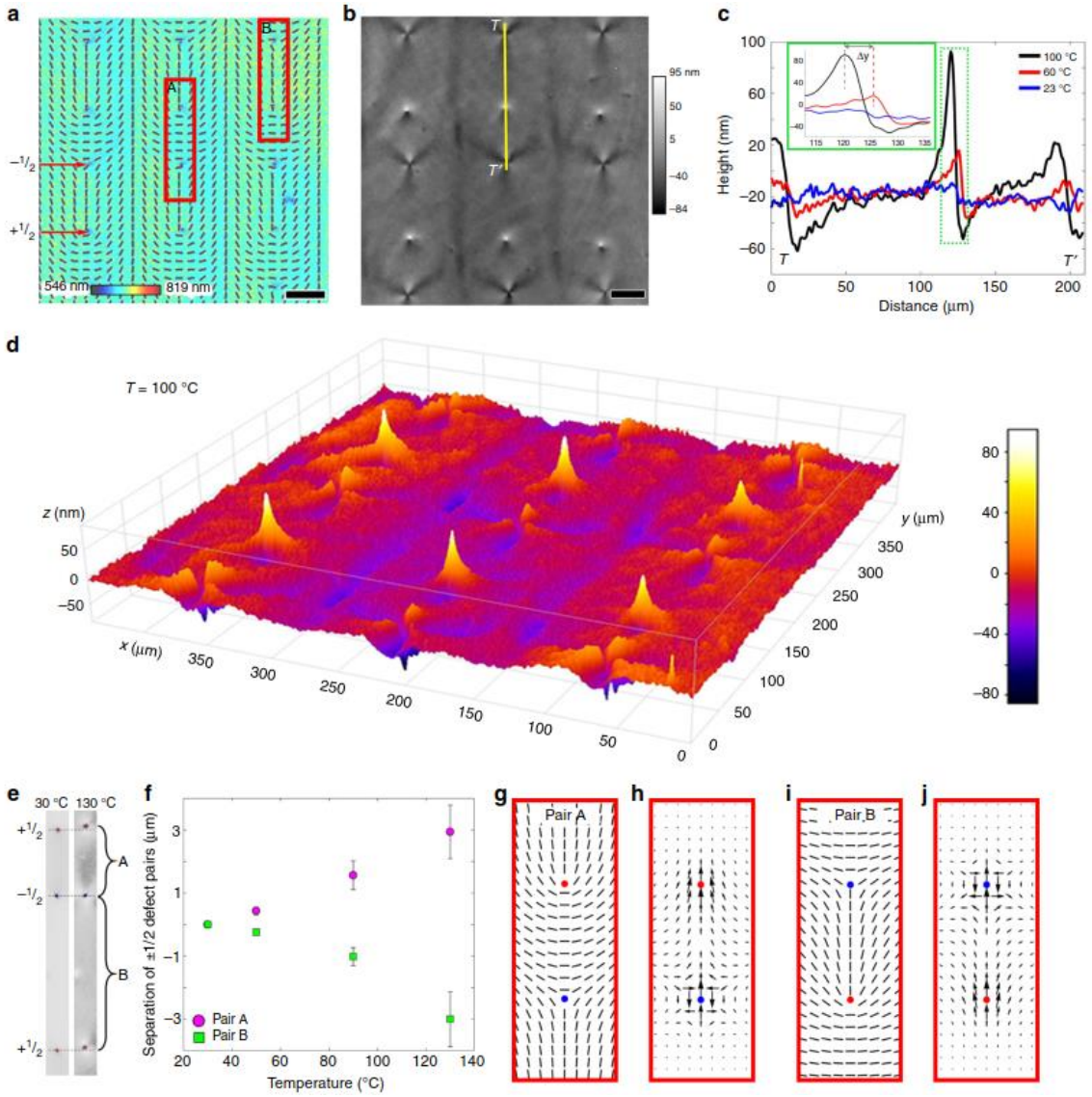

Figure 4-6. Coupled elevations-depressions caused by ±1/2 defects upon heating. a, PolScope image of a flat LCE coating at 23 ˚C which maps the optical retardance and the director orientation; red boxes A and B show two different director configurations of the defect pairs. Scale bar, 50 µm. b, DHM image of the non-flat LCE surface at 100 ˚C used to extract the surface profile along line *TT'*. Scale bar, 50 µm. c, Surface profiles along line *TT'* in (b) at 23 ˚C, 60 ˚C and 100 ˚C. d, 3D image of surface topography of LCE at 100 ˚C observed using DHM. e, Grayscale PolScope images taken at 30 ˚C and 130 ˚C showing the displacement of the half-integer defects as a function of temperature and director configuration that separates the defects. f, Plot showing the distance separating ±1/2 defects as a function of temperature and director configurations A and B. The error bars represent the s.d.'s of 12 measurements. g, Director configuration for pair A. h,

Activation force density **f** map calculated for the director pattern A. i, Director configuration for pair B. j, Activation force density **f** map calculated for director pattern B.

4.3.5 Depressions/elevations caused by splay/bend stripe patterns

The correlations splay $\rightarrow$ depression and bend $\rightarrow$ elevation are observed not only in arrays with topological defects but also in defect-free patterns. As an example, Figure 4-7 shows the response of an LCE coating with the splay-bend stripes, $\hat{\mathbf{n}} = \left(n_x, n_y, n_z\right) = (\left|\cos\beta\right|, \sin\beta, 0)$, where $\beta(y) = \pi y / P$ and P is half the period. The profile along the line *NN'* in the DHM texture (Figure 4-7a) changes from being flat at room temperature to strongly modulated at elevated temperatures, with alternating sharp valleys at the locations of a maximum splay and ridges at locations with a prevailing bend.

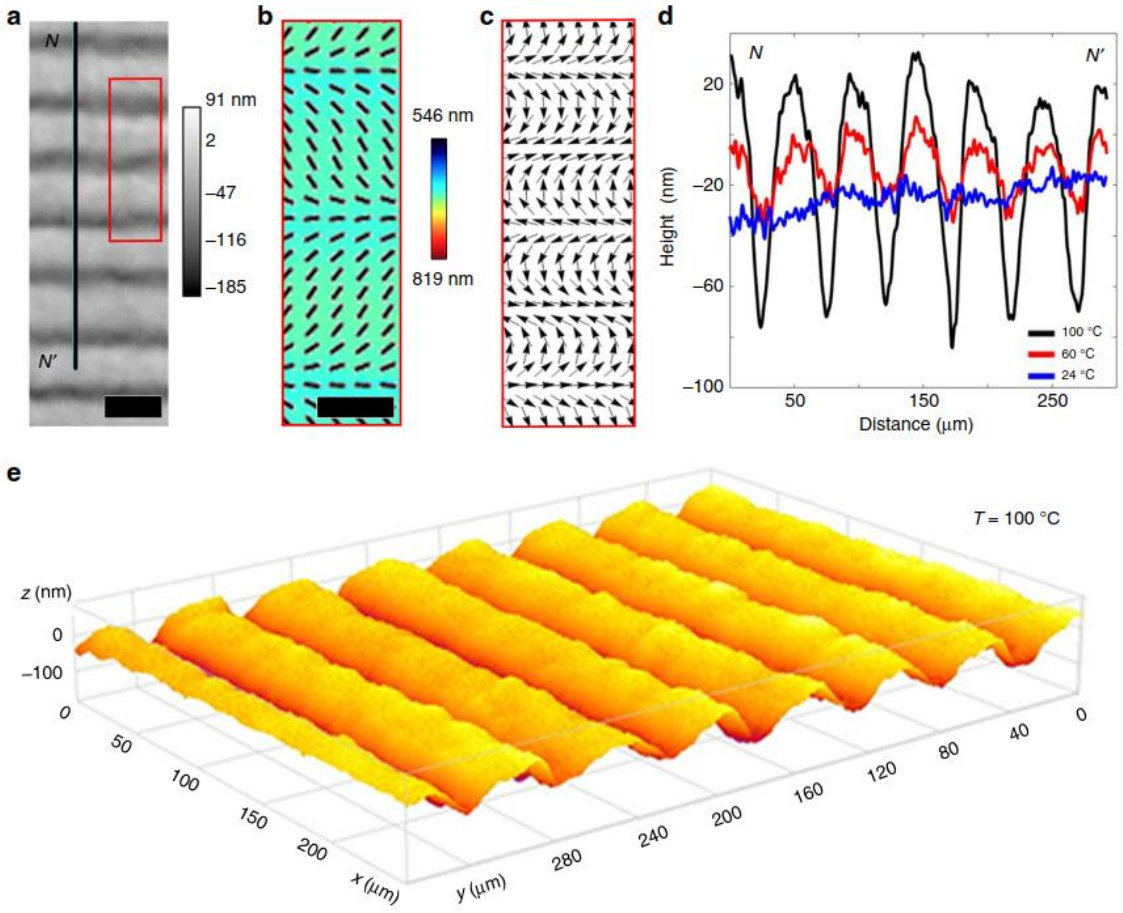

Figure 4-7. Depressions/elevations caused by splay/bend stripes upon heating. a, DHM image at 100 ˚C used to extract the surface profile along line *NN'*. Scale bar, 50 μm. b, PolScope image of a flat LCE coating at 23˚C which maps the optical retardance and the director orientation. Scale bar, 25 μm. c, Activation force density map calculated for region in (a,b) outlined by a red box. d, Surface profiles along line *NN'* in (a) at 24 ˚C, 60 ˚C and 100 ˚C. e, 3D image of surface topography of LCE at 100˚C observed using DHM.

4.4 Discussion

The experiments above demonstrate clearly that the heat-induced dynamic profile of an LCE coating is defined deterministically by the type of director deformations pre-programmed in the plane of the initially flat sample. For example, in Figure 4-4, Figure

4-5, Figure 4-7, splay causes depressions, while bend causes elevations. The relationship is more complicated around $m = +1/2$ defects in Figure 4-6, since the vector connecting a depression to an elevation is directed from bend to splay region (Figure 4-6a,b). The underlying mechanism can be understood by considering the microscopic response of the LCE to a changing temperature.

Orientational order is coupled to mechanical deformations of LCEs, because of the cross-linking of the polymer network. This coupling results in an anisotropic structure of the network characterized by the so-called step length tensor [134] $l_{ij} = l_{\perp}\delta_{ij} + \left(l_{\parallel} - l_{\perp}\right)n_i n_j$. The step length l characterizing the polymer segments connecting cross-linking points is different when measured along $\hat{\mathbf{n}}$ ($l_{\parallel}$) and perpendicularly ($l_{\perp}$) to $\hat{\mathbf{n}}$. For $l_{\parallel} > l_{\perp}$, the spatial distribution of the step lengths can be represented by a prolate ellipsoid elongated along $\hat{\mathbf{n}}$ (Figure 4-8a). If the temperature is raised and the orientational order weakens, the distribution becomes more spherical, i.e., the ellipsoid shrinks along $\hat{\mathbf{n}}$ and expands in two perpendicular directions. Once the nematic order is melted, the ellipsoid becomes a sphere, $l_{\parallel}^{iso} = l_{\perp}^{iso} = \bar{l}$ (Figure 4-8b).

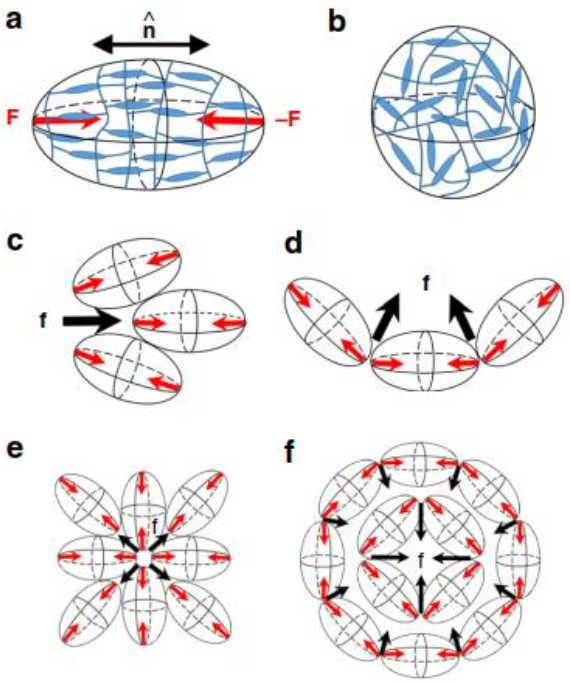

Figure 4-8. Polymer network conformation and occurrence of the activation force. a, Prolate ellipsoid of polymer network conformations in the nematic phase; the long axis is along the director $\hat{\mathbf{n}}$; during heating, the ellipsoid shrinks along the long axis; in the isotropic phase, it becomes a sphere, as shown in part (b); the shrinking ellipsoid is modelled by a pair of forces $\mathbf{F}$. c, Activation force density $\mathbf{f}$ produced by contracting ellipsoids in the geometry of splay. d, Activation force density $\mathbf{f}$ produced by contracting ellipsoids in the geometry of bend. e, Map of activation forces in the pattern of a radial splay that push the material away from the center towards the periphery upon heating. f, Map of activation forces in the pattern of a circular bend that push the material from the periphery towards the center.

Morphing of the step length ellipsoid caused by the temperature can be modelled by a force dipole, with two point forces of equal amplitude F directed from the poles of the ellipsoid towards its center (Figure 4-8a). For an LCE of a constant volume and small anisotropy, $l_\perp - l_\parallel << l_\perp, l_\parallel$, this amplitude can be estimated as $F \sim \mu \bar{l} \left(l_\perp - l_\parallel \right)$, where μ is the shear modulus of the LCE, on the order of $\left(10^4 - 10^5 \right)$ J m^{-3}, Ref. (*150*). Whenever

the director field of the LCE changes in space, so do the local axes of the ellipsoids (Figure 4-8c,d). The spatial gradients of the step-length tensor produce a vector quantity with the components $f_i = \alpha \partial_j \left(n_i n_j \right)$, which can also be written in the equivalent invariant form as

$$\mathbf{f} = \alpha \left(\hat{\mathbf{n}} \mathrm{div} \hat{\mathbf{n}} - \hat{\mathbf{n}} \times \mathrm{curl} \hat{\mathbf{n}} \right), \tag{4-2}$$

where $\alpha \sim F / \bar{l}^2 \sim \mu \left(l_\perp - l_\parallel \right) / \bar{l}$ is introduced as an activation parameter that describes the local elastic response to the changing temperature; for the sake of simplicity, the estimated value of α corresponds to the complete melting of orientational order. Note that α depends on the dimensionless anisotropy $\left(l_\perp - l_\parallel \right) / \bar{l}$ rather than on the absolute values of the step lengths, which stresses a universal character of the elastic response of LCEs with little dependence on the concrete microscopic details (*151*). In the order of magnitude, with $\left(l_\perp - l_\parallel \right) / \bar{l} \sim 0.1$, one expects $|\alpha| \sim \left(10^3 - 10^4 \right)$ J m^{-3}. When the temperature of an LCE with $l_\parallel > l_\perp$ increases and the long axes of the polymer ellipsoids shrink, then $\alpha > 0$; in the case of cooling, $\alpha < 0$.

With α defined as above, the vector $\mathbf{f}$ represents a spatially varying activation force density that controls the elastic response of an LCE with a non-uniform director $\hat{\mathbf{n}}(\mathbf{r}) \neq \mathrm{const}$ to the external factors such as heating. The occurrence of the force $\mathbf{f}$ is illustrated in Figure 4-8c,d,e,f for the cases of pure splay and pure bend. For example, in the case of bend, Figure 4-8d,f, the point forces of the two neighboring shrinking

ellipsoids that are titled with respect to each other, produce a net force density $\mathbf{f}$ along the radius of curvature of the director $\hat{\mathbf{n}}(\mathbf{r})$.

The activation coefficient α and the vector $f_i = \alpha \partial_j (n_i n_j)$ are similar to the activity coefficient and active current introduced by Simha and Ramaswamy (*152*) in the description of flowing active matter with elementary swimming units representing force dipoles of either puller or pusher type; the former are similar to the shrinking LCE ellipsoids (Figure 4-8a). Furthermore, the factor $\hat{\mathbf{n}}\mathrm{div}\hat{\mathbf{n}} - \hat{\mathbf{n}} \times \mathrm{curl}\hat{\mathbf{n}}$ is identical to the gradient expression of the flexoelectric polarization in a spatially-nonuniform liquid crystal in which the molecular structure is of quadrupolar symmetry (*153*). It is also the same as the gradient part of the active force considered by Green, Toner and Vitelli (*154*) for distorted incompressible active nematic fluids. All these similarities bring under one umbrella rather different phenomena, flow of active fluids, flexoelectric polarization of a distorted nematic liquid crystal and stimuli-responsive LCEs. The connection is not surprising as in all cases the symmetry of elementary units (ellipsoids of shrinking-expanding polymer networks in LCEs) is quadrupolar, and the orientation of these units varies in space. Note that the force $\mathbf{f}$ in equation (4-2) is not uniquely associated with the heating/cooling and can be used to describe the effect of other stimuli, such as light irradiation, humidity change, etc.

The spatial distribution of the activation force $\mathbf{f}$ acting in pre-programmed director patterns (Figure 4-4e, Figure 4-5e, Figure 4-6g,h, Figure 4-8e,f) qualitatively explains the deterministic relationships $\mathrm{splay} \rightarrow \mathrm{depression}$ and $\mathrm{bend} \rightarrow \mathrm{elevation}$.

Consider first the $m = +1$ defect with a radial splay (Figure 4-4a, Figure 4-8e). The force $\mathbf{f}$ is directed away from the center upon heating, Figure 4-4e and Figure 4-8e. This force transports the matter within the coating. Since the bottom surface of the coating is affixed to the substrate, the transport results in thinning of the coating. The coating thus should develop a depression, as observed, Figure 4-4b,c,d.

The situation is opposite for the circular bend defect of the same topological charge $m = +1$, Figure 4-5a, Figure 4-8f. Upon heating, the force $\mathbf{f}$ moves the material towards the center, Figure 4-8f, making the coating thicker in this region, Figure 4-5b,c,d. It is instructive to compare this behavior to a response of an LCE film containing a similar circular bend $m = +1$ in-plane pattern, but having both surfaces free to deform. As demonstrated theoretically by Modes, Bhattacharya and Warner (*155*), such a free LCE film responds to raising temperatures by bulging out of plane and forming a hollow cone that has an equal probability of protruding upwards or downwards. The top and bottom free surfaces of the film experience similar conical deformations, as clearly seen in the experiments by Ware et al (*139*). In the LCE coating with a fixed substrate, the free surface protrudes only "upwards" and the conical elevation is filled with the material transported from the periphery of the coating by the activation forces $\mathbf{f}$ in equation (4-2).

In the case of $m = -1$ defects, the force $\mathbf{f}$ produces four ridges and four valleys, by converging in the bend regions and diverging in the splay regions. For example, the activation force density map in Figure 4-4e predicts valleys along the horizontal and vertical directions, and the ridges that are at 45 degrees to the valleys, which is what is

seen in the experiment (Figure 4-4b,c). Similar profiles are formed around $m=-1$ defects in Figure 4-5b,c.

The activation force $\mathbf{f}$ also helps to understand why the cores of $m=+1/2$ upon heating move towards the splay region: the angular distribution of the force around the $m=+1/2$ defect core is not symmetric, breaking the fore-aft symmetry with a nonzero net force directed towards the splay (tail) region. This effect is yet another demonstration of a deep analogy between the responsive LCEs and active matter such as arrays of vibrating rods (*156*), living cell cultures (*157*, *158*), bacterial colonies (*159*) and microtubules powered by kinesin motors [(160)]. In all these systems, $m=+1/2$, unlike their $m=-1/2,\pm 1$ counterparts, show a net propulsion in out-of-equilibrium dynamics, either in the direction of bend or splay, depending on whether the active units are extensile or contractile; these types differ in the sign of the activity coefficient α. The heated LCE corresponds to a contractile case, $\alpha>0$; an extensile version with $\alpha<0$ could be manufactured by polymerizing the nematic LCE at elevated temperatures and then cooling it down. The map of the activation force for $m=+1/2$ suggests that the material is pulled from the bend region towards the splay region (Figure 4-6h,j). An exact analytical description of the resulting profile of the LCE coating is not easy to construct, since the solution should account for mass conservation, dynamic coupling of the director field and rubber elasticity to the material transport, different boundary conditions at the two interfaces, etc.; however, the concept of activation force provides the key insights into the deterministic relationship between the in-plane molecular order and heat-triggered surface profiles.

Note here an interesting similarity in the behavior of LCE coatings and interfacial tissues, or "skins", in living organisms. Very recent research breakthroughs (*157, 161*) demonstrated two key factors controlling cell dynamics in biological tissues such as epithelium, namely, orientational order of cells and presence of topological defects in this orientational order. Activity of individual cells combined with the spatially-varying order leads to compressive-dilative stresses in the tissue that facilitate in-plane and out-of-plane displacements, an effect similar to the observed behavior of LCE coatings.

The described variations of surface profile of LCE coatings are rooted in temperature-induced changes in spatially-varying step-length tensor. At this most general level, the situation is similar to the 3D behavior of LCE thin films with two free surfaces that develop regions of varying Gaussian and mean curvature, as demonstrated theoretically (*144, 155, 162-167*) and experimentally (*137-143, 168*). There are important differences, however. The theoretical modelling of the LCE free films considers the limit of vanishing thickness; thickness variations are not involved in the mechanism of bending, although they are important in shaping the free films in the regions of maximum curvatures, as described by Modes, Bhattacharya and Warner (*155*). The top and bottom surfaces of the free LCE films experience the same deformation, except near the regions where the curvature radii are comparable to the film thickness. Top-down symmetry of the free films produces an uncertainty in the direction of the film's bulging (*144, 155, 162-167*). For example, a free film with a circular bend pattern, $m = +1$, changes its shape upon heating into a hollow cone of a positive Gaussian curvature that can protrude either upwards or downwards with respect to the initial flat plane (*155, 162, 166, 167*). The

LCE coatings are different, since only one of the surfaces is free. Upon heating, the activation forces produce only an upward elevation in a circular bend pattern of $m = +1$ (Figure 4-5b, Figure 4-8f) and never a downward depression, while a radial splay with $m = +1$ yields a depression (Figure 4-4b, Figure 4-8e) and never an elevation. Furthermore, the activation forces around $m = +1/2$ defects result in an in-plane mobility of these defects in LCE coatings, while in the case of LCE free films, such a mobility has not been described.

4.5 Conclusion

We demonstrated that the dynamic surface profile of the LCE coatings activated by temperature can be pre-programmed deterministically by inscribing in-plane patterns of orientational order into the initially flat elastomer at the stage of preparation. Deformations such as splay, bend and their combinations cause different response of the LCE coating, triggering topography changes with local elevations, depressions and in-plane shifts. The mechanism of the effect is explained by introducing an activation force that makes the description of dynamically addressed LCEs similar to that of active matter. The proposed approach implies that the activated LCEs can serve as a well-controlled experimental model of active matter, which is a very welcome addition to this rapidly developing field. From the practical point of view, the ability to control 3D shape changes through 2D inscribed patterns of orientational order could be employed to produce coatings with dynamic hydrophobicity/hydrophilicity, coatings that could move microparticles in space according to the underlying topography of their surface, etc.

CHAPTER 5

Guiding microparticles via light-activated deformations of liquid crystal elastomers

5.1 Introduction

Placing microparticles in predetermined locations is a challenging problem of microtechnology (*169-172*). Many current approaches are based on heterogeneous patterning of substrates (*173*). One of the issues is the strength of binding forces and reversibility of particle placement. In this work, we propose an approach that offers reversible light-controlled predesigned placement of microparticles. The technique is based on photoresponsive liquid crystal elastomer (LCE) coatings with predesigned molecular orientation. Ultraviolet (UV) $(\lambda = 365\ \text{nm})$ photoactivation of the LCE translates in-plane patterns of molecular orientation into variable surface topography (*33, 35-38, 41, 43, 44, 174*). When such a photoactivated LCE elastomer coating with spatially varying profile serves as a substrate in contact with a water dispersion of microparticles, the particles are guided by gravity towards preprogrammed locations with the lowest potential energy. When UV irradiation is terminated, the LCE recovers its flat profile and the positions of particles are randomized. We consider different geometries of LCE patterning and discuss the advantages of reversibility of the proposed technique.

5.2 Materials and methods

5.2.1 Preparation of the liquid crystal cells

Indium tin oxide coated glass substrates were cleaned in an ultrasonic bath and subsequently rinsed with isopropyl alcohol. The glass substrates were than dried in an oven at 90 ˚C and treated with a UV-ozone for 5 minutes to remove organic residual and increase the hydrophilicity of the glass for better spreading of polyimide layer (*175*). The uniform planar alignment layer was achieved by spin coating polyimide layer PI2555 (HD Microsystems) onto a cleaned glass and baked in an oven at 275 ˚C for one hour, after which the substrates were rubbed ten times with a velvet cloth in a unidirectional fashion. The photosensitive alignment layer was achieved via spin coating the solution of the photosensitive azo-dye SD1 (synthesized by I.C.) premixed with a N,N-dimethylfomamide (DMF) solvent at 0.5 wt% concentration onto the glass and baking the substrates at 95 ˚C for 30 min. The SD1 coated glass substrates were used to pre-pattern a non-uniform liquid crystal director field orientation using plasmonic metamask (PMM) composed of 200x100 nm nanoaperture arrays in Al film (*148, 176*). The PMM was exposed to an unpolarized metal halide light source with emission spectrum $\lambda = 300 - 750$ nm (EXFO X-Cite series 120). After passing the PPM, the outgoing beam of light becomes linearly polarized. Once the polarized light is incident onto the SD1 coating, the azo dye molecules reorient their long axis perpendicular to the orientation of the polarized light. Liquid crystal mixture (Figure 5-1) was injected into the assembled sandwich-type cells (Figure 5-2a,b) via capillary action to create disclination free liquid

crystal elastomers (LCEs), while the assembly in Figure 5-2c was used to create LCEs with periodic disclinations. The cell spacing was controlled using Micropearl microspacers with diameter (D) of $\sim 8\ \mu m$ (Sekisui Chemical Co. Ltd.) pre-mixed with NOA71 UV glue.

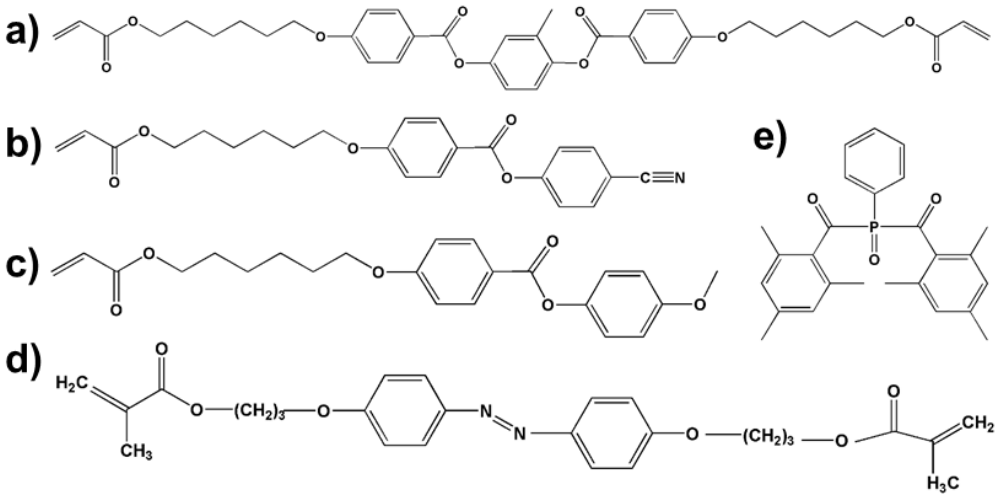

Figure 5-1 Chemical structures of liquid crystal monomers (a) RM82, (b) RM23, (c) RM105, (d) azo-dye, A3MA and (e) photoinitiator Irgacure 819.

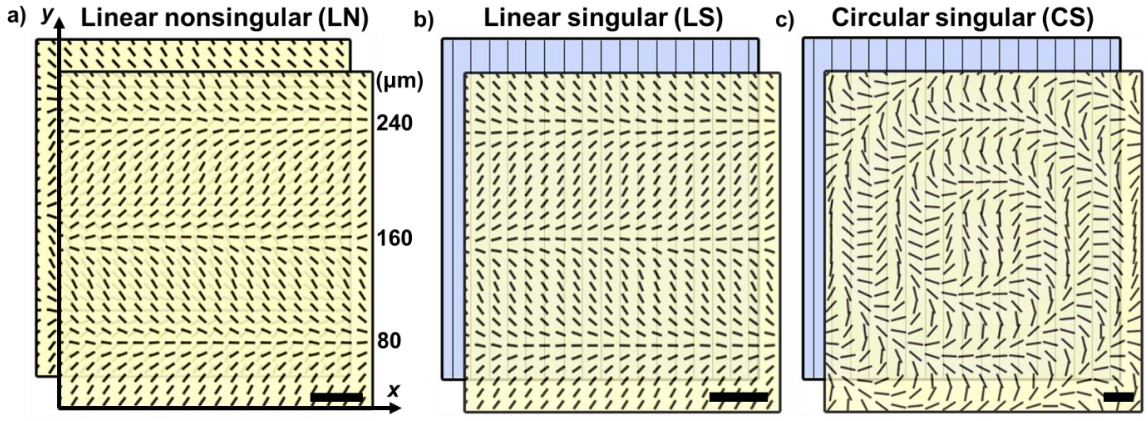

Figure 5-2. Schematic representation of assembled cells consisting of a) an identical linear V-stripes at the top and bottom glass boundaries, b) linear photopatterned "V-stripes" and unidirectional planar substrates, c) circular "C-stripes" and unidirectional planar glass substrates. Scale bar $40\ \mu m$.

5.2.2 Preparation of the light responsive LCE coatings

The composition of the photosensitive mixture presented in Figure 5-1 included monomers RM23 (24.8 wt%), RM105 (46.9 wt%) and RM82 (23.9 wt%) which were homogeneously mixed with a photoinitiator Irgacure 819 (0.9 wt%) (Merck) and azo dye A3MA (3.5 wt%) (Synchom) in Dichloromethane solvent (Sigma Aldrich). The monomeric mixture was injected in the cell in an isotropic phase ($T = 80$ °C) using capillary action, after which the system was brought to 25 ˚C using Linkam PE 94 temperature controller and the LTS 150 hot stage with precision of 0.01 °C (Linkam Scientific Instruments, Ltd.). The aligned monomeric mixture was photopolymerized using metal halide unpolarized light source (EXFO X-Cite series 120) with intensity of 18.3 mW/cm^2 for 10 minutes at $T = 25$ °C. Additionally, a 400 nm high-pass filter was used to avoid exposure to the UV light to prevent premature isomerization of the photoresponsive A3MA molecules (*177*). After curing, one substrate was removed leaving a light responsive LCE coating on the remaining substrate.

5.3 Results and discussion

We use a special class of liquid crystal (LC) molecules with polymerizable acrylate groups (Figure 5-1a-c). When using such reactive LC mesogens, the LC molecular order can be fixed via UV photopolymerization (*29, 31, 32, 178*). The anisotropic LC order is coupled to the physical properties of an LCE (*32, 134, 179*). In particular, in-plane patterns of molecular orientation specified by the so-called director,

$\hat{\mathbf{n}}$, control the local thickness of the LCE coatings activated by temperature (*35, 176*). In this work, we employ photoactivation of LCE coatings.

The LCE coatings were created using reactive mesogens, Figure 5-1a-c mixed with a photoresponsive azobenzene monomer A3MA (Figure 5-1d), and a photoinitiator Irgacure 819, Figure 5-1e. The director patterning of the LCE was achieved by the recently developed technique of PMM photoalignment, as described in Section 2.1.(*148*) The mixture of monomers was confined between two glass plates with a predesigned surface alignment pattern (Figure 5-2). We used three different patterns of the director at the bounding plates. The first is a uniform director aligned along a single direction in the xy-plane of the cell, which we call the *y*-axis, $\hat{\mathbf{n}} = (n_x,\ n_y,\ n_z) = (0,\ 1,\ 0)$. The second represents a one-dimensional periodic system of stripes with V-shaped director field, written as

$$\hat{\mathbf{n}} = (\left|\cos \pi y / p\right|,\ \sin \pi y / p,\ 0), \qquad (5\text{-}1)$$

where p is half the period. The third represents circular stripes with the director resembling a letter "C" and written in cylindrical coordinates as

$$\hat{\mathbf{n}} = (n_r,\ n_\varphi,\ n_z) = (\cos \pi r / p,\ \sin \pi r / p,\ 0), \qquad (5\text{-}2)$$

where r is the distance to the center of the pattern.

After the monomeric mixture was filled in the space between two glass plates, the surface anchoring forces control the bulk director of the monomer mixture. The bulk director structure depends on the type of bounding plates used. If both plates are predesigned as V-stripes in phase with each other, then the bulk director forms a periodic

linear nonsingular (LN) splay-bend structure, Figure 5-2a. When the cell is comprised of one plate treated uniformly and the second plate with V-stripes, then a linear singular (LS) system forms, with linear singular disclinations of strength ½ running along the *x*-axis in the bulk of the sample. The disclinations form along the lines where the director orientations at two plates are perpendicular to each other and separate the right- and left-handed twist domains of the director (*180-182*). In a similar fashion, a combination of circular stripes and a uniform plate shown in Figure 5-2c, produces a system of concentric singular disclinations, which we call a circular singular (CS) pattern.

After the cells were filled with the monomeric mixtures and adopted director fields specified by the boundary conditions, the material was polymerized using a metal halide lamp with $\lambda = 300 - 750$ nm emission spectrum to form a flat ~ 8 μm thick LCE slab. During photopolymerization of the monomers, a high pass filter was placed after the light source, to avoid the premature photoisomerization of A3MA photoresponsive molecules (*177*). At this stage, the LCE elastomer slab is of a uniform thickness, defined by the gap thickness between the two plates. Finally, one of the bounding plates was removed to produce an LCE coating. The bottom surface of LCE coating is affixed to the glass substrate. A water dispersion of microparticles is deposited onto the free top surface of the coating.

The LCE coating remains flat until it is irradiated with UV light at $\lambda = 365$ nm. Irradiation results in the *trans-cis* isomerization of A3MA azo dye, which reduces the scalar order parameter of the LCE and triggers activation forces that lead to expansion/shrinkage of the coating, as described in Ref.(*176*). Previously, we

demonstrated that upon decreasing the orientational order, splay deformation of the director causes the coating to develop valleys, and bend develops protrusions (176). The activation force, $\mathbf{f}$, that links the director field gradients to the topographical changes of the surface profile (*176*),

$$\mathbf{f} = \alpha\left(\hat{\mathbf{n}}\mathrm{div}\hat{\mathbf{n}} - \hat{\mathbf{n}}\times\mathrm{curl}\hat{\mathbf{n}}\right), \qquad (5\text{-}3)$$

where α is an activation parameter, increases as the director gradients become stronger. These activation forces produce non-flat topography of the coating that are determined by the prescribed director pattern (Figure 5-3a, Figure 5-4a, Figure 5-5a). As the experiments reveal, these surface topography changes are sufficiently strong to control placement of microparticles, Figure 5-3, Figure 5-4, Figure 5-5, Figure 5-6.

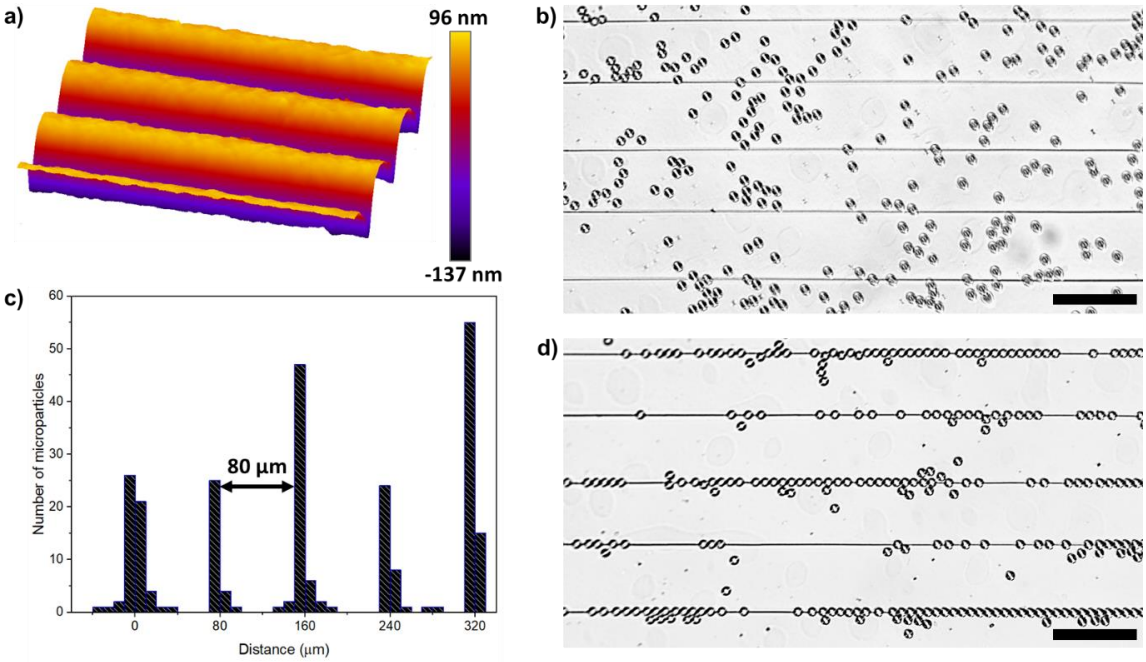

Figure 5-3. LS system. a) 3D visualization of an actuated LCE with LS pattern showing alternating linear hills and valleys, b) light microscopy image showing the random distribution of microparticles at the initial deposition on an LCE surface, c) histogram

showing the 80 μm periodicity of microparticle separation after UV light illumination, d) light microscopy image showing linear chains of assembled microparticles at the disclination sites. Scale bar 100 μm.

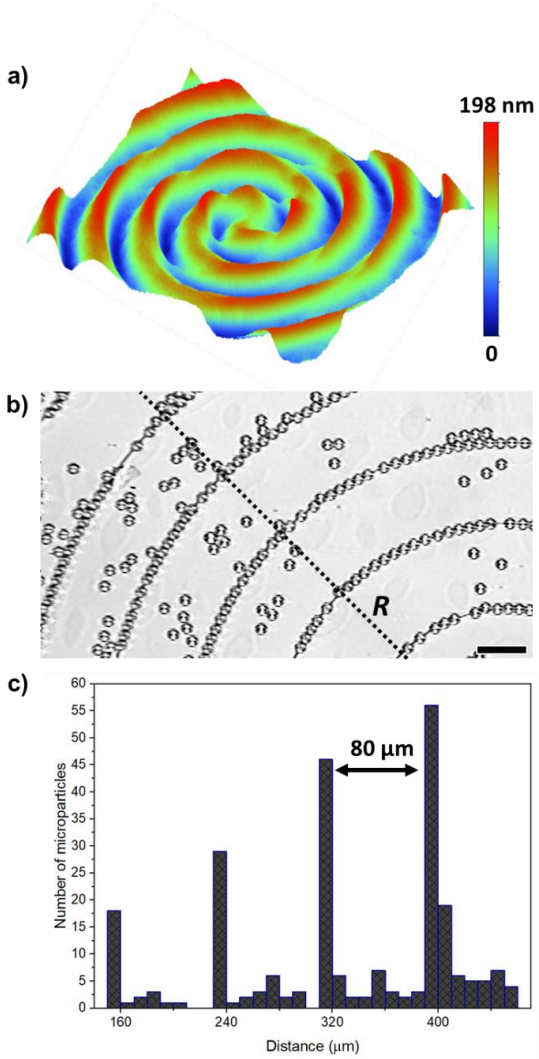

Figure 5-4. CS system. a) 3D visualization of an actuated LCE showing circular surface topography, b) light microscopy image showing the microparticles assembling at the disclination sites after UV irradiation, c) histograms showing periodic 80 μm microparticle separation upon UV light irradiation. The number of particles increases with distance, *R*, since the radius and length of each trough increase with the distance. Scale bar 50 μm.

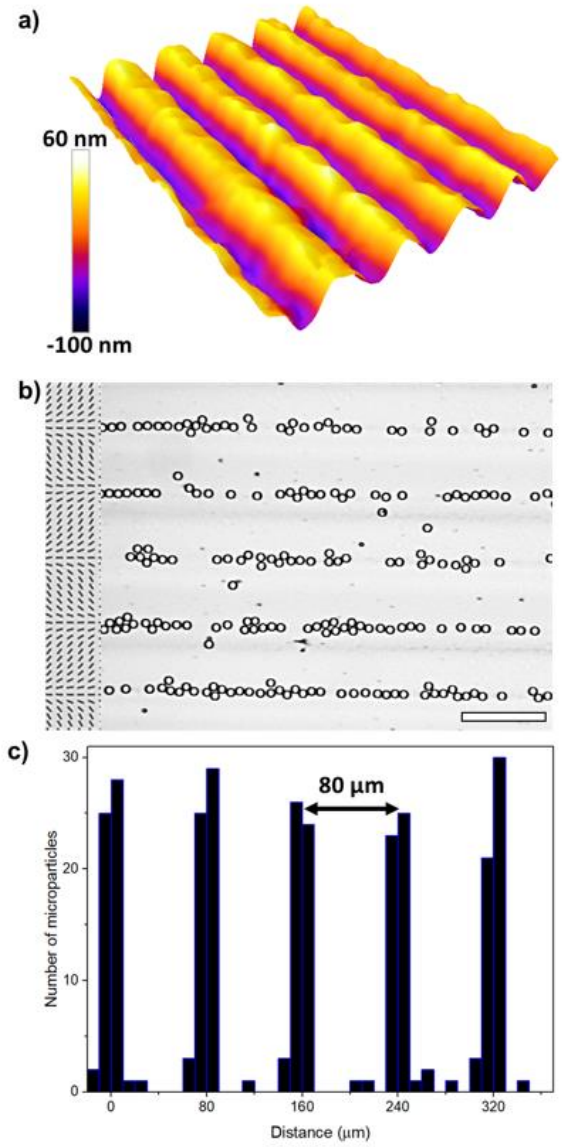

Figure 5-5. NS system. a) 3D visualization of an actuated LCE showing linear, periodic hills and valleys, b) linear V-striped prepatterned LCE showing microparticles forming chain-like assemblies in the splay regions of the LCE coating where valleys are formed upon UV irradiation, c) histogram showing spatial distribution of the microparticles upon UV light irradiation exhibiting the $80\ \mu\mathrm{m}$ periodicity. Scale bar $100\ \mu\mathrm{m}$.

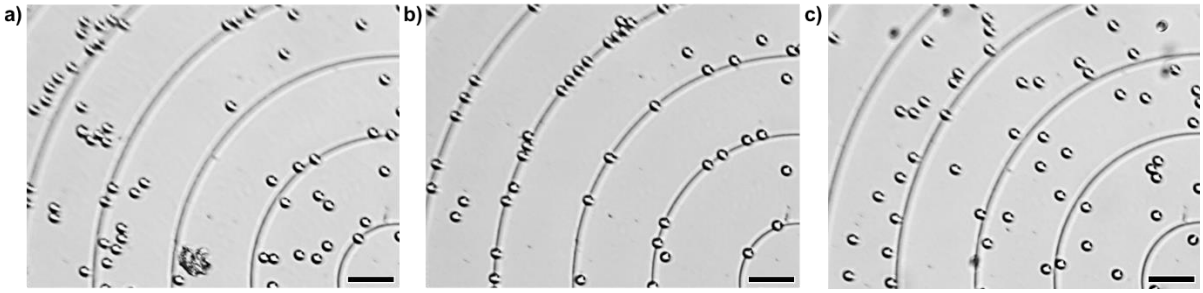

Figure 5-6. CS system. a) Initial deposition of microparticles dispersed in water onto a flat LCE surface showing random distribution, b) microparticles aggregated at the disclination sites where the valleys were formed upon UV illumination for 3 min, c) blue light illumination for 3 min yielded random distribution of microparticles, thus, showing the reversibility of the system. Scale bar $50\ \mu\text{m}$.

Deposition of spherical resin microparticles (Sekisui Chemical Co. Ltd.) of a radius $R = 5\,\mu\text{m}$ onto a flat LCE coating yields a random distribution (Figure 5-3b, Figure 5-6a). Upon UV irradiation at $\lambda = 365$ nm, locations with $y = 80,\ 160,\ 240\ \mu\text{m}$ (Figure 5-2a) at which the director deformations are predominantly of the splay type, develop valleys (Figure 5-3a, Figure 5-4a, Figure 5-5a).(*176*) As a result, after few minutes of UV light exposure, the microparticles move towards the valleys, driven by gravity (Figure 5-3d, Figure 5-4b, Figure 5-5b, Figure 5-6b). The microparticles form chain-like assemblies, spatially separated by 80 μm period, matching the period of the inscribed photopattern (Figure 5-3c,d, Figure 5-4b,c, Figure 5-5b,c, Figure 5-6b). After the preferred arrangement of microparticles was achieved by the UV irradiation at $\lambda = 365$ nm (Figure 5-6b), the UV light was turned off and the sample was irradiated with blue light $(\lambda = 455\ \text{nm})$ instead (Figure 5-6c). The distribution of the microparticles became random within one minute of blue light irradiation (Figure 5-6c). The

assembly/disassembly remains reversible after at least 10 cycles of UV/blue light irradiation.

The disclinations located in splay regions of LS and CS coatings are clearly visible under light microscope (Figure 5-3b,d, Figure 5-4b, Figure 5-6). Upon UV illumination at $\lambda = 365$ nm, these regions develop periodic valleys (Figure 5-3a, Figure 5-4a) that collect microparticles (Figure 5-3d, Figure 5-4b, Figure 5-6b). The histograms in Figure 5-3c and Figure 5-4c show $80\ \mu$m spatial separation of the microparticles matching the periodicity of the photopatterned director field. The disclinations should yield sharper tilts of the LCE coatings, as suggested by Equation 4-3, since the director gradients near disclinations are stronger than in smoothly deformed director. The experiments confirm this expectation: the amplitude of the protrusions in Figure 5-3a is $\sim 20\%$ greater than in Figure 5-5a. Thus, the disclinations provide a deeper potential minimum for the assemblies of microparticles.

Microparticle assembly at the troughs is guided by gravity. In our system, the component of the gravitational force acting on microparticles, $F_g = \left(\rho_{\text{particle}} V_{\text{particle}} - \rho_{\text{water}} V_{\text{water}}\right) g \sin\psi$, is in the range of $(2-6)\times 10^{-14}$ N, where $\rho_{\text{particle}} = 1190$ kg m^{-3} and $V_{\text{particle}} = 4\pi R^3/3$ are the density and the volume of the microsphere, respectively, $\rho_{\text{water}} = 1000$ kg m^{-3} is the density of water, $g = 9.8$ m s^{-2} is the gravitational acceleration, $\psi_{\text{LN}} \approx 0.0035$ rad and $\psi_{\text{CS}} \approx 0.01$ rad are the slope angles of the LN and CS coatings, respectively, measured from the surface topography as $\psi \approx h/d$, where $h \approx 130$ nm is the average amplitude of deformations of the coating's

profile and $d = (10-40)$ μm is the distance between the minima and maxima of the profile. The driving force F_g overcomes the friction, $f = \left(\rho_{\text{particle}} V_{\text{particle}} - \rho_{\text{water}} V_{\text{water}}\right) \mu_r g \cos\psi$ force, where μ_r is the coefficient of rolling friction. A typical value of rolling friction is $\mu_r \approx 10^{-5}$.(*183*) Since $\psi > \mu_r$, the microparticles migrate towards the troughs. The difference in potential energy of the microspheres between the elevated regions and valleys, calculated as $\Delta U_g = V_{\text{particle}}(\rho_{\text{particle}} - \rho_{\text{water}})gh \approx 1.3\times10^{-19}\text{J}$, is significantly higher than the thermal energy, $k_{\text{B}}T = 4.1\times10^{-21}$ J, thus providing a robust trapping at the troughs.

5.4 Conclusion

We demonstrated that light-responsive liquid crystal elastomer coatings can be used for a controlled placement of microparticles. Contact-free UV irradiation creates a non-flat surface topography that is preprogrammed through in-plane molecular alignment of the liquid crystal during the preparation of coatings. Splay deformations of molecular alignment result in depressions of the topography which collect the microparticles thanks to gravity. Assemblies of microparticles are reversible, as the elastomer coatings restore their flat profile under visible light illumination. We demonstrated both linear and circular assemblies of the particles driven by linear defects-disclinations and by disclination-free coatings. In both cases, the microparticles migrate to regions of the lowest potential energy, although the stronger gradients of the molecular alignment in the case of disclinations produce stronger topography variations. More complex director field

patterns could be used for desired particle assembly patterns. For example, periodic lattice of point defects in molecular alignment presented in Ref. (*176*) can be used to create disk- and aster-like clusters of microparticles. It would be of interest to explore whether the proposed non-contact photocontrol of surface topography can be expanded to biological applications to control cell growth, migration, tissue formation, and in designing targeted/site-specific drug delivery systems (*174, 184-186*).

CHAPTER 6

Directing motile skin cells via polymerized liquid crystal nanostructures

6.1 Introduction

Cell migration plays a crucial role in chemotaxis, development, tumor invasion, infection, immunity, and tissue regeneration (*187*). Changes in cell shape, adhesion and cytoskeletal reorganization are some of the key factors in cell migration. Importantly, the microenvironment of the cells affects these processes via chemical or contact guidance cues. The challenge of the regenerative medicine is to develop systems which can produce tissues *in vitro* which have identical architectures to those *in vivo*. In the case of skeletal muscle, for example, organization of fibrils define their functionality (*188*). Also, in the efforts to engineer muscle tissue, one of the vital steps in muskuloskeletal myogenesis is the alignment of myoblasts to form myotubes (*188*).

Various fabrication techniques have been implemented to direct motion of cells through topographical guidance of substrata with ordered structures (*184, 189-204*). They include photolithography, micro-contact printing, stereolithography, electron beam lithography soft-lithography, wet/dry etching or azopolymerization (*184, 194, 205*). Most of these techniques demand sophisticated instrumentation for fabrication of the desired topography of a biomaterial, which are not always available to researchers. Inspired to simplify and expedite the process of fabricating a grooved biocompatible interfaces, we developed a facile method of cell alignment based on liquid crystal (LC) technologies.

In this work, we used a blend of materials which exhibit smectic-A (SmA) phase, characterized by having periodic layered structure (*62*). When SmA materials are in contact with competing boundary conditions (i.e. air/uniformly rubbed glass interface), they develop periodic oily streak defects extending perpendicular to the underlying director field (*206-208*). The mixture was doped with LC diacrylate monomers to polymerize and fixate the desired director of the defects. The oily streak structures which are employed in this investigation have nano- and micro-scale topographical features (*208*). These defect structures make ideal candidates for surface topography generation, since the simple control over director alignment on the desired substrate provides us with limitless number of nano- and micro-patterned structures. Here we show that such biocompatible, grooved surfaces made of liquid crystal networks (LCN) may be used to align human dermal fibroblasts (hDFs) through the so-called contact guidance, which refers to the tendency of cells to be guided by the shape of the underlying surface. The highest aligned states of hDFs are achieved without the deposition of an attachment protein, fibronectin, on to the substrate.

6.2 Materials and Methods

6.2.1 Preparation of the nanogrooved surfaces

The uniform alignment of the monomers was promoted by spin-coating PI2555 (HD Microsystems) polyimide layer on indium tin oxide (ITO)-coated glass substrate and rubbing it with a velvet cloth ten times in a unidirectional manner. A liquid crystalline solution with 14.15 wt/wt% contained reactive monomer, RM82 (Merck), nematic liquid

crystal 4′-(Octyloxy)-4-biphenylcarbonitrile, 8OCB, and a photoinitiator, Irgacure 651 (Ciba) in the 80:19.8:0.2 proportion in Toluene. The chemical structures of the components is shown in Figure 6-1a-c. The solution was subsequently spin-coated onto a planar glass substrate at 400 rpm for 3 sec and 1500 rpm for 30 sec. The antagonistic boundary conditions at the air/SmA liquid crystal interface result in formation of SmA defects called oily streaks which extend perpendicular to the planar anchoring direction, or easy axis (Figure 6-1d).(*208-210*) The polarizing optical microscopy observations (Figure 6-2a) of these structures showed 1-3 μm periodicity. The oily streak structure was polymerized at $T = 50\ ^{\circ}C$ (Linkam TMS 94) using UV LED light source (Thorlabs Inc.) for 10 min with intensity of 18.3 mW/cm^2 in a nitrogen environment. After polymerization of the reactive monomers, the non-reactive 8OCB liquid crystal was thoroughly washed in a solution of Hexane and Dichloromethane (≈ 7:3). The atomic force microscopy (AFM) observations (Figure 6-2b) showed nanogrooved periodic topography of the oily streak structures. On average, the amplitude of the grooves was in the range of 50-100 nm (Figure 6-2b). The substrates were treated with UV ozone for 5 minutes before plating the cells for sterilization purposes.

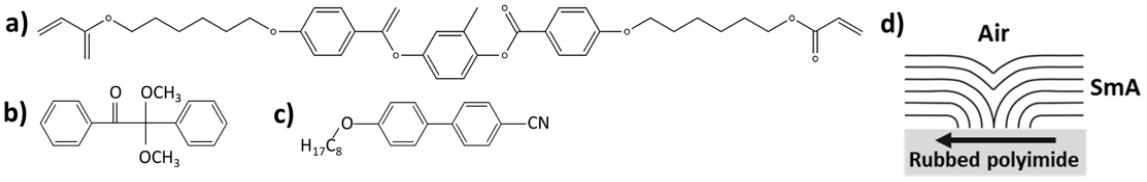

Figure 6-1. Chemical structures of (a) RM82, (b) Irgacure 651 and (c) 8OCB, (d) Schematic representation of the oily streak structure at the air/SmA LC interface.

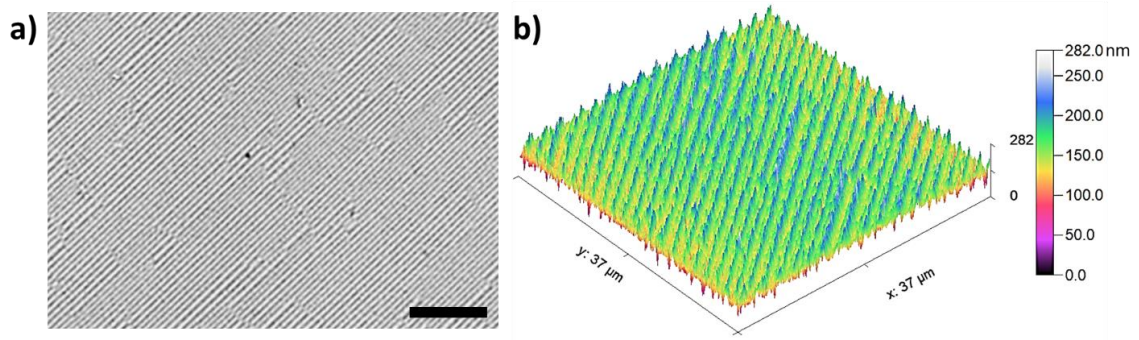

Figure 6-2. a) Bright field observations of the polymerized oily streak structures oriented at 45 °; scale bar 20 µm. b) AFM image showing the grooved periodic surface profiles.

6.2.2 Surface characterization

Three-dimensional surface topography of the polymerized surfaces (Figure 6-2b) were measured using a Table-Top Atomic Force Microscope (AFM Workshop). The data were obtained using tapping mode imaging at room temperature ($T \approx 23\ ^{\circ}C$). The tapping mode probe had a tip of a radius <15 nm with a force constant of 25-95 N/m (SensaProbes, TM190-50). The images were captured with a scan rate of 0.4 Hz at resonant frequency of 216.75 kHz.

6.2.3 Culturing Human Dermal Fibroblasts

Passage 5 human dermal fibroblasts (hDFs) were purchased from American Type Culture Collection and maintained at 37 °C with 5% CO2 and 90% humidity. Cell culture media was composed of Dubbecco's modified Eagle's medium (DMEM, high glucose) supplemented with 10% fetal bovine serum (Clonetics), Glutamax, and penicillin

streptomycin. The cells were seeded at a density of 6.6 x $10^3/cm^2$ into 12-well plates containing four different surfaces in each well. We used fibronectin-coated (50μg/mL, Corning) as well as fibronectin-free surfaces. The hDFs were grown for seven days until reaching confluency.

6.2.4 Immunocytochemistry

After reaching confluency, the old media was removed and cells were rinsed with the phosphate buffer saline (PBS) 1X solution. The adherent cells were fixed with 4% paraformaldehyde (PFA) for immunostaining. The samples were than treated with PBS containing 0.1 % Triton X-100 and subsequently washed with PBS, 1X. Blocking nonspecific enzyme binding was achieved using a 5% fetal bovine serum (FBS) solution, after which the washing step was performed using PBS solution with 0.1% of Tween. Alexa Flour 488 phalloidin was used in order to visualize the actin in cells, whereas, 4′,6-diamidino-2-phenylindole, DAPI, fluorescent stain was utilized to label the nuclear DNA. The fluorescent imaging was performed using Olympus microscope.

6.3 Results

In this study we used four different microenvironments for cell growth. In particular we employed 1) flat glass with fibronectin coating, 2) flat glass without fibronectin, 3) grooved LCN adhered onto a rigid glass substrate without fibronectin and 4) grooved LCN adhered onto a rigid glass substrate with fibronectin. The oily streaks in SmA phase were used to generate nanogrooved surface topography. The orientational order parameter of the cells defined as $S =< 2\cos^2\theta - 1 >$ was used to quantify the cell

alignment, where θ is the angle between the long axis of the cell nucleus and the direction of the grooves. The system is said to be in perfect order when. Flat ITO glass substrates with and without fibronectin coating showed random alignment of hDFs (Figure 6-3a,b). The calculated order parameter was less than $S = 0.25$, characterizing a disordered state (Figure 6-4). Figure 6-3a shows that in an unaligned states, at high concentrations, hDFs form nematic domains exhibiting half-integer topological defects. In contrast, the nanogrooved substrates align the cells parallel to the troughs. The calculated order parameter of cell assemblies at the nanogrooved surface coated with fibronectin is $S = 0.66 \pm 0.21$ (Figure 6-3c). Note here, that the relatively big error reported here is due to the relatively large distribution of the cell orientations in different samples. The best alignment showing the highest order parameter, $S = 0.81 \pm 0.11$, was achieved using the fibronectin-free nanogrooved surface shown in Figure 6-3d and Figure 6-4. Moreover, the images of the actin show that the latter case (Figure 6-5b) exhibits more elongated and highly connected cells as compared to the ones that were grown on fibronectin treated surfaces (Figure 6-5a).

The orientational distribution of the actin filaments was also used in assessing the alignment of the cells. The horizontal axis ($\theta = 0°$) in Figure 6-6 reflects the orientation of the nanogrooves and closely matches the orientation of the actin filaments. The orientation distribution of the actin filaments on the nanogrooved coating was fitted with Gaussian and shows that the full-width-at-half-maximum (FWHM) is 16.5˚. In the case of the untreated flat glass surface, the actin filaments are disorganized and widely vary in their orientations as seen in Figure 6-6.

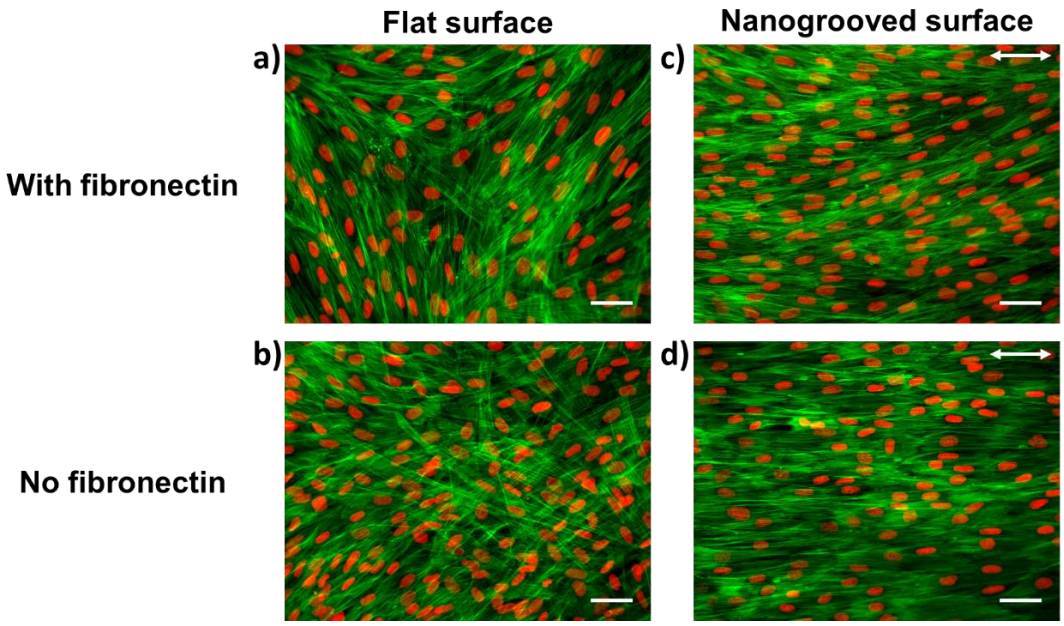

Figure 6-3. Human dermal fibroblast cells grown on flat glass substrate a) with fibronectin, b) without fibronectin and nanogrooved LC polymer surfaces c) with fibronectin, d) without fibronectin. Actin filaments are presented in green, while the nuclei correspond to the red oval regions. The arrows represent the direction of the nanogrooves. Scale bars 50 μm.

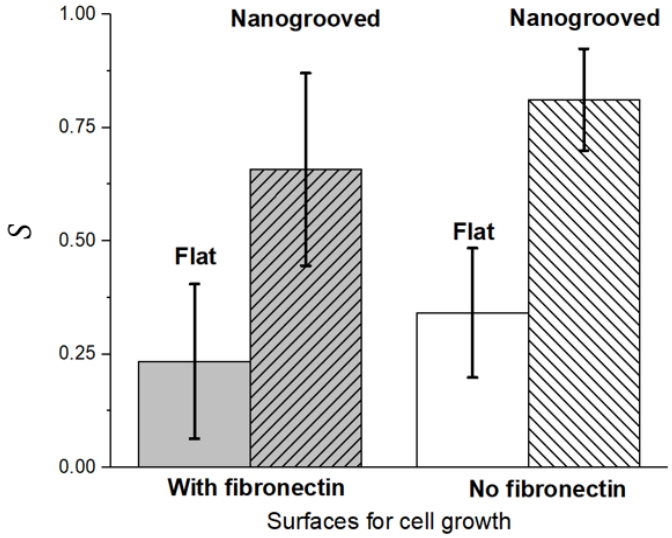

Figure 6-4. Orientational scalar order parameter (*S*) of human dermal fibroblast cells grown on flat glass with and without fibronectin as well as on nanogrooved surfaces with and without the fibronectin treatment.

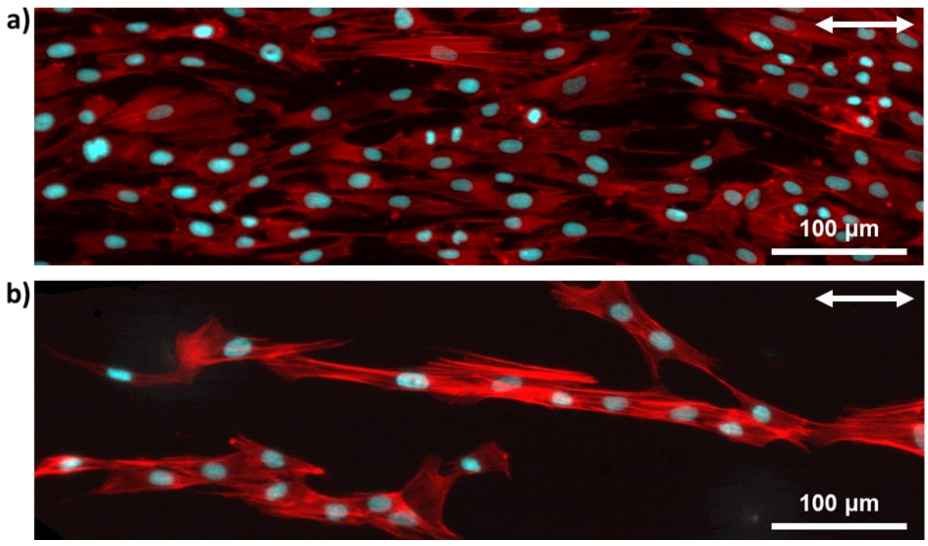

Figure 6-5. Day 3 of human dermal fibroblast cells grown on a) fibronectin coated and b) fibronectin-free nanogrooved surfaces. The arrows represent the direction of the nanogrooves. Actin filaments are presented in red and the nuclei correspond to the light blue oval regions.

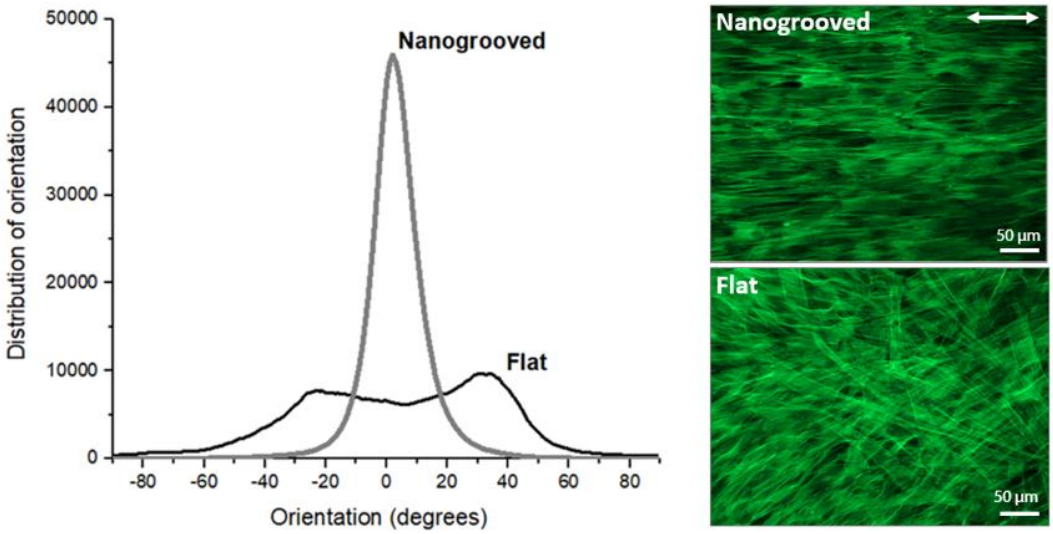

Figure 6-6. Distribution of actin filament orientations for flat and nanogrooved surfaces without fibronectin treatment. The orientation distribution of the actin filaments on the nanogrooved coating fitted with the Gaussian shows FWHM=16.5˚. The arrow represents the direction of the nanogrooves.

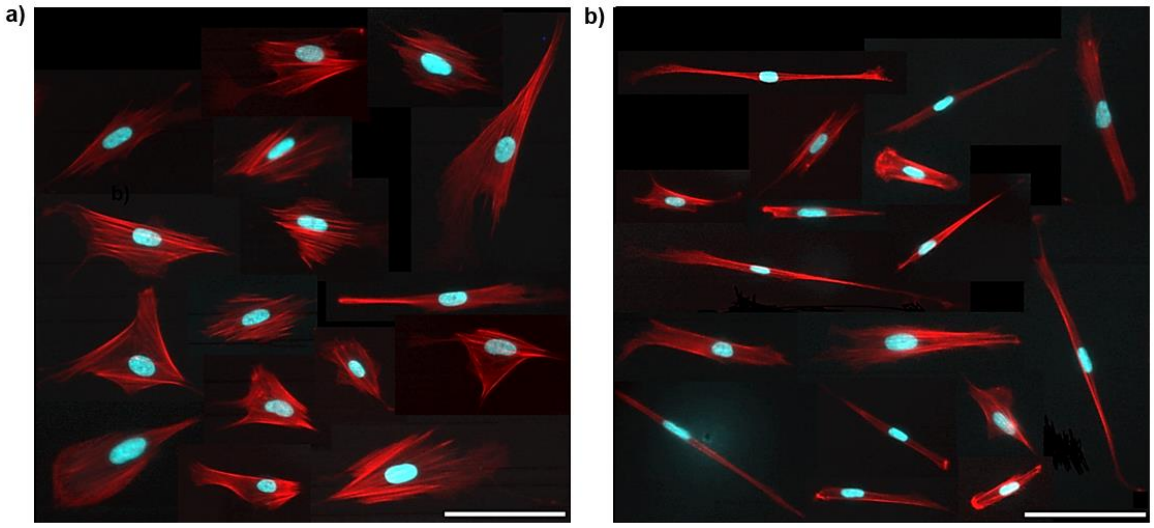

Figure 6-7. A collage of single human dermal fibroblast after day 1 of cells grown on a) fibronectin coated and b) fibronectin-free nanogrooved surfaces. Actin filaments are presented in red and the nuclei correspond to the light blue oval regions. The average aspect ratios of the cells are a) 3.3 and b) 7.6. Scale bars 100 μm.

6.4 Discussion

In the present study, we examined the influence of nanogrooved LCN surfaces comprised of SmA oily streak defects as well as the absence of the extracellular matrix deposition, fibronectin, on alignment of hDFs. The AFM results confirmed 50-100 nm surface topography of the defect structures at the surface of the LCN coating with periodicity of 1-3 μm. We demonstrate that nanogrooved LCN coatings allow hDFs to achieve aligned states, where the order parameter is in the range $S = 0.72 - 0.86$ (Figure 6-3, Figure 6-4). Clark et al defined the population of cells as highly aligned when their long axis makes an angle of $< 10°$ with the direction of the grooves, which corresponds to $S = 0.95$ (*184*). Numerous types of grooved substrates were used in the past, however,

our approach is inexpensive, fast and can be coated over large surface areas. The chemical composition of the reactive monomer also allows one to control the amplitude of the surface topography. Importantly, our method allows generating controlled patterns of grooves by preprogramming the molecular orientation on the glass surface. Here, we used the simplest case, where the LC director is uniform. However, using photopatterning approaches, for instance, allow one to generate any desired director field orientations (*139, 148*). For example, in order to generate concentric circular grooves, one may photopattern a +1 radial topological defect, as the oily streaks orient perpendicular to the underlying director field. The precise control over the LCN structures may guide cell movement in deterministic manner via contact guidance.

Our second observation was the ability to achieve the most aligned state $\left(S = 0.86 \pm 0.08\right)$ on extracellular matrix (fibronectin)-free substrates (Figure 6-4). Fibronectin is a cell surface protein that is widely used to promote cell adhesion, though, it is also important in controlling the cell shape and cell-cell interactions (*211*). Previous reports show that in the absence of the additional extracellular matrix component, fibroblasts may generate their own ECM to serve as scaffold for other cells (*212-214*). Fibroblasts do not bind directly to plastic surface, instead, extracellular glycoproteins, such as fibronectin attachment protein, bind the cells to the substrate (*214*). During migration, fibroblasts leave behind fibronectin tracks on grooved surfaces (*215-217*). Abiko and co-workers confirmed that the tracks on the grooved substratum are deposited on the ridges as well as on the floors and walls of the grooves (*216*). The fibronectin tracks align with the grooves to reinforce the contact guidance produced by the

substratum (*216*). Here we show that fibronectin-free grooved surfaces result in $\theta \approx 3°$ average deviation of the cells with respect to the direction of the grooves (Figure 6-6). For obvious reasons, the cell proliferation on fibronectin-free substrates was slower. However, in this case, our observations show that the hDFs form highly aligned elongated chains. Most likely, the elongated chaining occurs because the cells follow the fibronectin tracks in the grooves that were left behind by the neighboring cells. On average, the aspect ratio of hDFs plated on the fibronectin-free nanogrooved surface after one day of plating the cells is ~ 2 higher than the hDFs on fibronectin coated surfaces Figure 6-7. Meanwhile, the hDFs that were plated on the fibronectin nanogrooved substrates are more spread and have significantly expressed actin filaments and filapodia (Figure 6-5, Figure 6-7). The cells plated on fibronectin coated nanogrooved surface show slight decrease in the alignment possibly due to overcrowding, since fibronectin promotes adhesion and proliferation (Figure 6-4). It is likely that when cells are in close proximity to each other, the population pressure may affect cell-cell contact interaction that may override the cell-surface interaction (*218*).

6.5 Conclusion

We developed a simple technique of creating nanogrooved LCN biointerfaces using liquid crystal defect structures. The control over the molecular orientation of the monomers allows us to achieve the desired pattern of the nanogrooves. Polymerizable liquid crystal monomers fix the periodic nano- and micro-structures developed in SmA phase. The studied hDFs were highly aligned parallel to the nanoridges, where on average, the deviation from the direction of the grooves is about $\pm 17^{\circ}$. Moreover, we

showed that the presence of additional extracellular matrix coating on LCN coating is not a necessary factor for adhesion, alignment or migration of hDFs most likely because fibroblasts are able to secrete their own fibronectin which collects in the narrow grooves. Thus, the fibronectin tracks left behind by the migrating cells may facilitate the adhesion of the cells that follow the fibronectin mediating pathway. In this case, the observations show that the absence of the additional extracellular matrix significantly alters the morphology of the cells and makes them more elongated and, consequently, highly aligned.

CHAPTER 7

Summary

The research presented in this thesis highlights the importance of molecular structure on macroscopic properties of the studied material. Here, we investigate two systems: liquid crystal dimers connected by a flexible spacers and polymerized liquid crystal elastomers/networks with predetermined molecular orientation.

In Chapter 2 and Chapter 3 we explore temperature dependent material parameters of LC dimers formed by 1) two rod-like cyanobiphenyl segments connected by a flexible aliphatic link that show positive dielectric anisotropy and 2) two 2′,3′-difluoroterphenyl rod-like units also connected via flexible alkyl chains, yet exhibiting negative dielectric anisotropy. We report comprehensive set of measurements of birefringence, dielectric anisotropy and visco-elastic parameters. The measured elastic properties are consistent with the tendency of the dimeric molecules to adopt bent configurations that give rise to the N_{TB} phase. We draw a comparison between the negative dimer and its rod-like forming unit and show a distinct deviation in temperature dependent birefringence, dielectric anisotropy and elastic constant behavior. The flexible dimer shows a dramatic departure from the conventional trend of material parameters, especially near the N-N_{TB} pre-transitional region.

In Chapter 4 we present the approach to generate a deterministic thermo-responsive, dynamic surface profiles of LCE coatings that are adhered to a rigid glass

substrate. We demonstrate that upon thermal actuation, the inscribed pattern of the director field determines whether the coating will generate hills, valleys or in-plane deformations. We developed an activation force concept which explains the correlation between the out-of-plane dynamic profiles on in-plane molecular orientation.

In Chapter 5 and Chapter 6 we discuss applications of LC polymerized elastomers/networks, where we show control of microparticle placement using various surface topographies. First, we employ the gravitational force to form linear and circular chain-like assemblies of passive resin microspheres at water/LCE interface upon UV-light illumination. Importantly, the reversibility of the system is achieved by exposing the coating to visible light. Lastly, we employ LCN nanostructures to guide the motility of live biological cells. Using proper boundary conditions at the time of the preparation of an LCN coating, oily streaks are formed and polymerized in the SmA phase. These structures develop periodic surface reliefs, which in turn are employed as topographical cues to induce highly aligned cell constructs.

REFERENCES

1. D. Chen *et al.*, Chiral heliconical ground state of nanoscale pitch in a nematic liquid crystal of achiral molecular dimers. *Proc Natl Acad Sci U S A* **110**, 15931-15936 (2013).
2. V. Borshch *et al.*, Nematic twist-bend phase with nanoscale modulation of molecular orientation. *Nat Commun* **4**, 2635 (2013).
3. D. Chen *et al.*, Twist-bend heliconical chiral nematic liquid crystal phase of an achiral rigid bent-core mesogen. *Phys Rev E Stat Nonlin Soft Matter Phys* **89**, 022506 (2014).
4. M. Gao *et al.*, Direct observation of liquid crystals using cryo-TEM: specimen preparation and low-dose imaging. *Microsc Res Tech* **77**, 754-772 (2014).
5. E. Gorecka *et al.*, Do the short helices exist in the nematic TB phase? *Liquid Crystals* **42**, 1-7 (2015).
6. M. R. Tuchband *et al.*, The twist-bend nematic phase of bent mesogenic dimer CB7CB and its mixtures. *ArXiv e-prints* **1511**, arXiv:1511.07523 (2015).
7. D. A. Paterson *et al.*, Understanding the twist-bend nematic phase: the characterisation of 1-(4-cyanobiphenyl-4 '-yloxy)-6-(4-cyanobiphenyl-4 '-yl)hexane (CB6OCB) and comparison with CB7CB. *Soft Matter* **12**, 6827-6840 (2016).
8. D. A. Paterson *et al.*, Reversible Isothermal Twist-Bend Nematic-Nematic Phase Transition Driven by the Photoisomerization of an Azobenzene-Based Nonsymmetric Liquid Crystal Dinner. *J Am Chem Soc* **138**, 5283-5289 (2016).
9. C. Zhu *et al.*, Resonant Carbon K-Edge Soft X-Ray Scattering from Lattice-Free Heliconical Molecular Ordering: Soft Dilative Elasticity of the Twist-Bend Liquid Crystal Phase. *Phys Rev Lett* **116**, 147803 (2016).
10. I. Dozov, On the spontaneous symmetry breaking in the mesophases of achiral banana-shaped molecules. *Europhys Lett* **56**, 247-253 (2001).
11. R. B. Meyer, Effects of electric and magnetic fields on the structure of cholesteric liquid crystals. *Appl Phys Lett* **12**, 281-282 (1968).
12. R. B. Meyer, *Structural problems in liquid crystal physics*. R. B. a. G. Weil, Ed., Les Houches Summer School in Theoretical Physics, 1973. Molecular Fluids (Gordon and Breach, New York, 1976), pp. 271-343.
13. S. M. Shamid, S. Dhakal, J. V. Selinger, Statistical mechanics of bend flexoelectricity and the twist-bend phase in bent-core liquid crystals. *Phys Rev E* **87**, 052503 (2013).
14. M. Cestari *et al.*, Phase behavior and properties of the liquid-crystal dimer 1″,7″-bis(4-cyanobiphenyl-4′-yl) heptane: A twist-bend nematic liquid crystal. *Phys Rev E* **84**, 031704 (2011).
15. K. Adlem *et al.*, Chemically induced twist-bend nematic liquid crystals, liquid crystal dimers, and negative elastic constants. *Phys Rev E Stat Nonlin Soft Matter Phys* **88**, 022503 (2013).
16. C.-J. Yun, M. R. Vengatesan, J. K. Vij, J.-K. Song, Hierarchical elasticity of bimesogenic liquid crystals with twist-bend nematic phase. *Appl Phys Lett* **106**, 173102 (2015).
17. D. O. Lopez *et al.*, Miscibility studies of two twist-bend nematic liquid crystal dimers with different average molecular curvatures. A comparison between experimental data and predictions of a Landau mean-field theory for the N-TB-N phase transition. *Phys Chem Chem Phys* **18**, 4394-4404 (2016).

18. N. Sebastian *et al.*, Mesophase structure and behaviour in bulk and restricted geometry of a dimeric compound exhibiting a nematic-nematic transition. *Phys Chem Chem Phys* **18**, 19299-19308 (2016).
19. G. Babakhanova *et al.*, Elastic and viscous properties of the nematic dimer CB7CB. *Phys Rev E* **96**, 062704 (2017).
20. G. Cukrov *et al.*, Comparative analysis of anisotropic material properties of uniaxial nematics formed by flexible dimers and rod-like monomers. *Liquid Crystals* **44**, 219-231 (2017).
21. B. Robles-Hernandez *et al.*, Twist, tilt, and orientational order at the nematic to twist-bend nematic phase transition of 1 ",9 "-bis(4-cyanobiphenyl-4 '-yl) nonane: A dielectric, H-2 NMR, and calorimetric study. *Phys Rev E* **92**, 062505 (2015).
22. N. Sebastian *et al.*, Distinctive dielectric properties of nematic liquid crystal dimers. *Liquid Crystals* **44**, 177-190 (2017).
23. S. Shri, Curvature elasticity in liquid crystals. *Physics Reports* **277**, 283-384 (1996).
24. J. Xiang *et al.*, Electrically tunable selective reflection of light from ultraviolet to visible and infrared by heliconical cholesterics. *Advanced Materials* **27**, 3014-3018 (2015).
25. J. Xiang, S. V. Shiyanovskii, C. T. Imrie, O. D. Lavrentovich, Electrooptic Response of Chiral Nematic Liquid Crystals with Oblique Helicoidal Director. *Phys Rev Lett* **112**, 217801 (2014).
26. S. M. Salili *et al.*, Magnetically tunable selective reflection of light by heliconical cholesterics. *Phys Rev E* **94**, 042705 (2016).
27. P. G. De Gennes, Calcul de la distorsion d'une structure cholesterique par un champ magnetique. *Solid State Commun* **6**, 163-165 (1968).
28. D. Pociecha *et al.*, Critical behavior of the optical birefringence at the nematic to twist-bend nematic phase transition. *Phys Rev E* **98**, 052706 (2018).
29. G. P. Crawford, D. J. Broer, S. Žumer, *Cross-linked liquid crystalline systems : from rigid polymer networks to elastomers*. The liquid crystals book series (CRC Press, Boca Raton, FL, 2011), pp. xv, 605 p.
30. T. J. White, D. J. Broer, Programmable and adaptive mechanics with liquid crystal polymer networks and elastomers. *Nat Mater* **14**, 1087-1098 (2015).
31. M. Warner, E. M. Terentjev. (OUP Oxford, 2003).
32. W. H. d. Jeu, *Liquid Crystal Elastomers: Materials and Applications*. (Springer-Verlag Berlin Heidelberg, New York, 2012).
33. D. Q. Liu, C. W. M. Bastiaansen, J. M. J. den Toonder, D. J. Broer, Photo-Switchable Surface Topologies in Chiral Nematic Coatings. *Angew Chem Int Edit* **51**, 892-896 (2012).
34. D. Q. Liu, C. W. M. Bastiaansen, J. M. J. den Toonder, D. J. Broer, Light-Induced Formation of Dynamic and Permanent Surface Topologies in Chiral-Nematic Polymer Networks. *Macromolecules* **45**, 8005-8012 (2012).
35. D. Q. Liu, D. J. Broer, Liquid crystal polymer networks: switchable surface topographies. *Liq Cryst Rev* **1**, 20-28 (2013).
36. D. Q. Liu, D. J. Broer, Light controlled friction at a liquid crystal polymer coating with switchable patterning. *Soft Matter* **10**, 7952-7958 (2014).
37. D. Q. Liu, D. J. Broer, Self-assembled Dynamic 3D Fingerprints in Liquid-Crystal Coatings Towards Controllable Friction and Adhesion. *Angew Chem Int Edit* **53**, 4542-4546 (2014).

38. D. Q. Liu, D. J. Broer, New insights into photoactivated volume generation boost surface morphing in liquid crystal coatings. *Nat Commun* **6**, 8334 (2015).
39. D. Q. Liu, L. Liu, P. R. Onck, D. J. Broer, Reverse switching of surface roughness in a self-organized polydomain liquid crystal coating. *P Natl Acad Sci USA* **112**, 3880-3885 (2015).
40. D. Liu, N. B. Tito, D. J. Broer, Protruding organic surfaces triggered by in-plane electric fields. *Nat Commun* **8**, 1526 (2017).
41. M. Hendrikx, D. Liu, A. P. H. J. Schenning, D. J. Broer, in *SPIE Organic Photonics and Electronics*. (SPIE, 2018), vol. 10735, pp. 10.
42. W. Feng, D. J. Broer, D. Q. Liu, Oscillating Chiral-Nematic Fingerprints Wipe Away Dust. *Advanced Materials* **30**, 1704970 (2018).
43. M. Hendrikx, A. P. H. J. Schenning, D. J. Broer, Patterned oscillating topographical changes in photoresponsive polymer coatings. *Soft Matter* **13**, 4321-4327 (2017).
44. M. Hendrikx, A. P. H. J. Schenning, M. G. Debije, D. J. Broer, Light-Triggered Formation of Surface Topographies in Azo Polymers. *Crystals* **7**, 231 (2017).
45. H. Aharoni, Y. Xia, X. Zhang, R. D. Kamien, S. Yang, Universal inverse design of surfaces with thin nematic elastomer sheets. *Proceedings of the National Academy of Sciences* **115**, 7206 (2018).
46. M. a. R. Aguilar, J. San Román, *Smart polymers and their applications*. Woodhead publishing in materials (Woodhead Publishing, is an imprint of Elsevier, Cambridge, UK, 2014), pp. xvi, 568 pages.
47. H. M. D. Bandara, S. C. Burdette, Photoisomerization in different classes of azobenzene. *Chem Soc Rev* **41**, 1809-1825 (2012).
48. A. B. Harris, R. D. Kamien, T. C. Lubensky, Molecular chirality and chiral parameters. *Rev Mod Phys* **71**, 1745-1757 (1999).
49. J. Xiang *et al.*, Electrically tunable laser based on oblique heliconical cholesteric liquid crystal. *P Natl Acad Sci USA* **113**, 12925-12928 (2016).
50. S. Parthasarathi, D. S. S. Rao, N. B. Palakurthy, C. V. Yelamaggad, S. K. Prasad, Effect of Pressure on Dielectric and Frank Elastic Constants of a Material Exhibiting the Twist Bend Nematic Phase. *J Phys Chem B* **121**, 896-903 (2017).
51. S. Parthasarathi, D. S. S. Rao, N. B. Palakurthy, C. V. Yelamaggad, S. Krishna Prasad, Binary System Exhibiting the Nematic to Twist-Bend Nematic Transition: Behavior of Permittivity and Elastic Constants. *The Journal of Physical Chemistry B* **120**, 5056-5062 (2016).
52. H. J. Deuling, Deformation of Nematic Liquid-Crystals in an Electric-Field. *Mol Cryst Liq Cryst* **19**, 123-131 (1972).
53. M. Majumdar, P. Salamon, A. Jakli, J. T. Gleeson, S. Sprunt, Elastic constants and orientational viscosities of a bent-core nematic liquid crystal. *Phys Rev E* **83**, 031701 (2011).
54. S. Zhou *et al.*, Elasticity, viscosity, and orientational fluctuations of a lyotropic chromonic nematic liquid crystal disodium cromoglycate. *Soft Matter* **10**, 6571-6581 (2014).
55. J. Kędzierski *et al.*, Determination of ordinary and extraordinary refractive indices of nematic liquid crystals by using wedge cells. *Opto-Electron Rev* **18**, 214-218 (2010).
56. T. J. Scheffer, J. Nehring, Accurate Determination of Liquid-Crystal Tilt Bias Angles. *Journal of Applied Physics* **48**, 1783-1792 (1977).

57. Y. A. Nastishin, R. D. Polak, S. V. Shiyanovskii, V. H. Bodnar, O. D. Lavrentovich, Nematic polar anchoring strength measured by electric field techniques. *Journal of Applied Physics* **86**, 4199-4213 (1999).
58. L. M. Blinov, V. G. Chigrinov, *Electrooptic effects in liquid crystal materials*. Partially ordered systems (Springer-Verlag, New York, 1994), pp. xvii, 464 p.
59. M. J. Bradshaw, E. P. Raynes, J. D. Bunning, T. E. Faber, The Frank Constants of Some Nematic Liquid-Crystals. *J Phys-Paris* **46**, 1513-1520 (1985).
60. N. V. Madhusudana, R. Pratibha, Elasticity and Orientational Order in Some Cyanobiphenyls .4. Reanalysis of the Data. *Mol Cryst Liq Cryst* **89**, 249-257 (1982).
61. B. Kundu, Ph.D. Thesis, Raman Research Insitute, Raman Research Institute, Bangalore (2008).
62. P. G. d. G. a. J. Prost, *The Physics of Liquid Crystals (International Series of Monographs On Physics)*. (Oxford: Clarendon Press, ed. Second, 1995).
63. B. Kundu, R. Pratibha, N. V. Madhusudana, Anomalous temperature dependence of elastic constants in the nematic phase of binary mixtures made of rodlike and bent-core molecules. *Phys Rev Lett* **99**, 247802 (2007).
64. R. Borsali, D. Y. Yoon, R. Pecora, Determination of splay and twist relaxation modes in nematic liquid crystals from dynamic light scattering experiments. *J Phys Chem B* **102**, 6337-6341 (1998).
65. M. Cui, Ph.D. Thesis, Kent State University, Kent State University (2000).
66. I. Haller, Thermodynamic and static properties of liquid crystals. *Progress in Solid-State Chemistry* **10**, 103-118 (1975).
67. J. Addis, Ph.D. Thesis, University of Manchester, (2013).
68. N. Avci *et al.*, Viscoelasticity, dielectric anisotropy, and birefringence in the nematic phase of three four-ring bent-core liquid crystals with an L-shaped molecular frame. *Soft Matter* **9**, 1066-1075 (2013).
69. P. Sathyanarayana *et al.*, Viscoelasticity of ambient-temperature nematic binary mixtures of bent-core and rodlike molecules. *Phys Rev E* **85**, 011702 (2012).
70. P. Sathyanarayana, B. K. Sadashiva, S. Dhara, Splay-bend elasticity and rotational viscosity of liquid crystal mixtures of rod-like and bent-core molecules. *Soft Matter* **7**, 8556-8560 (2011).
71. J. A. Olivares, S. Stojadinovic, T. Dingemans, S. Sprunt, A. Jakli, Optical studies of the nematic phase of an oxazole-derived bent-core liquid crystal. *Phys Rev E* **68**, 041704 (2003).
72. S. Kaur *et al.*, Understanding the distinctive elastic constants in an oxadiazole bent-core nematic liquid crystal. *Phys Rev E* **86**, 041703 (2012).
73. S. Kaur *et al.*, The elastic and optical properties of a bent-core thiadiazole nematic liquid crystal: the role of the bend angle. *Journal of Materials Chemistry C* **1**, 2416-2425 (2013).
74. C. Meyer, G. R. Luckhurst, I. Dozov, The temperature dependence of the heliconical tilt angle in the twist-bend nematic phase of the odd dimer CB7CB. *Journal of Materials Chemistry C* **3**, 318-328 (2015).
75. M. R. Tuchband *et al.*, Double-Helical Tiled Chain Structure of the Twist-Bend Liquid Crystal phase in CB7CB. *ArXiv e-prints* **1703**, arXiv:1703.10787 (2017).

76. W. H. de Jeu, T. W. Lathouwers, P. Bordewijk, Dielectric Properties of Di-n-Heptyl Azoxybenzene in the Nematic and in the Smectic-A Phases. *Phys Rev Lett* **32**, 40-43 (1974).
77. W. H. de Jeu, W. J. A. Goossens, P. Bordewijk, Influence of smectic order on the static dielectric permittivity of liquid crystals. *The Journal of Chemical Physics* **61**, 1985-1989 (1974).
78. B. Robles-Hernandez *et al.*, Molecular dynamics of a binary mixture of twist-bend nematic liquid crystal dimers studied by dielectric spectroscopy. *Phys Rev E* **93**, 062705 (2016).
79. N. Sebastian *et al.*, Dielectric, calorimetric and mesophase properties of 1 "-(2 ',4-difluorobiphenyl-4 '-yloxy)-9 "-(4-cyano-biphenyl-4 '-yloxy) nonane: an odd liquid crystal dimer with a monotropic mesophase having the characteristics of a twist-bend nematic phase. *Phys Chem Chem Phys* **16**, 21391-21406 (2014).
80. N. Trbojevic, D. J. Read, M. Nagaraj, Dielectric properties of liquid crystalline dimer mixtures exhibiting the nematic and twist-bend nematic phases. *Phys Rev E* **96**, 052703 (2017).
81. A. Ferrarini, G. R. Luckhurst, P. L. Nordio, S. J. Roskilly, Understanding the Unusual Transitional Behavior of Liquid-Crystal Dimers. *Chem Phys Lett* **214**, 409-417 (1993).
82. A. Ferrarini, G. R. Luckhurst, P. L. Nordio, S. J. Roskilly, Prediction of the Transitional Properties of Liquid-Crystal Dimers - a Molecular-Field Calculation Based on the Surface Tensor Parametrization. *J Chem Phys* **100**, 1460-1469 (1994).
83. A. Ferrarini, G. R. Luckhurst, P. L. Nordio, Even-Odd Effects in Liquid-Crystal Dimers with Flexible Spacers - a Test of the Rotational Isomeric State Approximation. *Mol Phys* **85**, 131-143 (1995).
84. A. Ferrarini, G. R. Luckhurst, P. L. Nordio, S. J. Roskilly, Understanding the dependence of the transitional properties of liquid crystal dimers on their molecular geometry. *Liquid Crystals* **21**, 373-382 (1996).
85. S. Zhou *et al.*, Elasticity of Lyotropic Chromonic Liquid Crystals Probed by Director Reorientation in a Magnetic Field. *Phys Rev Lett* **109**, 037801 (2012).
86. W. H. d. Jeu, *Physical properties of liquid crystalline materials*. Liquid crystal monographs (Gordon and Breach, New York, 1980), pp. x, 133 p.
87. P. Sathyanarayana *et al.*, Splay bend elasticity of a bent-core nematic liquid crystal. *Phys Rev E* **81**, 010702 (2010).
88. C. V. Brown, N. J. Mottram, Influence of flexoelectricity above the nematic Freedericksz transition. *Phys Rev E* **68**, 031702 (2003).
89. A. Varanytsia, L. C. Chien, Giant Flexoelectro-optic Effect with Liquid Crystal Dimer CB7CB. *Sci Rep-Uk* **7**, 41333 (2017).
90. K. S. Krishnamurthy, N. B. Palakurthy, C. V. Yelamaggad, Confined Electroconvective and Flexoelectric Instabilities Deep in the Freedericksz State of Nematic CB7CB. *J Phys Chem B* **121**, 5447-5454 (2017).
91. A. Ferrarini, The theory of elastic constants. *Liquid Crystals* **37**, 811-823 (2010).
92. H. F. Gleeson *et al.*, The Nematic Phases of Bent-Core Liquid Crystals. *Chemphyschem* **15**, 1251-1260 (2014).
93. P. Salamon *et al.*, Dielectric technique to measure the twist elastic constant of liquid crystals: The case of a bent-core material. *Phys Rev E* **85**, 061704 (2012).

94. P. Tadapatri, U. S. Hiremath, C. V. Yelamaggad, K. S. Krishnamurthy, Permittivity, Conductivity, Elasticity, and Viscosity Measurements in the Nematic Phase of a Bent-Core Liquid Crystal. *J Phys Chem B* **114**, 1745-1750 (2010).
95. H. Gruler, Elastic Properties of Nematic Phase Influenced by Molecular-Properties. *J Chem Phys* **61**, 5408-5412 (1974).
96. W. Helfrich, Inherent Bounds to the Elasticity and Flexoelectricity of Liquid Crystals. *Mol Cryst Liq Cryst* **26**, 1-5 (1974).
97. M. Delaye, R. Ribotta, G. Durand, Rayleigh-Scattering at a Second-Order Nematic to Smectic-a Phase Transition. *Phys Rev Lett* **31**, 443-445 (1973).
98. R. Blinc *et al.*, in *Handbook of Liquid Crystals Set*. (Wiley-VCH Verlag GmbH, 1998), pp. 170-197.
99. J. Xiang *et al.*, Electrooptics of chiral nematics formed by molecular dimers. *Liquid Crystals Xviii* **9182**, 91820P-91821 – 91820P-91829 (2014).
100. P. K. Challa *et al.*, Twist-bend nematic liquid crystals in high magnetic fields. *Phys Rev E* **89**, 060501 (2014).
101. C. Meyer, I. Dozov, Local distortion energy and coarse-grained elasticity of the twist-bend nematic phase. *Soft Matter* **12**, 574-580 (2016).
102. R. J. Mandle, E. J. Davis, C. T. Archbold, S. J. Cowling, J. W. Goodby, Microscopy studies of the nematic NTB phase of 1,11-di-(1[prime or minute][prime or minute]-cyanobiphenyl-4-yl)undecane. *Journal of Materials Chemistry C* **2**, 556-566 (2014).
103. V. P. Panov *et al.*, Microsecond linear optical response in the unusual nematic phase of achiral bimesogens. *Appl Phys Lett* **99**, 261903 (2011).
104. V. P. Panov *et al.*, Field-induced periodic chiral pattern in the Nx phase of achiral bimesogens. *Appl Phys Lett* **101**, 234106 (2012).
105. Z. Ahmed, C. Welch, G. H. Mehl, The design and investigation of the self-assembly of dimers with two nematic phases. *Rsc Advances* **5**, 93513-93521 (2015).
106. M. G. Tamba *et al.*, A fibre forming smectic twist-bent liquid crystalline phase. *RSC Advances* **5**, 11207-11211 (2015).
107. Z. Parsouzi *et al.*, Fluctuation Modes of a Twist-Bend Nematic Liquid Crystal. *Physical Review X* **6**, 021041 (2016).
108. S. M. Salili *et al.*, Anomalous Increase in Nematic-Isotropic Transition Temperature in Dimer Molecules Induced by a Magnetic Field. *Phys Rev Lett* **116**, 217801 (2016).
109. O. D. Lavrentovich, V. G. Nazarenko, V. V. Sergan, G. Durand, Dielectric quenching of the electric polar surface instability in a nematic liquid crystal. *Physical Review A* **45**, R6969-R6972 (1992).
110. M. Shribak, R. Oldenbourg, Techniques for fast and sensitive measurements of two-dimensional birefringence distributions. *Appl. Opt.* **42**, 3009-3017 (2003).
111. Y.-K. Kim, G. Cukrov, J. Xiang, S.-T. Shin, O. D. Lavrentovich, Domain walls and anchoring transitions mimicking nematic biaxiality in the oxadiazole bent-core liquid crystal C7. *Soft Matter* **11**, 3963-3970 (2015).
112. H. W. Chen, R. D. Zhu, J. X. Zhu, S. T. Wu, A simple method to measure the twist elastic constant of a nematic liquid crystal. *Liquid Crystals* **42**, 1738-1742 (2015).
113. J. Parka, M. Dabrowski, R. Kowerdziej, Investigations of twist elastic constant K-22 of new nematic liquid crystal materials using threshold IPS method. *Opto-Electron Rev* **19**, 114-118 (2011).

114. F. M. Leslie, C. M. Waters, Light Scattering From a Nematic Liquid Crystal in the Presence of an Electric Field. *Mol Cryst Liq Cryst* **123**, 101-117 (1985).
115. I. Lazo, C. Peng, J. Xiang, S. V. Shiyanovskii, O. D. Lavrentovich, Liquid crystal-enabled electro-osmosis through spatial charge separation in distorted regions as a novel mechanism of electrokinetics. *Nat Commun* **5**, 5033 (2014).
116. P. P. Karat, N. V. Madhusudana, Elasticity and Orientational Order in Some 4'-Normal-Alkyl-4-Cyanobiphenyls .2. *Mol Cryst Liq Cryst* **40**, 239-245 (1977).
117. A. Nych *et al.*, Measurement of the twist elastic constant by phase retardation technique. *Mol Cryst Liq Cryst* **384**, 77-83 (2002).
118. D. V. Sai, K. P. Zuhail, R. Sarkar, S. Dhara, Structure–property correlation of bicyclohexane nematic liquid crystals. *Liquid Crystals* **42**, 328-333 (2015).
119. S. C. G. Czechowski, and J. Jadżyn, The Elastic Constants of Nematic n-Hexylcyanobiphenyl Determined with the Capacitance Method. *Zeitschrift für Naturforschung A* **56**, 257-261 (2001).
120. S. Urban, P. Kula, A. Spadlo, M. Geppi, A. Marini, Dielectric properties of selected laterally fluoro-substituted 4,4"-dialkyl, dialkoxy and alkyl-alkoxy [1:1 ';4':1 "]terphenyls. *Liquid Crystals* **37**, 1321-1330 (2010).
121. P. C. B. Sudipta Kumar Sarkar, Malay Kumar Das, Determination of optical birefringence. *International Journal of Research in Applied, Natural and Social Sciences* **1**, 1-8 (2013).
122. M. Geppi *et al.*, Determination of Order Parameters in Laterally Fluorosubstituted Terphenyls by F-19-NMR, Optical and Dielectric Anisotropies. *Mol Cryst Liq Cryst* **541**, 342-355 (2011).
123. J. W. Emsley, M. Lelli, H. Joy, M. G. Tamba, G. H. Mehl, Similarities and differences between molecular order in the nematic and twist-bend nematic phases of a symmetric liquid crystal dimer. *Phys Chem Chem Phys* **18**, 9419-9430 (2016).
124. E. E. Burnell, Z. Ahmed, C. Welch, G. H. Mehl, R. Y. Dong, Deuteron and proton NMR study of D2, p-dichlorobenzene and 1,3,5-trichlorobenzene in bimesogenic liquid crystals with two nematic phases. *Chem Phys Lett* **659**, 48-54 (2016).
125. R. Balachandran *et al.*, Elastic properties of bimesogenic liquid crystals. *Liquid Crystals* **40**, 681-688 (2013).
126. R. B. Meyer, in *Polymer Liquid Crystals*, W. R. K. a. R. B. M. A. Ciferri, Ed. (Academic Press, New York/London, 1982), pp. 133-185.
127. G. A. Dilisi, C. Rosenblatt, A. C. Griffin, U. Hari, Splay Elasticity in an Oligomeric Liquid-Crystal. *Liquid Crystals* **8**, 437-443 (1990).
128. G. A. Dilisi, E. M. Terentjev, A. C. Griffin, C. Rosenblatt, Viscoelastic Properties of a Bent and Straight Dimeric Liquid-Crystal. *J Phys Ii* **3**, 597-602 (1993).
129. E. Terentjev, R. G. Petschek, Properties of Uniaxial Nematic Liquid-Crystal of Semiflexible Even and Odd Dimers. *J Phys Ii* **3**, 661-680 (1993).
130. M. A. Osipov, G. Pajak, Effect of polar intermolecular interactions on the elastic constants of bent-core nematics and the origin of the twist-bend phase. *The European Physical Journal E* **39**, 1-12 (2016).
131. B. Kundu, R. Pratibha, N. V. Madhusudana, Anomalous temperature dependence of elastic constants in the nematic phase of binary mixtures made of rodlike and bent-core molecules. *Phys Rev Lett* **99**, 247802 (2007).

132. P. De Gregorio, E. Frezza, C. Greco, A. Ferrarini, Density functional theory of nematic elasticity: softening from the polar order. *Soft Matter* **12**, 5188-5198 (2016).
133. R. B. Meyer, Effects of Electric and Magnetic Fields on Structure of Cholesteric Liquid Crystals. *Applied Physics Letters* **12**, 281-282 (1968).
134. M. Warner, E. M. Terentjev, *Liquid crystal elastomers*. International series of monographs on physics (Oxford University Press, Oxford, 2003), pp. xiv, 407 p.
135. D. L. Thomsen *et al.*, Liquid crystal elastomers with mechanical properties of a muscle. *Macromolecules* **34**, 5868-5875 (2001).
136. M. Warner, C. D. Modes, D. Corbett, Curvature in nematic elastica responding to light and heat. *Proc. R. Soc. A* **466**, 2975-2989 (2010).
137. M. E. McConney *et al.*, Topography from Topology: Photoinduced Surface Features Generated in Liquid Crystal Polymer Networks. *Adv Mater* **25**, 5880-5885 (2013).
138. L. T. de Haan, A. P. H. J. Schenning, D. J. Broer, Programmed morphing of liquid crystal networks. *Polymer* **55**, 5885-5896 (2014).
139. T. H. Ware, M. E. McConney, J. J. Wie, V. P. Tondiglia, T. J. White, Voxelated liquid crystal elastomers. *Science* **347**, 982-984 (2015).
140. C. P. Ambulo *et al.*, Four-dimensional Printing of Liquid Crystal Elastomers. *Acs Appl Mater Inter* **9**, 37332-37339 (2017).
141. N. P. Godman, B. A. Kowalski, A. D. Auguste, H. Koerner, T. J. White, Synthesis of Elastomeric Liquid Crystalline Polymer Networks via Chain Transfer. *Acs Macro Lett* **6**, 1290-1295 (2017).
142. T. H. Ware, Z. P. Perry, C. M. Middleton, S. T. Iacono, T. J. White, Programmable Liquid Crystal Elastomers Prepared by Thiol-Ene Photopolymerization. *Acs Macro Lett* **4**, 942-946 (2015).
143. Y. Xia, G. Cedillo-Servin, R. D. Kamien, S. Yang, Guided Folding of Nematic Liquid Crystal Elastomer Sheets into 3D via Patterned 1D Microchannels. *Adv Mater* **28**, 9637-9643 (2016).
144. C. Mostajeran, M. Warner, T. H. Ware, T. J. White, Encoding Gaussian curvature in glassy and elastomeric liquid crystal solids. *Proc Math Phys Eng Sci* **472**, 20160112 (2016).
145. A. H. Gelebart *et al.*, Making waves in a photoactive polymer film. *Nature* **546**, 632-636 (2017).
146. J. E. Stumpel, D. J. Broer, A. P. H. J. Schenning, Stimuli-responsive photonic polymer coatings. *Chem Commun* **50**, 15839-15848 (2014).
147. J. E. Stumpel *et al.*, Photoswitchable Ratchet Surface Topographies Based on Self-Protonating Spiropyran-NIPAAM Hydrogels. *Acs Appl Mater Inter* **6**, 7268-7274 (2014).
148. Y. Guo *et al.*, High-Resolution and High-Throughput Plasmonic Photopatterning of Complex Molecular Orientations in Liquid Crystals. *Adv Mater* **28**, 2353-2358 (2016).
149. S. Zhou, S. V. Shiyanovskii, H. S. Park, O. D. Lavrentovich, Fine structure of the topological defect cores studied for disclinations in lyotropic chromonic liquid crystals. *Nat Commun* **8**, 14974 (2017).
150. A. Petelin, M. Copic, Strain dependence of the nematic fluctuation relaxation in liquid-crystal elastomers. *Phys Rev E Stat Nonlin Soft Matter Phys* **82**, 011703 (2010).
151. T. C. Lubensky, R. Mukhopadhyay, L. Radzihovsky, X. J. Xing, Symmetries and elasticity of nematic gels. *Phys Rev E* **66**, 011702 (2002).

152. R. Aditi Simha, S. Ramaswamy, Hydrodynamic fluctuations and instabilities in ordered suspensions of self-propelled particles. *Phys Rev Lett* **89**, 058101 (2002).
153. J. Prost, J. P. Marcerou, On the microscopic interpretation of flexoelectricity. *J Phys-Paris* **38**, 315-324 (1977).
154. R. Green, J. Toner, V. Vitelli, Geometry of thresholdless active flow in nematic microfluidics. *Phys Rev Fluids* **2**, 104201 (2017).
155. C. D. Modes, K. Bhattacharya, M. Warner, Gaussian curvature from flat elastica sheets. *P Roy Soc a-Math Phy* **467**, 1121-1140 (2011).
156. V. Narayan, S. Ramaswamy, N. Menon, Long-lived giant number fluctuations in a swarming granular nematic. *Science* **317**, 105-108 (2007).
157. K. Kawaguchi, R. Kageyama, M. Sano, Topological defects control collective dynamics in neural progenitor cell cultures. *Nature* **545**, 327-331 (2017).
158. G. Duclos, C. Erlenkamper, J. F. Joanny, P. Silberzan, Topological defects in confined populations of spindle-shaped cells. *Nat Phys* **13**, 58-62 (2017).
159. M. M. Genkin, A. Sokolov, O. D. Lavrentovich, I. S. Aranson, Topological Defects in a Living Nematic Ensnare Swimming Bacteria. *Physical Review X* **7**, 011029 (2017).
160. F. C. Keber *et al.*, Topology and dynamics of active nematic vesicles. *Science* **345**, 1135-1139 (2014).
161. T. B. Saw *et al.*, Topological defects in epithelia govern cell death and extrusion. *Nature* **544**, 212-216 (2017).
162. C. D. Modes, M. Warner, Blueprinting nematic glass: Systematically constructing and combining active points of curvature for emergent morphology. *Phys Rev E* **84**, 021711 (2011).
163. C. Mostajeran, Curvature generation in nematic surfaces. *Phys Rev E* **91**, 062405 (2015).
164. H. Aharoni, E. Sharon, R. Kupferman, Geometry of Thin Nematic Elastomer Sheets. *Phys Rev Lett* **113**, 257801 (2014).
165. A. Konya, V. Gimenez-Pinto, R. L. B. Selinger, Modeling Defects, shape evolution, and Programmed auto-Origami in liquid crystal elastomers. *Front Mater* **3**, 24 (2016).
166. C. D. Modes, K. Bhattacharya, M. Warner, Disclination-mediated thermo-optical response in nematic glass sheets. *Phys Rev E* **81**, 060701(R) (2010).
167. C. D. Modes, M. Warner, Negative Gaussian curvature from induced metric changes. *Phys Rev E* **92**, 010401(R) (2015).
168. L. T. de Haan, C. Sanchez-Somolinos, C. M. W. Bastiaansen, A. P. H. J. Schenning, D. J. Broer, Engineering of Complex Order and the Macroscopic Deformation of Liquid Crystal Polymer Networks. *Angew Chem Int Edit* **51**, 12469-12472 (2012).
169. G. M. Whitesides, B. Grzybowski, Self-assembly at all scales. *Science* **295**, 2418-2421 (2002).
170. O. P. Pishnyak, S. Tang, J. R. Kelly, S. V. Shiyanovskii, O. D. Lavrentovich, Levitation, lift, and bidirectional motion of colloidal particles in an electrically driven nematic liquid crystal. *Phys Rev Lett* **99**, 127802 (2007).
171. D. K. Yoon *et al.*, Internal structure visualization and lithographic use of periodic toroidal holes in liquid crystals. *Nat Mater* **6**, 866 (2007).
172. C. Peng *et al.*, Controlling placement of nonspherical (boomerang) colloids in nematic cells with photopatterned director. *J Phys Condens Matter* **29**, 014005 (2017).
173. C. Peng *et al.*, Control of colloidal placement by modulated molecular orientation in nematic cells. *Sci Adv* **2**, e1600932 (2016).

174. G. Kocer *et al.*, Light-Responsive Hierarchically Structured Liquid Crystal Polymer Networks for Harnessing Cell Adhesion and Migration. *Advanced Materials* **29**, 1606407 (2017).
175. A. Delplanque *et al.*, UV/ozone surface treatment increases hydrophilicity and enhances functionality of SU-8 photoresist polymer. *Applied Surface Science* **314**, 280-285 (2014).
176. G. Babakhanova *et al.*, Liquid crystal elastomer coatings with programmed response of surface profile. *Nat Commun* **9**, 456 (2018).
177. A. H. Gelebart, M. Mc Bride, A. P. H. J. Schenning, C. N. Bowman, D. J. Broer, Photoresponsive Fiber Array: Toward Mimicking the Collective Motion of Cilia for Transport Applications. *Adv Funct Mater* **26**, 5322-5327 (2016).
178. D. Q. Liu, D. J. Broer, Liquid Crystal Polymer Networks: Preparation, Properties, and Applications of Films with Patterned Molecular Alignment. *Langmuir* **30**, 13499-13509 (2014).
179. D. J. Broer, G. N. Mol, Anisotropic Thermal-Expansion of Densely Cross-Linked Oriented Polymer Networks. *Polym Eng Sci* **31**, 625-631 (1991).
180. H. Agha, C. Bahr, Nematic line defects in microfluidic channels: wedge, twist and zigzag disclinations. *Soft Matter* **14**, 653-664 (2018).
181. M. Wang, Y. Li, H. Yokoyama, Artificial web of disclination lines in nematic liquid crystals. *Nat Commun* **8**, 388 (2017).
182. K. Kawasaki, M. Suzuki, *Formation, dynamics, and statistics of patterns*. (World Scientific, Singapore ; Teaneck, N.J., 1990).
183. B. Bhushan, *Introduction to tribology*. (John Wiley & Sons, New York, 2002).
184. P. Clark, P. Connolly, A. S. G. Curtis, J. A. T. Dow, C. D. W. Wilkinson, Topographical Control of Cell Behavior .2. Multiple Grooved Substrata. *Development* **108**, 635-644 (1990).
185. B. Mishra, B. B. Patel, S. Tiwari, Colloidal nanocarriers: a review on formulation technology, types and applications toward targeted drug delivery. *Nanomed-Nanotechnol* **6**, 9-24 (2010).
186. S. T. Sanjay, M. W. Dou, G. L. Fu, F. Xu, X. J. Li, Controlled Drug Delivery Using Microdevices. *Curr Pharm Biotechno* **17**, 772-787 (2016).
187. D. Wedlich, *Cell migration in development and disease*. (Wiley-VCH, Weinheim, 2005), pp. xlviii, 349 p.
188. R. P. Lanza, R. S. Langer, J. Vacanti, *Principles of tissue engineering*. (Academic Press, an imprint of Elsevier, Amsterdam, ed. Fourth edition /, 2014), pp. xlviii, 1887 pages.
189. E. T. den Braber, J. E. de Ruijter, L. A. Ginsel, A. F. von Recum, J. A. Jansen, Quantitative analysis of fibroblast morphology on microgrooved surfaces with various groove and ridge dimensions. *Biomaterials* **17**, 2037-2044 (1996).
190. D. M. Brunette, Fibroblasts on Micromachined Substrata Orient Hierarchically to Grooves of Different Dimensions. *Exp Cell Res* **164**, 11-26 (1986).
191. A. Curtis, C. Wilkinson, Topographical control of cells. *Biomaterials* **18**, 1573-1583 (1997).
192. M. K. Driscoll, X. Y. Sun, C. Guven, J. T. Fourkas, W. Losert, Cellular Contact Guidance through Dynamic Sensing of Nanotopography. *Acs Nano* **8**, 3546-3555 (2014).
193. G. A. Dunn, A. F. Brown, Alignment of Fibroblasts on Grooved Surfaces Described by a Simple Geometric Transformation. *J Cell Sci* **83**, 313-340 (1986).

194. C. Fedele, P. A. Netti, S. Cavalli, Azobenzene-based polymers: emerging applications as cell culture platforms. *Biomater Sci-Uk* **6**, 990-995 (2018).
195. S. Fujita, M. Ohshima, H. Iwata, Time-lapse observation of cell alignment on nanogrooved patterns. *J R Soc Interface* **6**, S269-S277 (2009).
196. J. R. Gamboa, S. Mohandes, P. L. Tran, M. J. Slepian, J. Y. Yoon, Linear fibroblast alignment on sinusoidal wave micropatterns. *Colloid Surface B* **104**, 318-325 (2013).
197. D. W. Hamilton, C. Oakley, N. A. F. Jaeger, D. M. Brunette, Directional Change Produced by Perpendicularly-Oriented Microgrooves is Microtubule-Dependent for Fibroblasts and Epithelium. *Cell Motil Cytoskel* **66**, 260-271 (2009).
198. R. Kemkemer, S. Jungbauer, D. Kaufmann, H. Gruler, Cell orientation by a microgrooved substrate can be predicted by automatic control theory. *Biophys J* **90**, 4701-4711 (2006).
199. E. Lamers *et al.*, Dynamic Cell Adhesion and Migration on Nanoscale Grooved Substrates. *Eur Cells Mater* **23**, 182-194 (2012).
200. Y. H. Li *et al.*, Engineering cell alignment in vitro. *Biotechnol Adv* **32**, 347-365 (2014).
201. T. Peterbauer *et al.*, Dynamics of Spreading and Alignment of Cells Cultured In Vitro on a Grooved Polymer Surface. *J Nanomater*, 1-10 (2011).
202. A. M. Rajnicek, S. Britland, C. D. McCaig, Contact guidance of CNS neurites on grooved quartz: influence of groove dimensions, neuronal age and cell type. *J Cell Sci* **110**, 2905-2913 (1997).
203. T. Ristori, A. Vigliotti, F. P. T. Baaijens, S. Loerakker, V. S. Deshpande, Prediction of Cell Alignment on Cyclically Strained Grooved Substrates. *Biophys J* **111**, 2274-2285 (2016).
204. C. Simitzi, A. Ranella, E. Stratakis, Controlling the morphology and outgrowth of nerve and neuroglial cells: The effect of surface topography. *Acta Biomater* **51**, 21-52 (2017).
205. M. Nikkhah, F. Edalat, S. Manoucheri, A. Khademhosseini, Engineering microscale topographies to control the cell-substrate interface. *Biomaterials* **33**, 5230-5246 (2012).
206. M. Kleman, O. D. Lavrentovich, *Soft matter physics : an introduction*. Partially ordered systems (Springer, New York, 2003), pp. xxv, 637 p.
207. B. Zappone, E. Lacaze, Surface-frustrated periodic textures of smectic- a liquid crystals on crystalline surfaces. *Phys Rev E Stat Nonlin Soft Matter Phys* **78**, 061704 (2008).
208. I. Gharbi, A. Missaoui, D. Demaille, E. Lacaze, C. Rosenblatt, Persistence of Smectic-A Oily Streaks into the Nematic Phase by UV Irradiation of Reactive Mesogens. *Crystals* **7**, 358 (2017).
209. M. Kleman, O. D. Lavrentovich, Topological point defects in nematic liquid crystals. *Philos Mag* **86**, 4117-4137 (2006).
210. B. Zappone, E. Lacaze, Surface-frustrated periodic textures of smectic-A liquid crystals on crystalline surfaces. *Phys Rev E* **78**, 061704 (2008).
211. F. Grinnell, M. K. Feld, Initial Adhesion of Human-Fibroblasts in Serum-Free Medium - Possible Role of Secreted Fibronectin. *Cell* **17**, 117-129 (1979).
212. A. L. Allan, *Cancer stem cells in solid tumors*. Stem cell biology and regenerative medicine (Humana Press, New York, 2011), pp. xvii, 475 p.
213. I. R. Fernandes *et al.*, Fibroblast sources: Where can we get them? *Cytotechnology* **68**, 223-228 (2016).
214. H. K. Kleinman, R. J. Klebe, G. R. Martin, Role of Collagenous Matrices in the Adhesion and Growth of Cells. *J Cell Biol* **88**, 473-485 (1981).

215. W. Halfter, D. Liverani, M. Vigny, D. Monard, Deposition of Extracellular-Matrix Along the Pathways of Migrating Fibroblasts. *Cell Tissue Res* **262**, 467-481 (1990).
216. Y. Abiko *et al.*, Immunohistochemical Investigation of Tracks Left by the Migration of Fibroblasts on Titanium Surfaces. *Cell Mater* **3**, 161-170 (1993).
217. W. Halfter, I. Diamantis, D. Monard, Migratory Behavior of Cells on Embryonic Retina Basal Lamina. *Dev Biol* **130**, 259-275 (1988).
218. M. T. Lam, S. Sim, X. Y. Zhu, S. Takayama, The effect of continuous wavy micropatterns on silicone substrates on the alignment of skeletal muscle myoblasts and myotubes. *Biomaterials* **27**, 4340-4347 (2006).